2P

NASA CR-121148
PWA™-4517

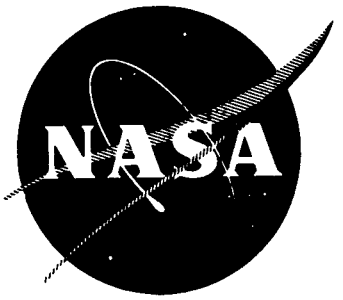

HIGH LOADING, LOW SPEED FAN STUDY
V. FINAL REPORT

by
M. J. Keenan and E. A. Burdsall
Pratt & Whitney Aircraft Division
United Aircraft Corporation

APRIL 1973

Prepared for
National Aeronautics and Space Administration
NASA Lewis Research Center
Contract NAS3-10483

1. Report No.	2. Government Accession No.	3. Recipient's Catalog No.
CR-121148		

4. Title and Subtitle	5. Report Date
High Loading, Low Speed Fan Study V. Final Report	6. Performing Organization Code April 1973
7. Author(s) M. J. Keenan and E. A. Burdsall	8. Performing Organization Report No. PWA™-4517
9. Performing Organization Name and Address Pratt & Whitney Aircraft Division United Aircraft Corporation East Hartford, Connecticut	10. Work Unit No. 11. Contract or Grant No. NAS3-10483
12. Sponsoring Agency Name and Address National Aerodynamic and Space Administration Washington, D. C. 20546	13. Type of Report and Period Covered Contractor Report 14. Sponsoring Agency Code

15. Supplementary Notes

Project Manager, T. F. Gelder, Fluid System Components Division, Lewis Research Center, Cleveland, Ohio

16. Abstract

A low-speed, low-noise, single-stage fan was designed and tested. Design pressure ratio was 1.5 at a rotor tip speed of 1000 ft/sec (304.8 m/sec). No inlet-guide-vane was used, and the rotor-stator was spaced and the number of rotor and stator airfoils was selected for low noise. Tests were conducted with uniform and distorted inlet-flows. Stall margin of the initial design was too low for practical application. Airfoil slots and boundary layer and endwall devices did not improve stall margin sufficiently. A redesigned stator with reduced loadings increased stall margin, giving a fan efficiency of 0.883, 15% stall margin, and a 1.474 pressure ratio at a specific flow of 41.7 lb/sec ft^2 (204.5 kg/sec m^2). Casing treatment over rotor tips improved stall margin with distorted inlet flow; vortex generators did not. Blade-passing-frequency noise increased with rotor relative Mach number. No supersonic fan-noise was measured below 105% of design speed. Slotting airfoils, casing treatments, and a reduction of the ratio (number-stators/number-rotors) from (2 n + 16) to (2 n + 2) had no significant effect on noise.

17. Key Words (Suggested by Author(s))		18. Distribution Statement
Low speed fan	Inlet distortion	Unclassified-Unlimited
Low noise fan	Stall Margin	
Rotor case treatment		

19. Security Classif. (of this report)	20. Security Classif. (of this page)	21. No. of Pages	22. Price*
Unclassified	Unclassified	131	3.00

* For sale by the National Technical Information Service, Springfield, Virginia 22151

TABLE OF CONTENTS

LIST OF ILLUSTRATIONS

LIST OF ILLUSTRATIONS (Cont'd)

LIST OF ILLUSTRATIONS (Cont'd)

LIST OF ILLUSTRATIONS (Cont'd)

LIST OF ILLUSTRATIONS (Cont'd)

LIST OF ILLUSTRATIONS (Cont'd)

LIST OF ILLUSTRATIONS (Cont'd)

LIST OF TABLES

HIGH LOADING, LOW SPEED FAN STUDY
V. FINAL REPORT

BY

M.J. Keenan and E.A. Burdsall

Pratt & Whitney Aircraft Division

United Aircraft Corporation

SUMMARY

A program was conducted for the purpose of evaluating the performance characteristics of a low tip-speed, single-stage fan that would be applicable to low-noise turbofan engines and to demonstrate acceptable efficiency, pressure ratio, and stall margin. The fan had no inlet-guide-vanes, and the axial location and number of the stator vanes were determined from acoustic considerations. The fan was designed to have a rotor tip speed of 1000 ft/sec (304.8 m/sec), a hub-to-tip ratio of 0.392 at the rotor inlet, and a pressure ratio of 1.5; high blade loadings and large past-axial exit angles were necessary to obtain this design pressure ratio because of the low rotor-speeds. The rotor had a design maximum diffusion factor of 0.54, occurring at 60 percent span from the hub. Design relative flow-angles at the rotor exit were past-axial from the hub to 30 percent span. The design flow angle was -39.6 degrees at the hub. The stator was originally designed to have a maximum diffusion factor of 0.64 but was later redesigned to have a maximum diffusion factor of 0.48; both these stators had maximum loadings at the hub.

Three fan-configurations were evaluated: 1) unslotted rotor and unslotted stator, 2) slotted rotor and slotted stator, and 3) slotted rotor and redesigned stator (unslotted). The first two configurations had boundary layer suction slits at the stator hub. These two configurations had good efficiency near stall, but they did not have adequate stall margin for practical applications. It was determined that stator-initiated stalls were the cause of this deficiency. Stator initiated-stalls were identified from strain-gage records and by analysis of blade and vane loadings. As a result, the stator was redesigned using additional annulus convergence and solidity to lower the diffusion factor. The third fan-configuration, with slotted rotor and redesigned stator but without slit suction, had good performance at 15 percent stall margin. The large past-axial exit-angles at the rotor did not cause instabilities in any of the tests conducted.

The peak efficiency at design speed of all three configurations exceeded the design prediction of 0.873. Weight flow on an operating line with 15 percent stall margin was lower than design flow due to inadequate rotor blade throat area and to excessive deviation angles at the rotor tip. Radial distributions of flow conditions were in fair agreement with design predictions, and velocity vectors were within the range of low-loss incidence angles on the rotor and stator. Boundary-layer suction through slits located at the intersections of the stator suction surfaces with the hub wall raised the stator loading limit and reduced stator losses. Slots in the rotor and stator improved part-speed efficiency, but no significant improvement in loading capability was obtained. Tip-radial and circumferential distortions of the inlet flow reduced stall margin, but hub-radial distortion increased stall margin. Honeycomb and skewed-slots casing treatment over the rotor tip gave increased stall margin with inlet distortions, but vortex generators on the case upstream of the rotor tip did not increase the stall margin.

Fan stage performance parameters at design speed are presented in Table I for the three fan-configurations tested.

TABLE I
SUMMARY OF FAN STAGE PERFORMANCE AT DESIGN SPEED

Parameter	Unslotted Rotor and Stator[1]	Slotted Rotor and Stator[1]	Slotted Rotor and Redesigned Stator
Flow Range, (% of Design Flow[2]):			
Max. Flow	100.8	99.7	99.5
Min. Flow	93.2 - 97.7[3]	92.7	87.1
Max. Stage Adiabatic Efficiency	0.881	0.883	0.886
Max. Pressure Ratio	1.484	1.497	1.506
Stage Adiabatic Efficiency (at 15% Stall Margin[4])	0.783	0.788	0.883
Pressure Ratio (at 15% Stall Margin)	1.400	1.401	1.474

1. With boundary layer suction at hub.
2. Design Flow = 185 lb/sec (83.92 kg/sec)
3. Intermittent stall within this flow range.
4. % Stall Margin at Point n = $\left[\frac{(W\sqrt{\theta/\delta})_n}{(W\sqrt{\theta/\delta})_{stall}} \times \frac{(P/P)_{stall}}{(P/P)_n} - 1 \right] \times 100$

Noise measurements were obtained from an array of microphones located within the inlet plenum chamber. Broadband noise generated by the fan stage and measured by these microphones was relatively constant over the range of speeds and flows tested. Other fan stages tested in the same facility have shown increased broadband noise with increased tip relative Mach number. Blade-passage-frequency noise levels increased with blade tip relative Mach number. The lower number of vanes (i.e., 50) in the redesigned stator (the original design had 64 vanes) did not affect the levels of inlet radiated blade-passage-frequency noise significantly. Supersonic fan noise (combination tone or multiple pure-tones) existed only at 105 percent design speed and above. The skewed-slots casing-treatment did not adversely affect noise.

INTRODUCTION

A program was conducted to determine the performance characteristics of a single-stage, low tip-speed fan that would be applicable to a low noise, aircraft engine. To achieve low noise, the fan stage was designed without inlet-guide-vanes, a large axial spacing between rotor and stator blade-rows, and a ratio of stator to rotor blades that theory indicated would prevent propagation of blade-to-blade row interaction noise [ref. 1]. To obtain a required pressure ratio of 1.5 from a single-stage fan with a low rotor tip-speed required the employment of unconventional aerodynamics (i.e., large negative relative angles at the rotor hub exit, high stator inlet Mach numbers, and high blade loadings). The program included aerodynamic performance testing with uniform and distorted inlet flows and noise testing. Three fan-configurations were evaluated:

1) unslotted rotor and unslotted stator

2) slotted rotor and slotted stator

3) slotted rotor and redesigned stator (unslotted).

Multiple-circular-arc blading was used for the rotor and stator of all three fan-configurations. The first and second fan-configurations were provided with suction slits at the stator hub.

Testing of the first fan-configuration indicated that while the efficiency was good, the stall margin was too low for practical application. To improve stall margin, the rotor and stator blades were slotted. Additional tests were run with honeycomb case treatment over the rotor tip and with vortex generators to energize the boundary layer flow entering the rotor tip. These modifications did not increase stall margin sufficiently. It was determined that stall margin was being limited by the stator. As a result, the stator was redesigned with lower loadings. This third fan-configuration had satisfactory stall margin as well as good efficiency. A skewed-slot case treatment over the rotor hub of the third fan-configuration gave improved stability during inlet-distortion operation.

This report provides a design summary and a comparison of test results for the three fan-configurations. Details of the original design, including design considerations and criteria, are provided in reference 2. Detailed data and performance obtained from testing of the first, second, and third fan-configurations are provided in references 3, 4, and 5, respectively. Other NASA programs related to this technology include tests of highly loaded, high Mach number stators with a rotor that turned past-axial [ref. 6] and tests of a low speed rotor, similar to the one described herein, in a "quiet engine" fan program [ref. 7].

All symbols and parameters appearing in this report are defined in Appendix 1.

TEST COMPRESSOR

ACOUSTIC CONSIDERATIONS

During design of this fan, emphasis was given to features that would reduce the three basic types of noise associated with fans: 1) discrete blade-passing-frequency noise, due to both blade-vane interaction and the rotor pressure field, 2) broadband noise, and 3) supersonic fan-noise (also referred to as combination tone, multiple pure-tones, or buzz saw).

Blade-vane interaction noise consists of discrete tones at fundamental blade-passing-frequency and higher harmonics generated by rotor blades chopping the wakes from upstream inlet-guide-vanes and by rotor wakes passing over the downstream stators. This fan was designed without inlet-guide-vanes to avoid guide-vane-rotor interactions and with a large axial spacing between the rotor and stator to permit the rotor wakes to decay before impinging on the stator. The spacing used was approximately two axially-projected rotor chords for the original-stator configurations and six percent less for the redesigned-stator configuration.

The choice of the number of rotor blades and stator vanes was made in accordance with blade-vane interaction theory [ref. 1]. Briefly, if the blade-vane interaction generates a rotating pressure pattern having a subsonic (approximately) tangential speed, the amplitude of the pattern will decay within the duct; whereas, supersonic speed will cause the pattern to propagate without attenuation, resulting in much louder levels of blade-passing-frequency noise being radiated from the inlet and fan ducts.

Each pressure pattern consists of a number (m) of lobes, or cycles, of circumferential pressure variation. The number of lobes is given by the expression $m = nB - kV$, in which V is the number of vanes, B is the number of blades, n is the harmonic number, and k is an integer taking all positive and negative values. Each pattern spins in the duct with a tangential Mach number equal to $(nB/m)\, M_{tip}$, where M_{tip} is equal to the rotor tip speed (U_{tip}) divided by acoustic speed.

Noise decays when the m-lobed pattern spins with a tangential Mach number that is less than the cutoff Mach number. The cutoff Mach number is near unity. However, its exact value depends on the number of circumferential lobes in the pattern, the hub-to-tip ratio of the rotor, the number of nodal points across the fan annulus (radial distribution), and the axial Mach number of the flow [ref. 1 and 8]. For all the configurations tested during this program, the cutoff Mach number was about 0.87. The maximum pattern Mach number for the first harmonic is with the minimum possible value of m. The maximum pattern Mach number generally can be made to be less than the cutoff Mach number for blade-vane interaction patterns by selecting the number of vanes to exceed about twice the number of blades. With a B of 24 and a V of 64 for the original design, the minimum value of m was $24 - 64 = -40$ lobes. This pattern spins backward at 24/40 of M_{tip} for a tangential Mach number of about 0.55. Compared with a cutoff Mach number of 0.87, the 64 V configuration was well below cutoff of the fundamental interaction tone at design speed. Changing from 64 to 50 vanes yielded an m of -26 lobes and a pattern tangential Mach number of about 0.84. Thus the redesigned 50 V configuration also was below cutoff at design speed, and no acoustic penalty

was to be expected. The M_{tip} of the 64-vane fan-configuration could have gone substantially supersonic before interaction noise would have propagated; however, this was of little practical importance since the direct rotor-field dominates at supersonic rotor tip speeds and supersonic fan-noise is inevitably generated by the shock wave inequalities at the blade tips.

In principle, control of the second harmonic (n = 2 in the above formulas) of blade passage noise can be achieved by similar means. The criterion here is that the vane number must exceed about four times the number of blades. In practice, the large number of vanes implied by this requirement is incompatible with obvious aerodynamic and structural restrictions. In this fan, however, the axial separation of blades and vanes could be expected to reduce this harmonic tone.

Discrete tone noise at the rotor blade-passing-frequency is also generated by the rotor alone. The number of lobes in the pressure pattern at the first harmonic is equal to the number of blades and spins at rotor speed. This pattern was below cutoff with the tip speed at 90 percent design speed. Thus, designing the fan for low tip-speed ensured decay of the rotor-alone discrete-tone-noise over much of the normal operating range of the fan.

The second type of fan noise, broadband noise, is identified by a relatively smooth spectrum having no predominant frequency components. It is random in character and can be described in terms of time-average properties such as overall power, overall sound pressure level, and spectrum shape. This type of noise is due primarily to: 1) unsteady forces on the blades, which are related to the randomness associated with the boundary layer and wake flow characteristics, 2) the random inflow turbulence interacting with the blade row, and 3) air scrubbing over surfaces such as blade and vane rows and the duct walls. Experience in testing of other single-stage fans indicates that the level of broadband noise increases at about the fifth power of the rotor blade tip-speed. Thus, the low design tip-speed of the subject fan, 1000 ft/sec (304.8 m/sec), should yield lower broadband noise levels than those generated by current, conventional fan stages which operate at higher tip speeds.

When relative Mach numbers into the fan rotor blades exceed unity, a shock-wave pattern is formed by each rotor blade. Upstream of the rotor blades, these shock waves decay to a system of Mach waves which propagate out of the inlet duct. This is the third type of fan noise, supersonic fan-noise. If all of the blades in the rotor were identical, the resulting radiated noise would be at blade-passing-frequency. However, small variations due to normal manufacturing tolerances yield a wave pattern which produces harmonics of rotor speed, resulting in a low pitched, "buzz-saw" noise. This type of noise was minimized by providing low inlet relative tip Mach numbers by means of low rotor-blade tip-speeds.

FLOWPATH AND VELOCITY VECTOR DIAGRAMS

The fan stage flowpath had a constant outer diameter of 31.0 inches (0.787 m) and a rotor inlet hub-tip ratio of 0.392. Design flow per unit annulus area at the rotor leading edge was set at 42 lb/sec-ft^2 (205.97 kg/sec-m^2), giving a design flow rate of 185 lb/sec (83.92 kg/sec). The rotor was designed for a constant spanwise pressure ratio of 1.55, giving an average

pressure ratio of 1.50 for the stage. Total pressure losses for all blade elements were estimated using shock and profile loss models. The predicted rotor efficiency was 0.933, and predicted stage efficiency was 0.873.

Overall flowpath convergence was determined by the design pressure ratio and ratio of exit-to-inlet-velocities. A major aerodynamic problem inherent in any low speed, low hub-tip ratio, highly-loaded compressor stage is the large past-axial turnings which occur in the rotor hub region. In design of this fan, flowpath convergence at the rotor hub was used to raise exit rotor speed and limit the past-axial turning. The rotor exit design air angle, β'_2, at the hub was, however, still highly negative (-39.6 degrees). Convergence was also used to relieve local high-loading at the stator hub. The resulting flowpath (Figure 1) had a constant tip diameter, a converging hub across the rotor and stator, and a constant hub-diameter section between the blade rows.

The rotor design loading (diffusion factor, D) was a maximum of 0.54 at 60 percent span from the hub and 0.53 at the tip. The design diffusion factor of the original stator was less than 0.5 over the outer 75 percent of the span and reached its maximum of 0.64 at the hub. Tests with the original stator showed that this high loading at the hub caused a stall margin deficiency. To improve the stall margin, the stator was redesigned with more hub convergence, higher solidity, and a lower aspect ratio (Figure 1). The design diffusion factors of the redesigned stator were less than 0.5 over the entire span. The reduced loading was achieved primarily by increasing the design Mach number at the stator exit. The design diffusion factors for the rotor and the two stators versus span are presented in Figure 2, and the design Mach numbers at the exit of the two stators versus span are presented in Figure 3.

The design relative Mach numbers at the inlet of the rotor were subsonic to about 71 percent span from the hub and reach a maximum of 1.13 at the tip. The design Mach numbers at the stator inlet were highest (0.90) at the hub. Spanwise profiles of design relative Mach number at the rotor inlet and design absolute Mach number at the entrance to both stators are presented in Figure 4. The differences in the Mach number profiles at the leading edge of the two stators are due to differences in the design point in addition to the flowpath changes. Velocity diagrams used to redesign the stator were calculated for the modified flowpath and for the aerodynamic performance of the slotted rotor at a design speed data point which had a corrected flow of 179.7 lb/sec (81.84 kg/sec) and a stage pressure ratio of 1.488 [ref. 4].

The lower aspect ratio of the redesigned stator required the reduction in the number of stator vanes (from 64 to 50) and the six percent reduction in the axial spacing between the rotor and stator discussed under Acoustic Considerations.

AIRFOIL DESIGN

The rotor and stator blades had multiple-circular-arc (MCA) airfoils designed on conical surfaces which approximated stream surfaces of revolution. The MCA airfoil design concept is discussed and airfoil definitions are described in reference 2. Chord length and thickness ratios were determined primarily by mechanical considerations.

Rotor

The rotor had 24 blades with aerodynamic chords of 4.5 inches (11.42 cm) at the hub and 5.525 inches (14.034 cm) at the tip. The ratio of maximum-thickness to chord was 0.07 at the root and 0.03 at the tip. Both chord and thickness ratios varied linearly between root and tip. Solidity was 1.359 at the tip and 2.513 at the root. A photograph of a rotor blade is presented in Figure 5.

Design incidence angles for sections with subsonic inlet relative Mach numbers were based on rotor test data except at the hub where cascade data were used. A supersonic flow alignment technique [ref. 2] was used for the outer 22 percent of span. Deviation angles were calculated using a form of Carter's Rule plus an experience factor [ref. 2] over the outer 75 percent of span. Applicable two-dimensional cascade data were used to calculate the deviation angles at the hub where no rotor data were available for turnings of 39.6 degrees past axial. Deviation angles were faired between the cascade test value at the hub and the standard prediction system value at 25 percent span from the hub [ref. 2].

Chordwise camber distributions for the MCA rotor airfoils were selected to control stream-tube throat area between adjacent airfoils on stream surfaces of revolution. Airfoils with inlet relative Mach numbers less than 1.0 were designed to have a minimum critical-area ratio (A/A*) in channels between blades equal to 1.03 times the A/A*, corresponding to the inlet relative Mach number. Airfoils with inlet relative Mach numbers greater than 1.0 were designed to have a minimum A/A* of 1.03. It was necessary to limit the maximum-thickness to chord ratio of 0.07 at the hub in order to obtain the required channel area.

Design blade-element performance parameters are provided in Appendix 2, and airfoil definitions are provided in Appendix 3. Details of the rotor design are given in reference 2.

Stators

Two stators were designed – photographs of both stator vanes are shown in Figure 5. The original stator had an aspect ratio of 3.67 (based on an average blade-length and aerodynamic hub chord) and high loadings, and the redesigned stator had an aspect ratio of 2.46 and lower loadings to improve stall margin. Both stators had MCA airfoil sections.

ORIGINAL STATOR

The original stator had 64 blades, a hub solidity of 2.169, and aerodynamic chord lengths of 1.877 inches (4.768 cm) at the root and 1.826 inches (4.638 cm) at the tip. Maximum-thickness to chord ratio tapered linearly from 0.039 at the hub to 0.07 at the tip. Design incidence was set approximately at zero degrees to the suction surface. Deviation angles were based on Carter's Rule plus an experience factor. The transition between front and rear sections of the MCA airfoils was located at the channel entrance or at an assumed shock-intersection point on the airfoil suction surface. Camber of the front section was 60 percent of an equivalent double-circular-arc (DCA) airfoil front camber. The lowest critical-area ratio (A/A*) was 1.08 for the stream-tube throats of the stator blade elements, providing

adequate flow capacity. Design blade element performance parameters are provided in Appendix 2, and airfoil definitions are provided in Appendix 3. Details of the original stator design are given in reference 2.

REDESIGNED STATOR

The redesigned stator had 50 blades, a hub solidity of 2.33, and an aerodynamic chord length of 2.628 inches (6.675 cm) at the root and 2.550 inches (6.487 cm) at the tip. The chord was 40 percent longer than the original stator chord in order to gain a higher loading capability for improving the stall margin. Although the stator solidity was increased about eight percent, the estimated blade-element losses for the redesigned stator did not exceed at any point the estimated losses of the original stator. Maximum-thickness to chord ratio was set to vary linearly from 0.041 at the hub to 0.072 at the tip, a distribution similar to that of the original stator which had demonstrated mechanical integrity and reasonable losses.

Low curvature entrance region airfoils were selected for the high Mach number hub sections. There was a gradual transition to nearly DCA airfoils at the lower Mach number tip sections. The choice of the nearly DCA tip sections for the redesigned stator was based on data that showed the DCA stators have lower losses than MCA sections with uncambered entrance regions when the inlet Mach numbers drop below 0.7 [ref. 6]. Transition between front and rear sections was set at the channel-entrance point on the suction surface for the hub section and at approximately half-chord for the tip section. Camber distribution was used to control throat area in blade channels. Design throat areas were selected using a correlation of minimum loss as a function of the ratio of throat-area-to-capture-area versus Mach number [ref. 6].

Incidence angles were set at approximately zero degrees to the suction surface at the hub (based on loss data from reference 6). Tip incidence angles were set at minus 6.1 degrees based on the P&WA™ correlation of DCA airfoils cascade data. Deviation angles were predicted using a P&WA correlation of cascade data plus a correction based on data from tests with the original stator [ref. 4].

Design blade element performance parameters are provided in Appendix 2, and airfoil definitions are provided in Appendix 3. Details of the stator redesign are given in reference 5.

BOUNDARY LAYER AND ENDWALL DEVICES

Stator Slit Suction

Boundary-layer suction slits were provided at the hub of the original-design stator and were utilized by the first and second fan-configurations to reduce total pressure loss and to attain higher loading without boundary layer separation. The slits were located at the intersection of the stator suction surface and the hub wall. Bleed flow requirements were based on analysis of Peacock's data [ref. 9]. Sonic bleed velocity was selected to prevent recirculation. The slits extended from 15 to 85 percent chord and were 1.160 inches (29.46 mm) long and, for the unslotted stator, were 0.017 inch (0.432 mm) wide. For the tests with the slotted stators,

the slit width was increased to 0.030 inch (0.762 mm) to evaluate effects of increasing boundary-layer suction flow. The slit arrangement can be seen in Figure 6. The redesigned stator was not provided with slit suction; instead this configuration was provided with variable angle capability to optimize overall performance.

Blade Slots

Slots were designed for the rotor and original-stator blades to increase stall margin by improving blade loading capability. The rotor blades had a tip slot at 20 percent chord that extended over the outer five percent of span and a larger slot at 70 percent chord that extended from 70 to 94 percent span from the hub. The original stator had slots at 20 percent chord that extended from each endwall to a distance equal to five percent of span. The redesigned stator was not slotted. Photographs of slotted rotor and stator blades are shown in Figure 5. Details of the slot designs are given in reference 4.

Casing Treatments Over Rotor Tips

Two rotor-tip casing treatments were designed to improve stall margin. The first treatment, used with the second fan-configuration (slotted rotor and slotted stator), was a honeycomb structure with cells inclined into the direction of rotor rotation at an angle of 70 degrees to a radial line (Figure 7). Cells were approximately 1/8 inch (0.318 cm) square and were 2.34 inches (5.943 cm) long, extending axially from 0.2 inch (0.508 cm) forward of the rotor leading edge plane to 0.6 inch (1.524 cm) rearward from the trailing edge plane [ref. 4]. Cells were open at both ends with an enclosed plenum on the outside. Provision was made to reduce plenum volume with an insert and to close off outer ends of the cells.

A skewed-slot rotor tip casing treatment [ref. 5] was also designed and was used with the redesigned stator (third fan-configuration). Slots were axial and slanted into the direction of rotor rotation at an angle of 60 degrees to the radial direction (Figure 8). Slots were 5/8 inch (1.588 cm) deep, 1/8 inch (0.318 cm) wide, and were separated by a land 1/16 inch (0.159 cm) wide. The slots extended from 20 to 80 percent of the axially projected rotor tip chord with a 0.162 inch (0.412 cm) wide partition separating each slot into equal length front and rear segments.

Vortex Generators

Vortex generators were designed [ref. 4] to add momentum to the boundary layer on the outer wall at the fan inlet. The vortex generators were paired to produce sets of counter-rotating vortices and were mounted on the outer case wall 8 inches (20.32 cm) upstream of the rotor leading edge. Figure 9 shows installed vortex generators along with honeycomb type casing treatment [ref. 4] over the rotor tips.

MECHANICAL DESIGN

Rig

The fan rig was designed with a cantilevered rotor which could be run without an inlet support structure and with a rotating nose cone for noise testing. For shakedown and performance testing, inlet struts were used to support an inlet fairing and a slip ring was used for rotor stress instrumentation. The inlet configurations for performance and noise testing are compared in Figures 10 and 11. An oil-damped bearing permitted operation through the range of test speeds without critical-speed problems. Provisions were made for extracting stator slit-suction flow and to mount flow-distortion screens upstream of the rotor. A split outer case permitted on-stand changes of rotor tip casing treatments. Chord angle of the redesigned stator could be reset at the test stand.

Rotor

The rotor blade thickness-to-chord ratio at the hub was limited to 0.07 by flow choking considerations which made it necessary to use either a partspan shroud or a pinned-root attachment to avoid low order resonances. The pinned-root attachment was selected so that partspan shroud losses could be avoided. Calculated stresses at 110 percent speed were well within the capability of the AMS 4928 titanium alloy material employed.

Stators

Calculated stator stress due to air loads was very low and well within the capability of the AMS 5613 stainless steel material employed. The vibration frequency of the original stator was dependent on the hub-end constraint provided by the plastic used to position the stator hub and to form the boundary-layer suction slit. The exact amount of constraint is unknown, but calculations showed that a cantilevered stator might flutter but a fixed or pinned-root stator would not. Some flutter occurred at high speeds during testing, but stresses did not limit the range of operation.

Mechanical properties calculated for the redesigned stator with low aspect ratio and a pinned-root hub attachment indicated low static stress and no vibration problems.

TEST FACILITY AND INSTRUMENTATION

The tests were conducted in a sea-level compressor test stand. The facility was equipped with a gas turbine drive engine and an exhaust system for boundary-layer control devices. A schematic of the test stand is shown in Figure 12. A description of the facility is provided in reference 3.

Inlet total-pressure distortions were created by attaching distortion screens to a support screen located 32 inches (0.813 m) upstream of the rotor leading edge. Radial distortion screens were designed to produce distortions extending over the outer or inner 40 percent of span. The circumferential distortion screen was designed to produce a distortion covering

a 90-degree segment of the annulus at the rotor inlet. All screens were designed to provide a distortion, $(P_{max}-P_{min})/P_{max}$, of 0.15 at design corrected flow. The photographs in Figure 13 show the support screen installed and the screens used to generate inlet distortions.

Performance measurements were made at nine radial locations defined by streamlines which passed the rotor trailing edge at 5, 10, 15, 30, 50, 70, 85, 90, and 95 percent span from the hub. The instrumentation locations are shown in Figure 14. (Changing to a split casing [ref. 5] necessitated shifts in the circumferential location of some instrumentation from that used in previous tests.) A detailed description of the instrumentation used during this program was given in earlier reports [ref. 3, 4, and 5].

Prior to this contract, the acoustic characteristics of the inlet plenum chamber had been investigated to determine the number and location of microphones needed to calculate the acoustic power output from the inlet of the fan stage. Both reverberation time measurements and sound pressure level distribution surveys were conducted; results of the surveys are presented in reference 3. Based on these data, eight microphones were positioned within the plenum chamber as shown in Figure 15. These eight positions were used for all the acoustic tests. One traversing microphone was positioned downstream of the stator trailing edge to sample downstream noise at blade-passing-frequency.

TEST AND DATA ANALYSIS PROCEDURES

The general test procedure for all the configurations consisted of: 1) shakedown phase in which stresses were surveyed, stall flow determined, and sample aerodynamic data obtained for instrumentation checkout; 2) performance tests in which detailed aerodynamic measurements were made; and 3) acoustic tests with microphones and only enough performance instrumentation to identify operating points. The acoustic tests were run with a rotating nose cone and no inlet support structure. Detailed test procedures were provided in earlier reports [ref. 3, 4, and 5].

Aerodynamic data were processed in two steps. In the first step, the data signals were converted from millivolts to temperatures and pressures and corrected by means of probe calibration data. Temperatures and pressures were circumferentially mass-flow averaged. Corrected weight and bleed flows (where applicable), corrected speed, and wake-blockage factors were calculated. In the second step, the information from step one was used as input to a streamline analysis program for the calculation of overall and blade element performance parameters. The second step was not used for circumferential distortion data. A complete description of the calculation procedure employed is provided in reference 3.

Tape-recorded noise data were processed through a wave analyzer having a 50 Hz bandwidth filter. The output of the analyzer was then recorded on a graphic-level recorder that yielded curves of sound pressure level as a function of frequency. From these traces, broadband noise and supersonic tip speed noise were evaluated. Blade-passage-frequency data were time averaged for 30 seconds at each operating point. A more detailed description of acoustic data analysis procedures may also be found in reference 3.

RESULTS AND DISCUSSION

In this section the aerodynamic performance of the third fan-configuration (slotted-rotor and redesigned stator) is discussed in relation to program objectives. Its aerodynamic and acoustic performance is compared with the performance of the first and second fan-configurations (unslotted rotor and stator and slotted rotor and stator), both of which gave inferior aerodynamic performance.

Aerodynamic performance is presented first in overall terms and then in blade element or spanwise variation terms. Most of the explanations for the overall results appear in the Blade Element Performance section because they depend on the spanwise variations. The acoustic test results are presented in a separate section following the aerodynamic performance.

AERODYNAMIC PERFORMANCE

Overall Performance

UNIFORM INLET FLOW

Fan stage and rotor performance maps for the third fan-configuration are presented in Figures 16 and 17, respectively. A constant-throttle operating line is shown on both the fan stage and rotor performance maps to provide a reference for comparing performance parameters at various test speeds. The operating line passes through the design speed line at fifteen percent stall margin, an acceptable value for useful application, and also through the design point. The operating lines correspond to a fixed-area fan nozzle with the ratio of nozzle-static-pressure to total-pressure equal to the reciprocal of the fan total pressure ratio and to temperature as determined by test efficiency. Design speed operating line performance parameters listed in this report correspond to data obtained at the solid points on Figures 16 and 17.

At design speed, fan efficiency on the operating line was 0.883, exceeding the design goal of 0.873. The peak efficiency measured at design speed was 0.886. Operating line rotor efficiency was 0.936, exceeding the design goal of 0.932. The peak rotor efficiency measured at design speed was 0.947.

Operating line performance parameters for the stage and the rotor are given in Table II. The values given do not represent particular data points but were taken from faired curves through data points on Figures 16 and 17. Because the two points at 65 percent design speed did not bracket the operating line, trends of pressure ratio and efficiency as functions of flow were established from previous tests [ref. 3 and 4].

TABLE II
OPERATING LINE PERFORMANCE PARAMETERS FOR
SLOTTED ROTOR AND REDESIGNED STATOR

Rotor Speed (% design)	Inlet Corr. Flow (% design)†	Stage Stall Margin (%)	Stage Pressure Ratio	Stage Efficiency (%)	Rotor Pressure Ratio	Rotor Efficiency (%)
65	66.1	29	1.183	90.1	1.190	94.8
90	88.6	21	1.380	90.3	1.402	95.5
100	97.5	15	1.474	88.3	1.508	93.6
110	102.8	7	1.535	80.0	1.584	88.5

†Design corrected flow = 185 lb/sec (83.8 kg/sec)

Figure 18 presents stage and rotor efficiencies as functions of percent design inlet corrected flow on the operating line shown in Figure 16; corresponding rotor speeds are also indicated. Maximum stage efficiency was 0.903 in the region of 88.5 percent of design corrected flow and 90 percent design speed. As shown in Figure 18, beginning at approximately 90 percent of design flow, there was a rapid fall-off in efficiency with increasing flow. The original design flow and pressure ratio were obtained at approximately 104 percent of design speed. Fan stage and rotor efficiencies at that point were 0.864 and 0.923, respectively (Figure 18).

Comparison of Performance of the Three Configurations

The most significant change in performance between the three fan-configurations was the improvement in stall margin obtained with the redesigned stator (third fan-configuration); there was also a slight increase in efficiency and a reduction in pressure ratio at design speed with this configuration. Other changes included a loss of about one percent in high speed flow capacity and an improvement in part-speed efficiency for both slotted rotor configurations (second and third fan-configurations) relative to the unslotted rotor (first fan-configuration). A composite performance map for the three fan-configurations is provided in Figure 19. In addition to the performance differences due to slotting and the redesigned stator, differences were also caused by the hub-slit suction of the original stator (both slotted and unslotted) and by the stagger angle variations of the redesigned stator. The differences in performance are discussed in the following sections; attempts are made to identify and explain the mechanisms causing the differences.

Stall Margin Comparison: Stall margin was identified as a potential problem area during the original design because of the high blade aerodynamic loadings required to obtain the design pressure ratio. Rotor design maximum diffusion factor was 0.54, occurring at 60 percent of span from the hub, and the stator maximum diffusion factor was 0.64, occurring at the hub (Figure 2). These high loadings indicated that the fan might have little stall margin.

Tests of the first fan-configuration demonstrated high efficiency, but the stall margin was considerably less than the 15 percent considered necessary for aircraft application. A region of intermittent stall was found at design speed (Figure 19). Flow at stall varied from 93.2 to 97.7 percent of design flow. An operating line with 15 percent stall margin relative to the low-flow side of the intermittent stall region would coincide with wide open throttle operation. Open-throttle performance was inferior to the performance obtained on the selected operating line (Figure 16) with pressure ratio dropping from 1.474 to 1.40 and efficiency dropping from 0.880 to 0.783 at design speed.

Modifications to this original configuration were designed and tested in an effort to improve stall margin while maintaining efficiency, flow capacity, and pressure ratio. In the first modification, rotor and stator blades were slotted (Figure 5) to improve their loading capabilities and reduce loss at high incidence. Boundary-layer-suction slits at the stator hub (Figure 6), which were effective in reducing stator losses in the unslotted blading, were widened to obtain additional loss reductions and to delay stator-initiated stalls. The addition of the slots and widened suction slits stabilized operation near stall so that stall at design speed occurred consistently at 92.7 percent of design flow. Stall tests without suction applied to the slits showed that most of the stability improvement was caused by the increased flow capacity of the widened slits. Figure 20 shows that without exhaust suction applied to the widened slits the stall margin dropped to approximately the level obtained at the high-flow side of the intermittent-stall region found in the previous test with the smaller slit and unslotted blading. With suction, the stall line coincided with the lowest flow obtained in the previous test. This stability improvement was significant, but it did not provide the amount of stall margin needed for aircraft applications.

Records of strain-gage signals with time, near and at stall, were often vital in indicating which blade row initiated stall by the onset of high vibratory stress in one row before the other. Characteristics of strain-gage records of stator-initiated and rotor-initiated stalls are shown in Figures 21 and 22. Figure 21 is an excerpt from the strain-gage record made during stall at 80 percent of design speed with uniform inlet flow and no stator-slit suction, indicating first signs of stall on stator strain-gages. Figure 22 shows records for the same speed and inlet conditions but with slit suction, indicating rotor-initiated stall. At speeds lower than 80 percent, all stalls were initiated by the rotor; at speeds higher than 80 percent, all stalls were initiated by the stator, with or without slit suction.

The stator was then redesigned with increased hub-convergence and increased solidity to reduce loadings and with reduced aspect ratio to improve loading capability. Variable stator-angle settings were also provided so that the stator could be reset on the test stand to optimize fan performance. Tests of this third fan-configuration showed that the redesigned stator raised the fan stall margin at design speed by seven percentage points over that obtained with the slotted stator and slit suction by decreasing the stall flow from 92.7 to 87.1 percent of design flow and by increasing stall pressure ratio from 1.497 to 1.506 (Figure 19). Maximum flow capacity decreased only slightly and efficiency increased slightly; thus the improved stall line represents a gain in useful stall margin. Table III provides a comparison of design speed performance at 15 percent stall margin for the three basic fan-configurations.

TABLE III
PERFORMANCE OF THE THREE FAN CONFIGURATIONS
AT DESIGN SPEED WITH 15 PERCENT STALL MARGIN

Parameter	Configuration 1 Unslotted Rotor and Stator	Configuration 2 Slotted Rotor and Stator	Configuration 3 Slotted Rotor and Redesigned Stator
Efficiency at 15% Stall Margin	0.783†	0.788	0.883
Pressure Ratio at 15% Stall Margin	1.40†	1.401	1.474

†Assuming stall occurs at the low-flow side of the intermittent-stall region. If stall is assumed to occur at the high-flow side of the intermittent stall region, 15 percent stall margin falls below the open-throttle point.

It is acknowledged that the increased stall margin with the redesigned stator was obtained by reducing stator diffusion. The stator exit average Mach number was approximately 0.58 during fan operation with 15 percent stall margin, a value too high for some applications. An alternative solution for engine fans would be to use the splitter to limit the redesign to the hub region where high loadings occurred. If a splitter isolated the fan duct flow from the primary flow, there would be no requirement for static-pressure and flow-angle continuity between the separated streams. Convergence, curvature, and exit swirl could be used to reduce primary-flow stator loadings. Original Mach number levels and axial exit-flow could be retained for the exit-guide-vane in the fan duct flow.

Tests were run to investigate the effect of resetting stagger angle of the redesigned stator to optimize performance at design speed. The best combination of stall margin, efficiency, and flow capacity at design speed was obtained with the nominal stator-setting (i.e., stator at design setting), as shown by Figure 23. The highest stall-line was obtained with the stator closed (reset to reduce incidence angle) 10 degrees. This higher stall-line was obtained at the expense of flow capacity and efficiency at an acceptable stall margin. A higher stall-line but lower efficiency was also obtained with the stator opened 5 degrees. This latter stall-line improvement can be explained as a result of spanwise shift of stator loading as discussed under Blade Element Performance.

Performance tests over a range of speeds with the stator in the nominal and 10 degrees closed settings indicated that closing the stator was effective in raising the stall line at high speed but not at part-speed. Figure 24 shows that a significant improvement in stall line was obtained at 110 percent of design speed but that there was no improvement at 90 percent speed. Flow capacity was reduced at all speeds.

Flow Capacity Comparison: Maximum flow capacities of the first and second fan-configurations and of the third fan-configuration with different stator setting angles are shown on Figure 25. Maximum flow with the original unslotted blading exceeded the

design flow although flow was lower than design for near-design pressure ratios and efficiencies (Figure 19). Slotting reduced flow capacity by 1.1 percent. Another flow reduction was indicated when the slotted stator was replaced by the redesigned stator; however, the 0.4 percent decrease indicated is close to the repeatability (0.3 percent) of the flow measuring system. Opening the stator did not increase flow capacity, indicating that the rotor limited the stage flow capacity with nominal and opened stator setting angles. Maximum flow decreased by 2.1 and 7.2 percent when the stator was closed 5 and 10 degrees, respectively.

Fan flow capacity can be related to choking in channels between adjacent airfoils. Table IV lists radially mass-flow-averaged values of minimum-area ratio (A/A*)† of the slotted rotor and redesigned stator (third fan-configuration) for maximum-flow operating points at design speed with the stator at nominal and 10 degrees closed settings; the underlined values shown are flow-limiting values. The operating line point gives the minimum A/A* levels at which good pressure ratio and efficiency were obtained.

TABLE IV
SPANWISE AVERAGE OF MINIMUM A/A* IN SLOTTED ROTOR AND REDESIGNED STATOR BLADE CHANNELS AT DESIGN SPEED

Operating Condition	A/A* Rotor	A/A* Stator	Percent Design Flow
Open throttle, stator nominal	<u>1.021</u>	1.016	99.2
Open throttle, stator closed 10 degrees	1.100	<u>1.001</u>	92.1
Operating-line stator nominal	1.049	1.095	97.5

Maximum flow with the nominal stator-setting (also with the opened stator-setting) occurred at a rotor minimum A/A* level of 1.021 (before slotting, the rotor obtained a minimum A/A* of 1.010 at open throttle) and with the stator closed 10 degrees at a stator minimum A/A* level of 1.001 in the stator. The low minimum A/A* level in the stator may have been due to the large annulus blockage (actual-area/effective-area) of 1.041 used at the stator inlet in the streamline calculation to match calculated static pressure with measured wall static pressure.

The slotted rotor blade had about one percent lower measured flow capacity than the unslotted blade (Figure 25) because of the positions of the slot entrance and exit relative to the channel between blades, as shown by Figure 26. Local channel widths normal to a midgap

†Minimum values of A/A* for each of nine blade-element channels were radially mass-flow averaged to obtain the blade-throat A/A* value used to correlate flow capacity. Blade-element A/A* ratios were calculated using the method described in reference 2, except that the test flow conditions at blade edges were used instead of design flow conditions.

streamline are represented in the figure by diameters of the circles drawn in the channel. Viewing the channel area in this way, it can be seen that relative to the midgap streamline, the slots discharged into the channel upstream of the slot entrance on the following blade. Figure 27 shows design A/A* ratios as functions of axial location in the passage at midgap at 73 and 91 percent of span from the hub (the slot extended from 70 to 94 percent span). A three percent drop in A/A* (corresponding to the slot design flow rate) is shown for the channel sections carrying additional flow. The calculated flow capacity at choke was reduced by 1.0 percent at 73 percent span and by 2.8 percent at 91 percent span due to the slotting geometry used.

Efficiency Comparison: Figure 19 shows that all configurations attained maximum efficiencies only slightly higher than the original design-estimate. Since the original efficiency estimate was based on conventional correlations of blade-element loss [ref. 2], and since configuration changes had only minor effects on efficiency, the high level of efficiency appears to be the result of the low tip-speed in relation to the fan pressure ratio. Figure 28 shows a map of rotor and stage static pressure ratios as functions of flow. The reaction, defined as the ratio of rotor-static-pressure-rise to stage-static-pressure-rise [ref. 10], was below 0.6, a low value for a fan. The static pressures used to calculate the reaction ratios were arithmetic averages of hub, mean, and tip values from the streamline calculation.

Rotor and stator total pressure recoveries† were nearly equal, as shown in Figure 29, which is characteristic of stages with reactions near 0.5. Reactions in this range generally give a higher stage recovery (product of rotor and stator recoveries) than stages with very high or very low reactions. At the operating-line point at design speed, the rotor recovery was 0.974 and the stator recovery was 0.978, giving a stage recovery of 0.953. The recoveries of both airfoils (i.e., rotor and stator airfoils) fell rapidly as choke was approached. Figure 30 shows total pressure recoveries of the slotted rotor and the redesigned stator versus the spanwise-average minimum A/A* for the open-throttle design speed data points shown in Figure 23. The higher minimum A/A* level at which rotor recovery fell relative to stator recovery is partly attributable to rotor slot flow which decreased choked flow at design speed by approximately one percent.

Tests with and without boundary-layer suction through slits at the stator hub showed that suction improved stator total pressure recovery. The average recovery on the operating line of the unslotted original stator with slit suction was 0.9777 and 0.9764 without slit suction. The increase in efficiency corresponding to the increase in recovery was 0.005 for these operating-line points. At open throttle, where stator hub losses were more severe, slit suction improved efficiency by 0.015 [ref. 3]. The net efficiency gains for operating-line and open-throttle points were 0.003 and 0.013, respectively, after accounting for the 0.2 percent bleed flow.

Small efficiency gains were obtained in each successive fan configuration. Figure 19 shows that slotting the rotor and stator and increasing the width of the boundary-layer suction-slit at the stator hub raised part-speed efficiency by approximately 0.02. This increase resulted from gains from both the rotor and the stator. Rotor efficiency increased 0.016 and the stator had a higher total-pressure ratio (recovery), giving an efficiency improvement of

† Recovery is defined in Appendix 1

approximately 0.008. Design speed efficiency improved when the slotted stator was replaced by the redesigned stator even though the redesigned stator did not have the benefit of slit suction. Details of these performance changes are discussed in the Blade Element Performance section.

DISTORTED INLET FLOW

Inlet flow distortions were generated by means of screens (Figure 13) located one rotor-diameter upstream of the rotor leading edge. Three types of inlet distortions were investigated: tip-radial, hub-radial, and circumferential. Radial profiles of rotor inlet total pressure with the tip-radial and hub-radial distortions at 95 percent speed are shown in Figure 31. A maximum distortion parameter, $(P_{max} - P_{min})/P_{max}$, of 0.147 was obtained with the tip distortion and 0.100 was obtained with the hub distortion. A contour map of rotor inlet total pressure with circumferential distortion at 95 percent speed is presented in Figure 32. For this pattern, the distortion parameter at 50 percent span was 0.122. Maximum test-speeds during the distortion tests were held to 95 percent because of flutter. Flutter in the first-bending mode was encountered with both slotted and unslotted rotor blades at 97 percent of design speed with tip-radial distortion. Test speeds were therefore held to a maximum of 95 percent to avoid operating at high stresses. All distortion tests were run with this same maximum speed to simplify comparing results.

The third fan-configuration (slotted rotor with redesigned stator) was the only configuration tested with all three types of distortion. The first fan-configuration (both rotor and stator unslotted) was tested with only tip-radial and circumferential distortions, and the second fan-configuration (both rotor and stator slotted) was tested with only the tip-radial distortion. Because only the third fan-configuration was tested with all three types of distortion, the comparison of the effects of different types of distortion on performance is limited to that configuration. A comparison of the performance exhibited with tip-radial distortion is made for all three fan-configurations, and performance with circumferential distortion is compared for the first and third fan-configurations.

In Figure 33 the overall performance obtained with the three types of distortion is compared with the performance obtained with uniform inlet flow. The distorted flow operating line shown in the figure is higher than the operating line for the uniform flow and was calculated by assuming that nozzle-exit static pressure was equal to the maximum value of total pressure at the rotor inlet. Nozzle exit values of P/p were obtained by dividing the mass-flow-average total-pressure ratio, P_{12}/P_5, by $P_{5\ max}/P_{5\ mass\text{-}flow\text{-}av}$. The resulting Mach numbers for the distorted flows were lower than for uniform flow, and the operating lines were raised accordingly. Operating lines for the three types of distortion were separated by less than one percent of design corrected flow, and the distorted-flow operating-line shown in Figure 33 is the middle of the band of operating lines for the three distortions. An intersection of the operating line with a speed line locates an operating line efficiency point for a particular flow rate. The operating line efficiency curves in the figure were obtained by drawing a smooth curve through these efficiency points.

Tip-radial distortion reduced stall margin significantly and was most severe at low speeds. This sensitivity to distortions at speeds where with uniform inlet flow the rotor controlled

stall indicates that the loss in stall margin was due to rotor stall. Circumferential distortion had little effect on stall margin, but hub-radial distortion raised stall margin. This increase in stall margin with hub-radial distortion was unexpected and appears to be similar to the result obtained in another program in which a hub baffle raised stall margin [ref. 11]. Efficiency was reduced 0.01 and 0.02 by circumferential and hub-radial distortions, respectively, at 95 percent of design speed and tapered off to negligible reductions at 80 percent of design speed. The tip-radial distortion reduced efficiency by 0.021 at 95 percent speed and by 0.015 at 80 percent speed. Stall margin and operating-line adiabatic efficiency are presented as functions of test speed in Figure 34 for the three types of distortion investigated; the changes shown are relative to performance with uniform inlet flow.

All three fan-configurations had approximately the same stall line when tested with tip-radial distortion, as shown in Figure 35. As can be seen in the figure, the efficiencies of the third fan-configuration were 0.02 to 0.03 better than for the second fan-configuration, and the second fan-configuration efficiencies were 0.01 to 0.02 better than the first fan-configuration. With circumferential distortion, the efficiencies of the third fan-configuration were 0.04 to 0.05 better than the first fan-configuration (shown in Figure 36). The similar stall lines at lower speeds with circumferential distortion and at all speeds with tip-radial distortion indicate rotor-controlled stalls. The higher stall line of the third fan-configuration at high speed with circumferential distortions indicates that at this operating condition the first fan-configuration had a stator initiated stall.

Comparison of Inlet and Exit Distortions

Tip-radial distortion produced the spanwise meridional velocity-profiles at the fan inlet and exit shown in Figures 37 and 38, respectively. The data were obtained at the near-stall test point, the point closest to the distorted-flow operating-line, at 95 percent of design speed (Figure 33). Meridional velocity profiles of operating-line and near-stall test points with uniform inlet flow are shown for comparison. Tip-region velocity at the fan inlet (Figure 37) was approximately the same with uniform and distorted flows at near-stall data-points. Plots of exit velocity profiles (Figure 38) show that the distortion was not reduced appreciably by the fan. Both the inlet and the exit distortion patterns were approximately the same at the operating line and at near-stall.

Hub-radial distortion produced the inlet and exit velocity profiles shown in Figures 39 and 40, respectively. These figures show that on the operating line the fan reduced the velocity defect at the hub and that between the operating line and near-stall points a very large velocity defect developed at the hub. Because of the large region of past-axial exit-flow at the hub, instability had been expected with hub-radial distortion. Figure 41 shows that for past-axial rotor exit flow, decreasing exit velocity reduces the work done on the fluid by the rotor. Hub-radial distortions had been expected to reduce rotor exit velocity near the hub and, thus, reduce work, total pressure, and flow velocity. Figures 39 and 40 show, however, that although the rotor inlet velocity was low at the hub with the hub-radial distortion, the rotor exit velocity profile was not much different than with uniform inlet flow and that distortion was reduced except near stall.

Differences in rotor efficiency profiles between radially distorted and uniform inlet flows are shown in Figure 42 for operating-line data points at 95 percent of design speed. The efficiency values shown are from streamline calculations which used the radial distributions of measured rotor-inlet flow conditions and radial distributions of rotor exit conditions determined from stator-exit free-stream total pressures and circumferentially mass-flow-averaged total temperatures. Efficiency rose in the distorted regions and fell in the undistorted regions relative to the values obtained with uniform inlet flow. This result was due to a large increase in work in the distorted area without a corresponding increase in loss. Similar results were obtained in the radial distortion data reported in reference 12.

Contour maps of rotor inlet total pressure, stator inlet total pressure, and stator inlet total temperature are shown in Figures 32, 43, and 44, respectively, for a particular test point with inlet circumferential distortion and the redesigned stator stage. The maps were generated from a 95 percent speed data-point near the operating line. The shaded portions in each map indicate areas where either pressures were lower or temperatures were higher than average. Comparing the pressure maps for the rotor and stator leading edges indicates that after passing through the rotor the distorted area spread out and that radial gradients developed which were stronger than the circumferential gradients. The maximum value of the distortion parameter, $(P_{max} - P_{min})/P_{max}$, increased from approximately 0.13 at the rotor leading edge to 0.21 at the stator leading edge; however, the latter occurred only very locally near the stator hub. The temperature contour map in Figure 44 also shows that the steepest gradients were radial, with highest temperatures at the outer case in back of the distortion screen. A comparison of stator-inlet temperature and pressure maps (Figures 44 and 43) shows that the temperature distortion (region of higher than average temperature) was displaced circumferentially in the direction of rotation relative to the pressure distortion (region of lower than average pressure). A similar displacement pattern was evident in test results reported in reference 12. Again the present rotor design, with past-axial turning near the hub, could increase the radial gradients as previously discussed.

Performance With Casing Treatment

Casing treatments over the rotor tip were used to improve stall margin by increasing the load capability of the rotor. Skewed-slot casings (Figure 8) were tested with the third fan-configuration, and honeycomb casings (Figure 7) were tested with the second fan-configuration. Vortex generators (Figure 9) also were tested with the second fan-configuration, both in combination with the honeycomb casing and with the solid casing.

The skew-slot casing produced significant gains in stall margin with all three types of inlet-flow distortions. Effects of the skewed-slot case with the third fan-configuration are shown on Figures 45 through 48 which compare performance maps for each type of distortion with solid and skewed-slot casings to baseline performance with uniform inlet flow and the solid casing.

In Figure 45, performance with tip-radial distortion and solid casing is compared with performance with a skewed-slot casing. The skewed-slot casing increased stall margin by approximately seven percentage points at all speeds. Efficiency was unchanged at 95 percent of

design speed but dropped about 0.01 at lower speeds. Curves of pressure ratio versus flow were unchanged except that they were extended to lower flows at stall. With distortion, the stall line remained lower than with the uniform inlet flow, but the difference was small at high speeds.

In Figure 46, performance maps with hub radially distorted inlet flow for the solid casing are compared with the skewed-slot casing. Stall margin increased by 10 percent, but efficiency at 95 percent of design speed decreased approximately 0.025. Figure 47 shows that rotor-tip inlet velocity at stall was lower with the skewed-slot casing than with the solid casing and that velocity levels at the tip were approximately the same at stall with tip-radial and hub-radial distortions.

Figure 48 compares performance with circumferential distortions for solid and skewed-slot casings. Stall margin improvements of 2.5, 7.5, and 14 percent were obtained at 95, 90, and 80 percent design speeds, respectively, with the skewed-slot casing. Efficiency was reduced by 0.025 at 95 percent speed and 0.010 at 80 percent design speed.

Performance with uniform inlet flow for solid and skewed-solid casings is compared in Figure 49; all differences were small. The skewed-slot casing decreased stall margin at 95 and 100 percent of design speed, caused no change at 90 percent speed, and raised stall margin at 80 percent speed. The improvement in stall margin occurred where rotor stall occurred with the solid casing, and no improvement occurred at higher speeds where the stator stalled. Efficiency was reduced approximately 0.015 at design speed and 0.010 at 95 and 80 percent design speeds.

The combination of the honeycomb casing over the rotor tip and vortex generators provided approximately the same improvement in stall margin as obtained with the skewed-slot casing but the efficiency penalty was an unacceptable 0.070. The honeycomb alone gave slightly less stall margin but the efficiency penalty stayed at 0.070. The vortex generators alone had no effect on stall margin but reduced efficiency by 0.015. Tests with the honeycomb casing and vortex generators are discussed in detail in reference 4.

Blade Element Performance

This portion of the report is devoted to a discussion of spanwise distributions of performance parameters. Blade-element efficiency and pressure ratio are related to losses, deviation angles, and loading parameters. Fan stall is correlated as a function of blade-element loading. Minimum losses are correlated as a function of blade-element loading, and ranges of low-loss incidence angles are presented.

Blade-element percents of span given in this report designate the percent span at which design streamlines pass through the rotor trailing edge. These design streamlines pass other blade edges at the percent spans given in Table V.

TABLE V
SPANWISE LOCATIONS OF BLADE ELEMENTS (PERCENT FROM HUB)

Nominal % Span	Rotor Inlet	Rotor Exit	Original Stator Inlet	Original Stator Exit	Redesigned Stator Inlet	Redesigned Exit
5	4.8	5	4.9	5.2	5.4	4.3
10	10.3	10	9.5	9.3	10.6	8.9
15	16.0	15	14.6	14.1	15.7	13.1
30	32.5	30	29.4	28.2	30.7	27.8
50	53.3	50	49.7	48.2	50.6	47.8
70	72.9	70	70.0	68.6	70.4	68.5
85	85.5	85	84.9	84.0	85.3	84.5
90	91.0	90	89.9	89.4	90.2	89.7
95	95.4	95	94.7	94.5	95.1	95.3

ROTOR

Spanwise distributions of total pressure and temperature ratios and efficiency at the exit of the slotted rotor with the redesigned stator (third fan-configuration) for design-speed, uniform inlet flow operating points are compared to the original design intent in Figure 50. Solid symbols show the data from the operating line point with 15 percent stall margin. Pressure ratio at the tip was generally lower than the design goal, reaching design level only near stall. Temperature ratio followed the same trends except at open throttle where the large drop in pressure ratio was not accompanied by an equivalent drop in temperature ratio. The efficiency profile was essentially constant for all throttle settings from the selected operating line to stall but dropped off at the tip at open throttle. Efficiency was higher than the design estimate between 18 and 85 percent of span and below the estimate at both endwalls.

Slotting the rotor changed the radial distribution of work as shown by spanwise profiles of pressure ratio and efficiency at design speed (Figure 51). The total pressure ratio for the slotted rotor was higher at the tip (region of slot) and lower at the hub than for the unslotted rotor for the same overall rotor pressure ratio; efficiency profiles were nearly identical. At 80 percent of design speed (Figure 52), the slotted rotor also had a higher tip pressure ratio but a lower midspan pressure ratio. Efficiency of the slotted rotor was 0.04 higher at the tip, tapered off to no change at 20 percent span from the hub, and was slightly lower near the hub. The performance of the slotted rotor was affected slightly by the stator. In Figure 53, spanwise distributions of rotor pressure ratio and efficiency obtained with the third fan-configuration are compared with those obtained with the second fan-configuration. The rotor pressure ratio at the hub and midspan was lower with the redesign stator than with the original stator. Work (i.e., temperature rise) also decreased at the hub

and at midspan so that efficiency was increased by approximately 0.03 at the hub. Wall static pressures at the rotor exit and stator inlet also indicated a redistribution of flow and/or work. As can be seen from Figure 54, overall radial gradients of static pressure at both stator inlet and rotor exit were smaller with the redesigned stator than with the slotted original-stator. This change in rotor performance was not predicted by the streamline program at the time the stator was redesigned. The effect of these changes on rotor overall performance was to increase efficiency slightly and to reduce pressure ratio slightly.

Spanwise distributions of slotted rotor incidence and deviation angles, loss coefficients, and diffusion factor for the near-operating-line data point at design speed are compared to design estimates in Figure 55. Rotor tip deviations exceeded the design estimate, which explains the low pressure and temperature ratios at the tip shown in Figure 50. Midspan losses were lower and endwall losses were higher than design estimates, supporting the efficiency profile in Figure 50. Rotor incidences were slightly higher than the design estimate due to the inability of the stage to attain design flow at design speed and pressure ratio. Performance parameters of the rotor blade elements of the different rotor configurations are compared to each other and to design estimates in the following sections.

Rotor Loss

The spanwise distributions of total-pressure loss coefficients, $\bar{\omega}$, for test points near the operating lines are compared in Figure 56 to the original loss estimate. Data are shown for all three fan-configurations for tests at 80 and 100 percent of design speed. Essentially the same loss distribution was obtained with all three configurations. Overall efficiency was predicted with reasonable accuracy, indicating that radial integrations of test and predicted losses were in much better agreement than individual blade element losses.

Predicted endwall loss increments were calculated for the design speed, operating line, datapoint using the method of reference 13. The endwall loss increments were added to the "two-dimensional" losses (faired with the present data) to obtain the predicted losses in endwall regions (Figure 56). The correlation was in better agreement with test endwall losses than the predicted loss profile.

Plots of the loss parameter $\bar{\omega} \cos\beta_2/2\sigma$ versus diffusion factor, D, are compared in Figure 57 for both the unslotted and slotted rotor blade elements [ref. 3 and 5]. The correlation line on each plot is parallel to the loss-parameter versus diffusion-factor curve given in reference 14 for hub and midspan blade elements, but all the levels have been readjusted for spanwise position effects to fit the data on Figure 56. Figure 58(a) shows the reference 14 correlation, and Figure 58(b) shows the spanwise position adjustment (relative to the hub and midspan elements of reference 14) utilized for the lines on Figure 57. The level adjustment for proximity to endwalls was the same in both hub and tip regions. Tip blade elements of this rotor, Figure 57, had lower loss parameters than the band of tip data shown in Figure 58(a) taken from reference 14. For midspan blade elements, a minimum value of loss parameter of 0.002 is shown in Figure 57 for low values of diffusion factor.

No significant difference in loss was seen at design speed between the slotted and unslotted blades outboard of 70 percent span where slots were located (Figure 56). The slotted rotor did have lower losses in the hub region. Similarly, the slotted rotor hub losses were lower with the redesigned stator than with the slotted stator. The lower losses for the same blade elements apparently accompanied the changes in spanwise distributions of work (Figures 51 and 52), but the mechanism causing the loss reduction has not been determined. These loss reductions obtained by slotting raised rotor overall efficiency by approximately 0.003 at design speed and 0.016 at 80 percent of design speed.

Rotor Loading

Figure 59 compares the predicted spanwise profile of diffusion factor, D, at design point with the profiles obtained near the operating-line with 15 percent stall margin and near stall at 80 and 100 percent of design speed. The design loading level was higher than the level at which 15 percent stall margin was obtained. Maximum loadings occurred at the tip for both speeds and throttle settings. A correlation was obtained between rotor stall and rotor loading at 90 percent span from the hub for the third fan-configuration, as shown in Figure 60. The rotor stalled whenever the D-factor at 90 percent span reached 0.63. Figure 61 shows similar plots for tests with the unslotted and slotted rotor and stator. Rotor tip D-factor reached 0.645 at stall with unslotted blading and 0.63 with the slotted rotor, which indicates that slotting reduced rotor loading capability. The loading limit of the slotted rotor was the same when run with either the slotted or the redesigned stator.

Rotor Deviation

Rotor deviation angles at minimum-loss incidence for the three fan-configurations are compared with the design values in Figure 62. The line drawn through the slotted rotor deviation angles favors the data obtained in tests with the third fan-configuration because the best fan performance was obtained with this configuration and because better agreement was found between blade element data at all operating speeds than with the second fan-configuration. The slotted portion of the slotted blade (outer 30 percent span) had a lower deviation than the unslotted blade; however, the deviation was higher for the unslotted portion of the slotted blade resulting in a net reduction in rotor work. The phenomenon causing these changes has not been determined.

The design deviations were predicted using Carter's Rule plus an adjustment [ref. 2]. Deviation angles were not predicted accurately, particularly near the tip where the rapid increase in deviation outboard of 85 percent span was not anticipated. A better prediction was made for the hub region where cascade data were used.

Rotor Incidence

Optimum incidence was considered to be the value at the center of the low-loss incidence range, as defined on Figure 63, for 90 percent span. Optimum incidence angles versus span for the slotted rotor (from tests from the third fan-configuration) and unslotted rotor (from tests from the second fan-configuration) are compared at design speed to design values

in Figure 64. Choking problems limited flow and resulted in high levels of optimum incidence angles relative to design values. However, loss levels were not adversely affected by the high incidence angles. Figure 65 presents plots of total-pressure-loss coefficient versus incidence for slotted rotor blade elements (obtained with the third fan-configuration) at 10, 50, and 90 percent of span. Exact incidence alignment was not required for low loss at 10 and 50 percent of span, but at 90 percent span, a supersonic relative flow region, alignment was more critical due to diminished operating range. At high speeds, rotor choking limited negative incidences and raised losses rapidly as the limits were approached. Losses increased more slowly at high positive incidences where at high speeds the stator initiated stall, indicating that additional channel area could have provided additional range at negative incidences.

STATOR

Spanwise distributions of redesigned-stator incidence and deviation angles, loss coefficient, and diffusion factor for the near-operating-line data point at design speed are compared to redesign estimates in Figure 66. Redesign estimates were made using 100 percent corrected design speed data from the second fan-configuration tests at a corrected weight flow of 179.7 lb/sec (80.502 kg/sec) [ref. 5]. The data were in good agreement with redesign estimates except that incidence angles were one to three degrees lower, endwall region losses were higher, and deviation angles lower than the estimated values. Both sets of incidence angles were taken from streamline calculations in which blockages were adjusted to obtain agreement between measured and calculated wall static pressures. Three percent more blockage was required for the redesigned-stator calculations (from third fan-configuration tests) than for the original-design stator (second fan-configuration tests). The effect of increased blockage was to reduce incidence angles approximately 1.5 degrees.

Spanwise distributions of performance parameters for the unslotted and slotted original-stator (both with suction) blade elements are compared to the original-design estimated in Figure 67. The data presented are from design speed data points near the operating line, which had the same stage-pressure-ratio. Incidence angles were different from those predicted due to the unexpected radial distribution of flow from the rotor, but other parameters were in reasonably good agreement with predictions. Slotting did not have a major effect on stator performance. Incidence was increased because flow was reduced by rotor slots. Loss near the hub increased slightly with slots despite the widened suction-slit but was unchanged near the tip.

Stator Loss

Spanwise distributions of total-pressure loss coefficient, $\bar{\omega}$, are compared to the estimated loss coefficients in Figure 68. Design speed and the 80.0 percent design speed operating-line data are presented in the figure for the three fan-configurations; the coefficients for the first and second fan-configurations are with slit-suction. All stators had low losses at midspan and high losses near endwalls and were in reasonable agreement with the level and profile of estimated losses.

Redesigned-stator losses were lower at midspan, consistent with reduced loading, but endwall losses were higher than those of the original stator. Increased endwall losses appear to be

due to larger corner boundary layers with the longer-chord redesigned stator (a relationship described in reference 13). Figure 69 presents contour maps of total pressure downstream of original and redesigned stator tips, showing that the region of corner loss was larger and had lower pressures for the redesigned stator.

Hub region losses of the original stator were reduced by boundary layer suction through slits at the corners formed by stator suction surfaces and the hub wall (Figure 70). Tests of the original stator were run with both suction and with the slits covered to show the effects on loss. Profiles of $\bar{\omega}$ for the inner half-span showed significantly lower losses inboard of 30 percent span with corner-boundary-layer suction.

Endwall loss increments (calculated using the correlation of reference 13) are plotted in Figure 68 for comparison with the data. The "two-dimensional" losses to which endwall increments were added were extrapolated from the redesigned-stator midspan $\bar{\omega}$ profile. Endwall agreement with data was reasonably good, but this method does not offer an improvement over the loss parameter ($\bar{\omega} \cos \beta_2/2\sigma$) versus D-factor correlation used to estimate stator blade element losses. A correlation of $\bar{\omega} \cos \beta_2/2\sigma$ versus D-factor for these stator data is presented in Figure 71. All lines shown in Figure 71 are parallel to the correlation given for stators in reference 14 with levels of $\bar{\omega} \cos \beta_2/2\sigma$ adjusted for spanwise position effects. Figure 72(a) shows the reference 14 correlation, and Figure 72 (b) shows the spanwise level adjustments (relative to Figure 72(a)) utilized for the lines on Figure 71. Level adjustments are symmetrical about midspan.

Tests showed that the loss-incidence relationship for the redesigned stator was not greatly affected by stator setting angle. Figure 73 shows a single line passing through data points on a plot of loss coefficient, near the tip, versus incidence angle for all stator settings. However, spanwise distributions of loss did change with stator setting angle near stall, as shown by Figure 74. Higher incidence angles with the stator opened five degrees gave much higher losses near the tip. The high tip-losses decreased efficiency but forced flow toward the hub, relieving hub loading and increasing stall margin (Figure 23).

Stator Loading

Stator loading was the critical parameter in determining fan stall at high speeds. The loadings of the redesigned stator were reduced, relative to the original stator, and an increase in stall margin of seven percent was obtained at design speed. The spanwise profiles of D-factor for the slotted original-stator and the redesigned stator at design-speed test points near the operating line (chosen for the redesigned stator fan-configuration) and near stall are compared in Figure 75 to their predicted profiles. The D-factors for the slotted original-stator near the operating line are near the predicted values and are only 0.005 to 0.020 lower than the D-factors near the stall line, which explains why the stall margins of the original-stator fan-configurations were inadequate for practical applications. The D-factors for the redesigned stator at near stall are at approximately the same levels as for the slotted original-stator, but the predicted level and the actual level near the operating line are 0.07 to 0.10 lower than at near stall. The increase in difference between the operating-line and the stall loading levels permitted the redesigned stator fan-configuration to run at lower flows and higher pressure ratios (Figure 19) before stalling.

Fan stall at high speed was related to stator loading limits, as shown in Figures 60 and 61. Figure 60 shows this correlation of limiting D-factors for the third fan-configuration (slotted-rotor and redesigned stator), and Figure 61 shows a similar correlation for the first and second fan-configurations. The limiting loading for the original stator with boundary-layer suction through slits at the stator hub was 0.62. This was approximately the same limit obtained with the redesigned stator which had a lower aspect ratio but no slit suction. The limiting D-factor of the original stator without slit suction was 0.59, indicating that slit suction raised the loading capability of the original stator and that reduced aspect ratio raised the loading capability of the redesigned stator relative to the original stator. Mach numbers at blade element leading edges for the data points, shown in Figures 60 and 61, ranged from 0.52 to 1.18, indicating that in these tests the limiting loadings were independent of Mach number.

The fan with the unslotted original-stator had a region of intermittent stalls at design speed (Figure 19). Stator hub D-factors in this region ranged from 0.59 to 0.62. This instability was not seen with the slotted stator which also had suction slits; however, its slits were twice the width of those of the unslotted stator. When suction was not used with the slotted stator, the stator stalled at a stator hub D-factor of 0.59, coinciding with the low stall-margin (high flow) edge of the intermittent-stall region obtained with the unslotted stator with narrower suction-slits. The improved stability of the slotted stator is believed to be the result of the wider suction-slits and not of the airfoil slots as reported in reference 4. Slit flow was not measured accurately in the unslotted stator (narrow slit) test; therefore, the flow difference between the wide and narrow slits is unknown. Total flow through the wider suction slits was 0.22 percent of the total fan flow at the near-stall, design-speed test point. It was estimated that the narrow slit had between 40 and 50 percent of the flow capacity of the wider slit.

Tests with the redesigned stator reset open and closed (increasing and decreasing incidence angles respectively) showed that maximum stator loading increased for lower incidence angles. Figure 76 shows that the limiting stator D-factor, at 10 percent span from the hub, increased for the low incidence angles obtained with the stator closed 10 degrees. When the stator was opened 5 degrees, the loading shifted toward the tip. This redistribution gave a more uniform level of loading across the span (Figure 77), decreasing loading in the previously critical hub-region. It was not determined whether limiting loadings occurred at the hub or at the tip of the opened stator.

Stator Deviation

Measured stator deviation-angles at minimum stator loss are compared with design predictions in Figure 78. Measured and predicted values are shown as functions of spanwise positions for both the original and redesigned stators. Deviation angles of the original stator were based on Carter's rule plus adjustments for spanwise position [ref. 2], and deviation angles of the redesigned stator were predicted based on P&WA's cascade data correlations with adjustments; original adjustments were based on reference 6 data, and redesign adjustments were based on reference 4 data.

Tip deviations for the redesigned stator were about seven degrees lower than for the original stator. A five-degree difference was predicted due to the chordwise movement of the maximum-camber location in the redesigned stator tip. Agreement between predicted and test deviations was good for both stator configurations except at five percent span, where measured angles were four to six degrees lower than predicted. For the redesigned stator, deviation angles for hub-region blade elements (5, 10, and 15 percent of span) were highest near optimum incidence and decreased rapidly as incidence was increased, Figure 79(a). Deviation angles for midspan and tip-blade-elements changed very little, increasing slightly with increasing incidence, Figure 79(b). Similar trends in the deviation-incidence relationship were seen in the original-stator data [ref. 4 and 3].

Stator Incidence

Optimum-incidence angles for the redesigned stator were one to two degrees lower than design incidence angles (Figure 80). The design-speed operating-line incidence angles were within the low-loss range of stator blade elements, as shown in Figure 81 by plots of loss-coefficient versus incidence-angle. Range (defined on Figure 63) was correlated as a function of inlet Mach number (Figure 82). The greatest range was obtained near the tip and least range at the hub. Range decreased with increasing Mach number for all blade elements. Similar trends in range were found in the original-stator data at low speeds, but stalls at high speed, due to the locally high loading at the stator hub, prevented defining the high-incidence sides of most blade-element-loss versus incidence-angle curves.

ACOUSTIC TEST RESULTS

Selected noise-data for the various rotor-stator configurations are compared in this section. Blade-passing-frequency noise is discussed for the slotted rotor with both the 64 and 50 vane stators. Broadband noise comparisons are shown for a slotted rotor with the 50 vane stator in the nominal and the 10 degrees closed positions. Supersonic fan-noise at high fan-speeds is presented for both the unslotted and slotted rotors. Sample spectra obtained from measurements with the dynamic pressure probe downstream of the stator are also presented.

Blade-Passing-Frequency Noise

A comparison of time-averaged blade-passing-frequency noise from the 64 and 50 vane stator cascades is presented in Figure 83. As previously discussed, interaction noise theory does not predict any significant difference in noise level radiated from the inlet of these two stator cascades. The data show similar trends existing for both stators as rotor blade tip relative Mach number is increased. The wide-open-throttle operating-line was selected as the basis for this comparison because of the closer matching in rotor overall pressure ratio between the two configurations than was true for part-throttle data points.

Two different types of fan-tip case treatment were tested, one consisting of open honeycomb cells and the other of skewed slots. The design and location of both these treatments were based on aerodynamic-performance considerations rather than acoustic considerations. Figure 84 presents the time-averaged levels of inlet blade-passing-frequency noise for both types of tip treatment with the fan operating along a part-throttle operating-line. The

part-throttle line comparison was chosen here because of the proximity of the part-throttle line to an actual engine operating line. Although large differences in aerodynamic performance were noted, up to seven points in fan efficiency, essentially no difference was seen in blade-passing-frequency noise.

Effects on blade-passing-frequency noise of changing the stator angle by 10 degrees is shown in Figure 85. The configuration tested was the slotted rotor with the redesigned stator (third fan-configuration) in the nominal and 10 degree closed position. Altering the stator angle showed only insignificant differences in inlet discrete-tone-noise.

Broadband Noise

Total broadband sound power level versus blade tip relative Mach number is shown in Figure 86 for the slotted rotor with the redesigned stator in its nominal and 10 degrees closed settings at part throttle. Typical one-third octave band sound pressure levels are shown in Figure 87. The fact that no major changes in noise levels can be seen in the plotted data suggests that the controlling source of broadband noise for this fan stage was not the stator. The broadband noise level remained fairly constant with increased blade tip relative Mach number for all the configurations tested in this program. However, other fans tested previously in other programs in this same facility had shown broadband noise levels increasing at about the fifth power of tip relative Mach number. The reason for this difference has not been determined. Although these other fans were designed for higher fan tip speeds, they operated off-design at speeds within the range of the 1000 ft/sec (3048 m/sec) fan tested under this program.

Supersonic Fan-Noise

Supersonic fan-noise existed only at 105 and 110 percent of design speed on this fan rig. Sound pressure level for this type of noise was calculated by summing the sound pressure levels of discrete frequency tones below blade-passing-frequency at integral multiples of shaft rotational speeds. Supersonic fan-noise is generated due to the presence of shock waves originating at the leading edge of each blade. Geometric differences between individual blades, well within manufacturing tolerances, affect this type of noise. Because supersonic fan-noise is associated only with the rotor and because this type of noise only propagates upstream, the changes made in the stator during this program had no effect on the supersonic fan-noise, as can be seen, for example, in Figure 68 of reference 5. The representative plot in Figure 88 (of this report) shows that there was a significant increase in noise level when supersonic fan-noise was present in the noise spectra. Points plotted below Mach number 1.1 are not tone levels but reflect broadband noise content below blade-passing-frequency; those above Mach 1.1 are predominantly influenced by discrete tones at harmonics of shaft speed. This trend is typical of all fans operating in the transonic Mach number range.

Downstream Spectra

Fan discharge blade-passing-frequency noise levels were sampled for a number of configurations by means of a 1/4-inch diameter dynamic pressure transducer which was traversable in the radial direction in a plane approximately one-inch downstream of the stator trailing edge.

Spectral plots (50-Hz bandwidth) show that the ratio of blade-passing-frequency level to background level was sufficient to allow sound pressure level of the tones to be obtained at speeds below 100 percent design speed. Figure 89 shows data from the first fan-configuration, which also is typical of the data from the other configurations [ref. 4 and 5].

The time-averaged blade-passing-frequency noise level for the first fan-configuration is presented in Figure 90. Noise level is plotted as function of blade tip relative Mach number along the part-throttle operating line. Directly comparable measurements were not obtained for the other fan configurations; however, measurements were obtained for the third fan-configuration (slotted rotor and redesigned stator) with the stator closed 10 degrees. Figure 90 shows that trends of blade-passing-frequency noise versus rotor Mach number were similar for these two tests.

Fan generated broadband noise measured with the downstream microphone was not evaluated because of the level of wind noise in the high velocity airstream. Supersonic fan-noise propagates only from the inlet, and the telltale discrete tones at multiples of shaft speed are absent from the 105 percent design speed spectra of Figure 89.

SUMMARY OF RESULTS

The aerodynamic performance and noise levels of three low-tip-speed, low-noise fan-configurations were determined: 1) unslotted rotor and unslotted stator, 2) slotted rotor and slotted stator, and 3) slotted rotor and redesigned stator (unslotted). The significant results obtained from the testing of these three fan-configurations are summarized below.

1. The third fan-configuration at design speed and a 15 percent stall margin demonstrated a stage and rotor adiabatic efficiency of 0.883 and 0.936, respectively, which exceeded design efficiency goals. Measured total-pressure and loss-coefficients for the rotor and stator were lower than design estimates at the midspan but were higher near endwalls; spanwise averages were reasonably close to design.

2. Stalls occurred when blade loading limits were encountered. Rotor tip loading determined stall at low speed, and stator hub loading determined stall at high speed (above 80 percent of design speed). Strain-gages were employed in determining which blade row initiated stall. The redesigned stator, which had a lower loading than the original stator, provided the fan stage with an additional seven percent in stall margin. The lower loadings were obtained by increasing the axial velocity at the stator exit.

3. Stable rotor-operation was obtained over a wide range of operation despite the large past-axial relative flow-angle at the hub.

4. Flow was 97.5 percent of design flow at near design pressure ratios and efficiencies because channels between rotor blades had insufficient area and because rotor tip deviation angles exceeded the design estimates. The rotor limited the maximum flow capacity except when the stator vanes were reset closed relative to their design chord angle.

5. Slotting increased part-speed efficiency but reduced flow capacity at high speeds. Slots did not increase blade loading limits.

6. Boundary layer suction through slits at intersections of stator suction surfaces and the hub wall reduced losses inboard of 30 percent of span. Suction also raised the stator loading limit.

7. Radial distributions of pressure and temperature ratios agreed with design estimates near stall. At a throttle setting that gave adequate stall margin, midspan and tip work levels were lower than design levels.

8. Tip-radial, hub-radial, and circumferential distortions substantially influenced fan performance. Tip-radial distortion reduced stall margin, particularly at part-speed where rotor loading determined stall. The circumferential distortion had little effect on stall margin, and hub-radial distortion raised stall margin. Axial,

radially skewed slots in the casing over the rotor tip raised stall margin with all three types of distortion. A honeycomb casing over the rotor tip also improved stall margin with distorted inlet flows, but the efficiency penalties were unacceptable.

9. All configurations tested showed that blade-passing frequency noise levels increased with increased blade tip relative Mach number. Reducing the number of vanes from 64 to 50, the addition of slots to the blades, or the blade tip casing treatment of open honeycomb cells or skewed slots had no substantial effect on inlet noise.

10. Broadband noise was relatively constant over the range of speeds and flows tested. This lack of variation with speed had not been noted previously for a wide range of fan designs tested in this and other facilities.

11. No supersonic fan-noise was measured below 105 percent of design speed. This type of fan noise was not affected significantly by blade slots, stator design, or stator setting angle.

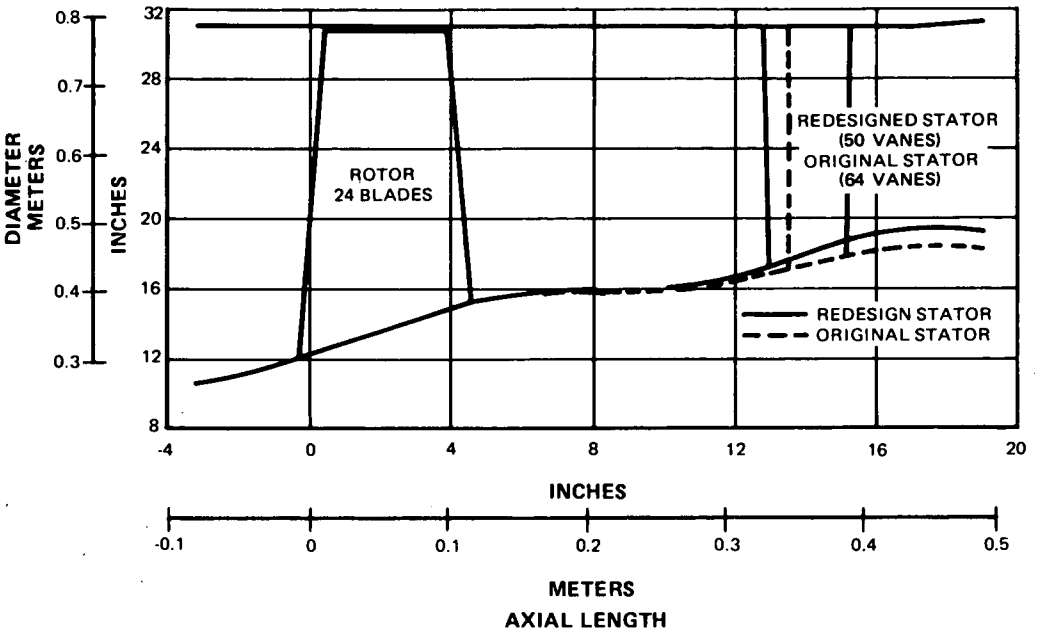

Figure 1 Fan Flowpath

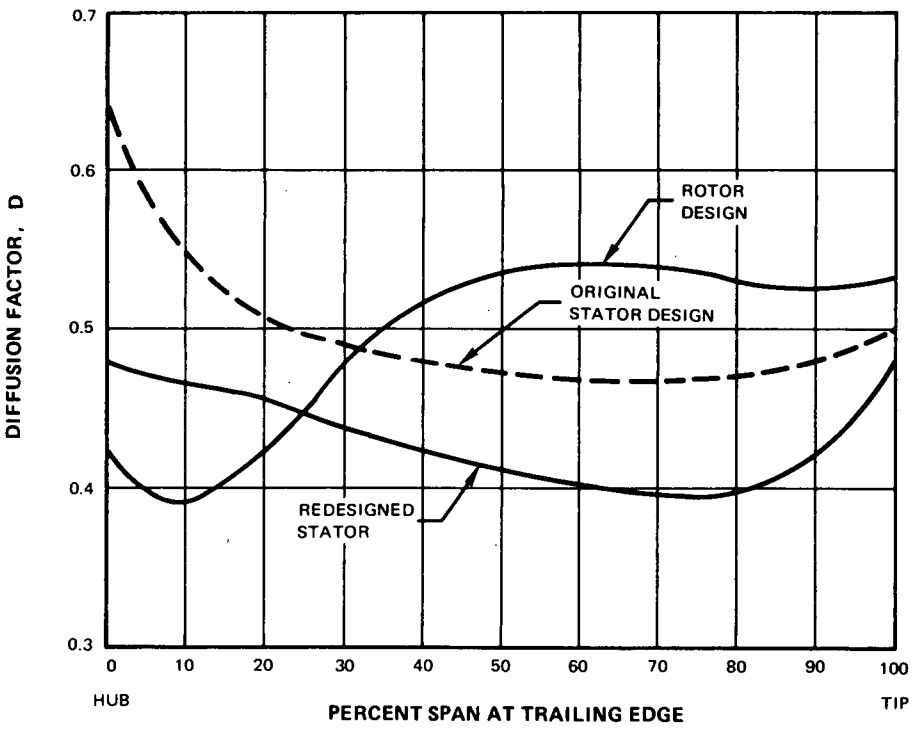

Figure 2 Rotor and Stator Design Diffusion Factors vs Span

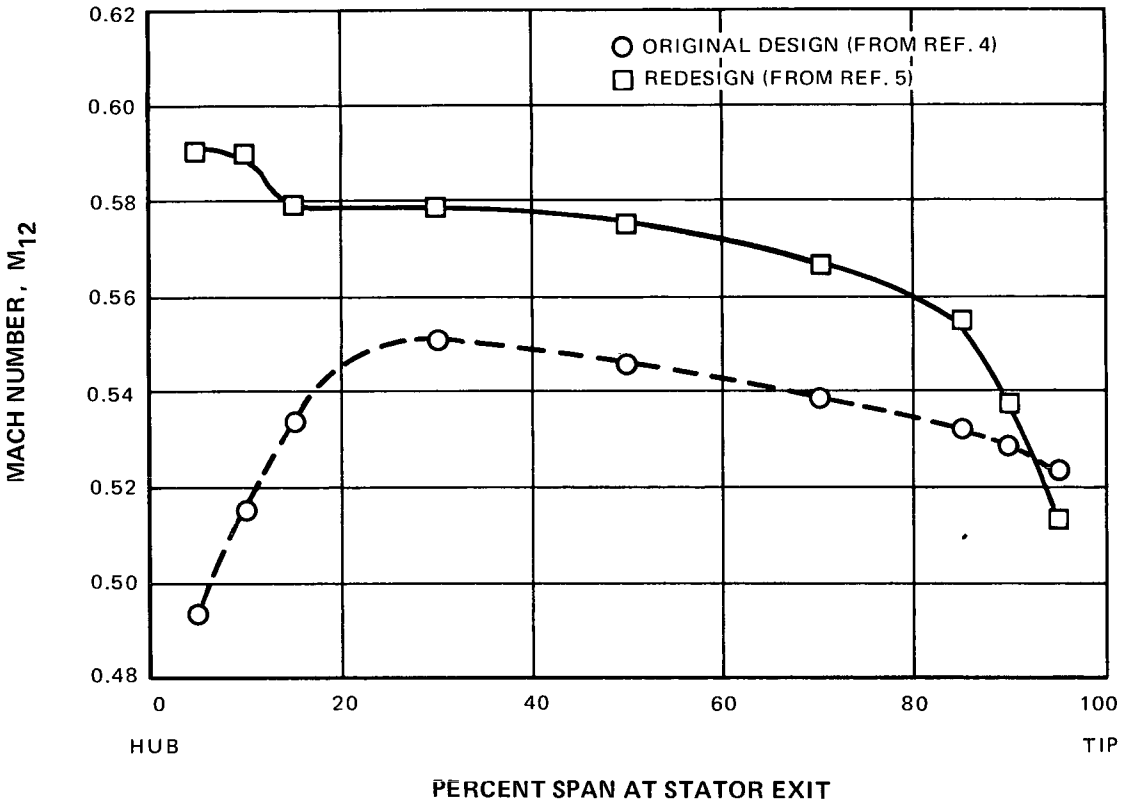

Figure 3 Stator Design Exit Mach Number vs Span

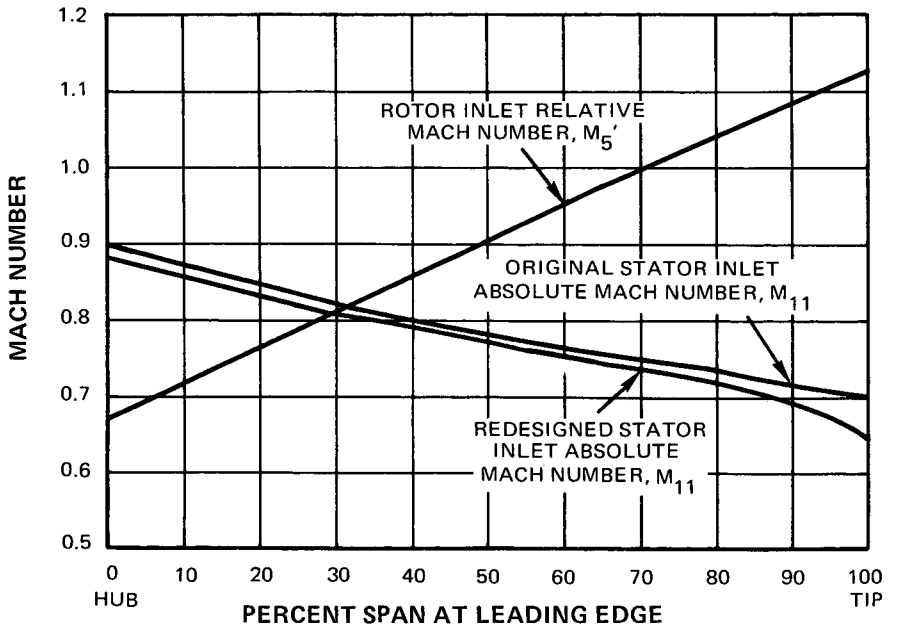

Figure 4 Rotor and Stator Design Inlet Mach Number vs Span

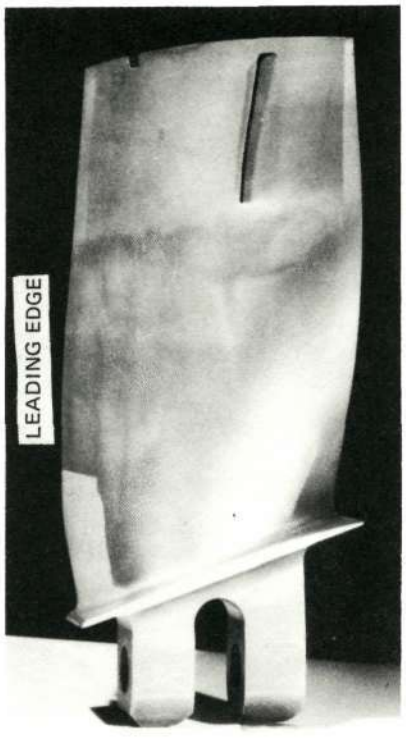

Slotted Rotor Blade

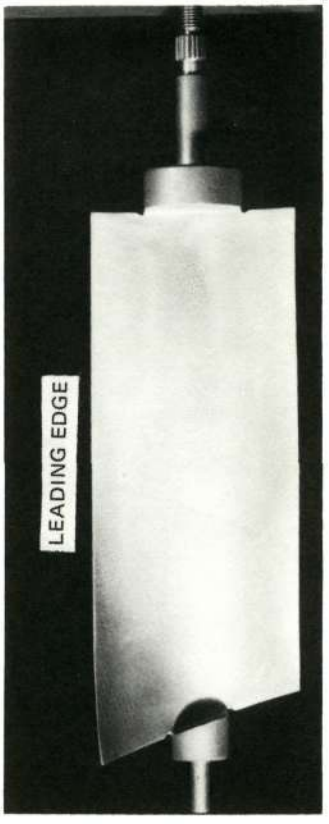

Redesigned Stator Vane (Unslotted)

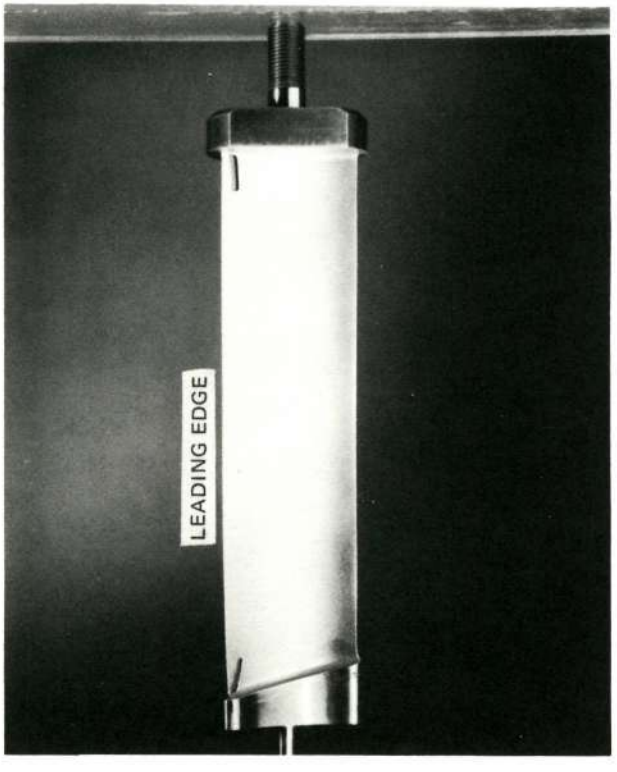

Original Stator Vane (Slotted)

Figure 5 Rotor and Stator Blades

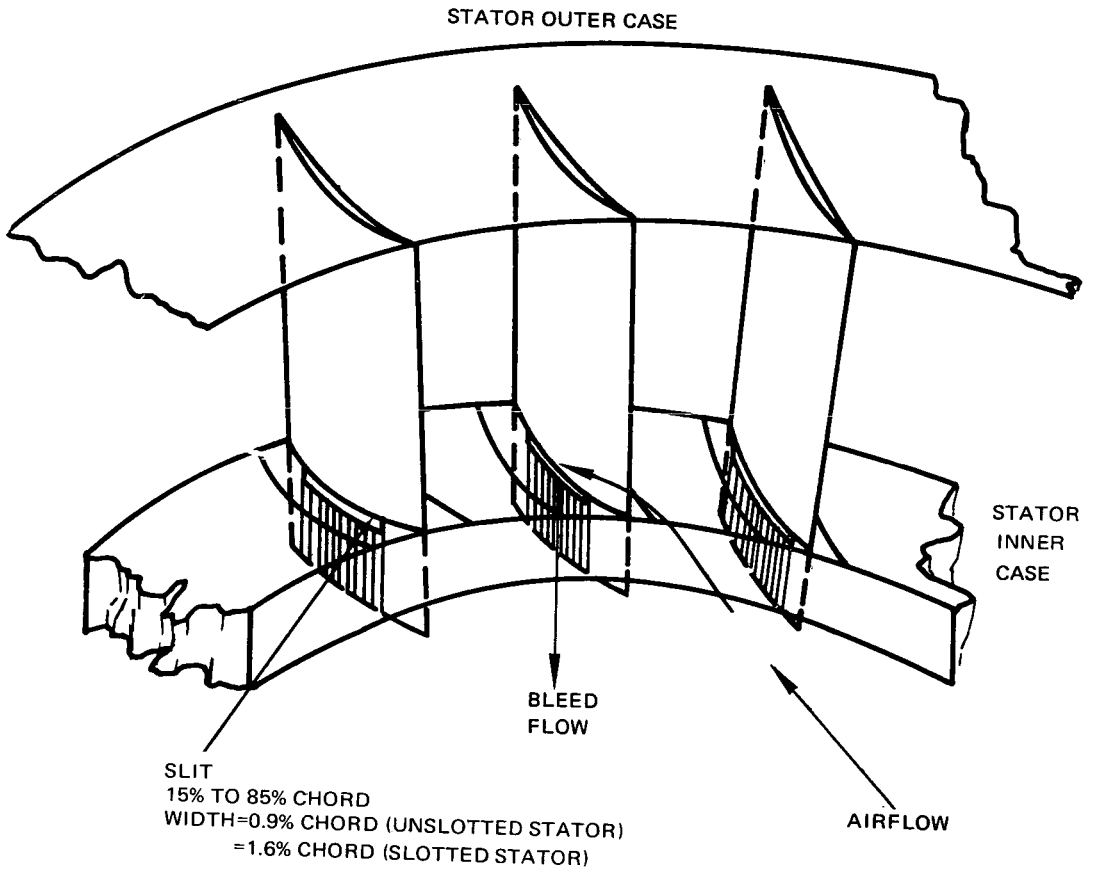

Figure 6 Schematic of Stator Hub Slit for Corner-Boundary-Layer Suction

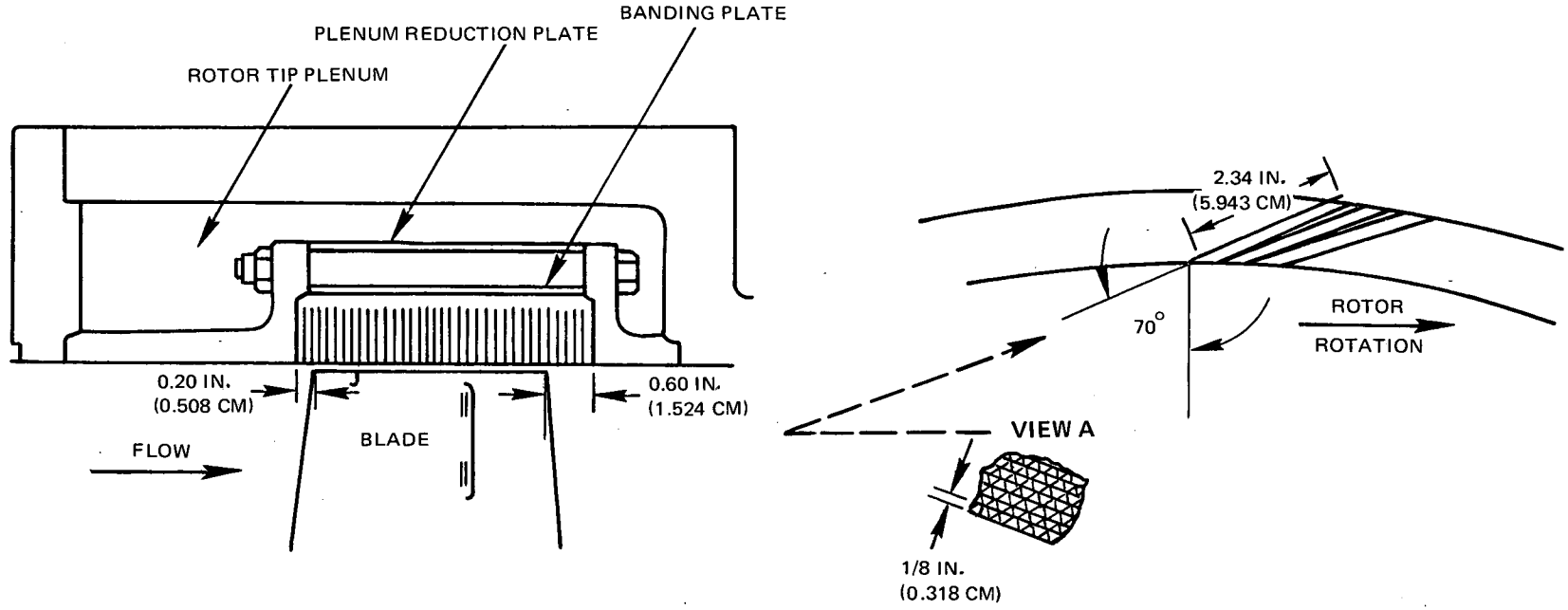

Figure 7 Honeycomb-Case Rotor Tip Treatment

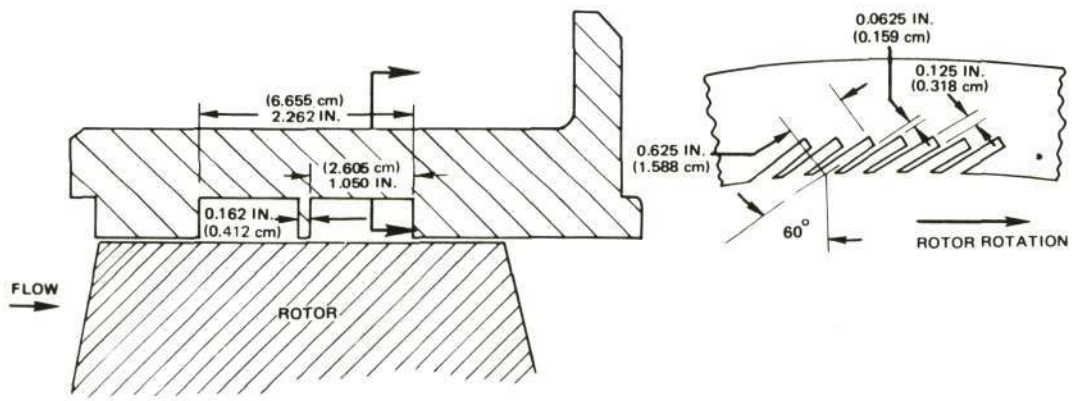

Figure 8 Skewed-Slot-Casing Rotor Tip Treatment

Figure 9 Vortex Generators in Outer Case Wall Shown With Honeycomb Over Rotor Tip

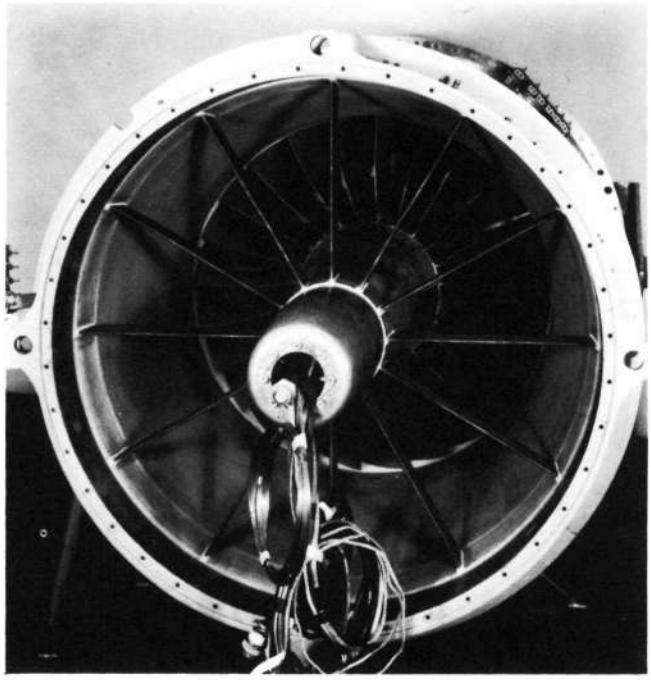

Figure 10 Inlet Configuration for Performance Testing

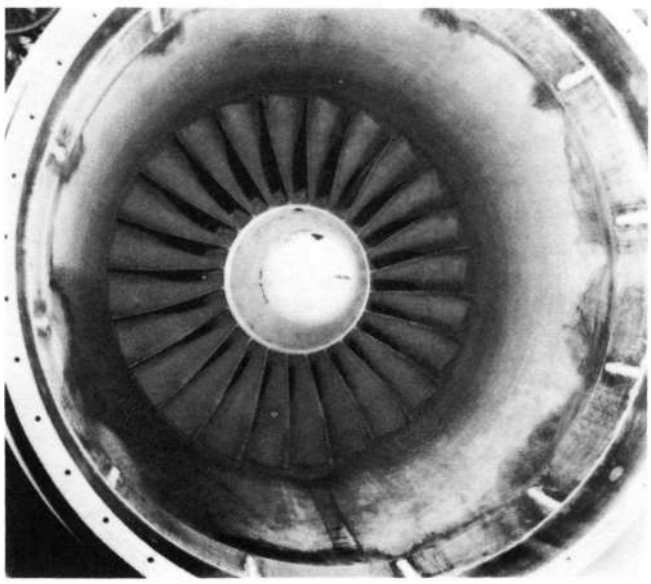

Figure 11 Inlet Configuration for Noise Testing

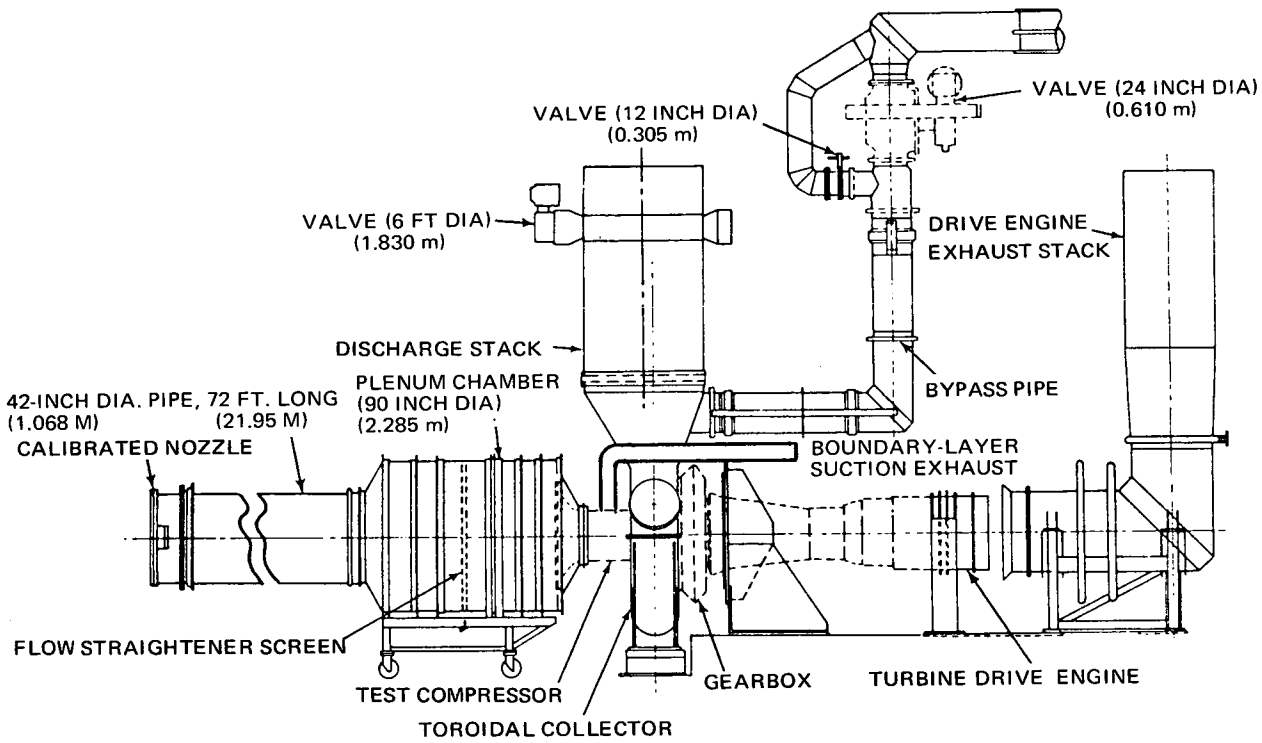

Figure 12 Schematic of Compressor Test Facility

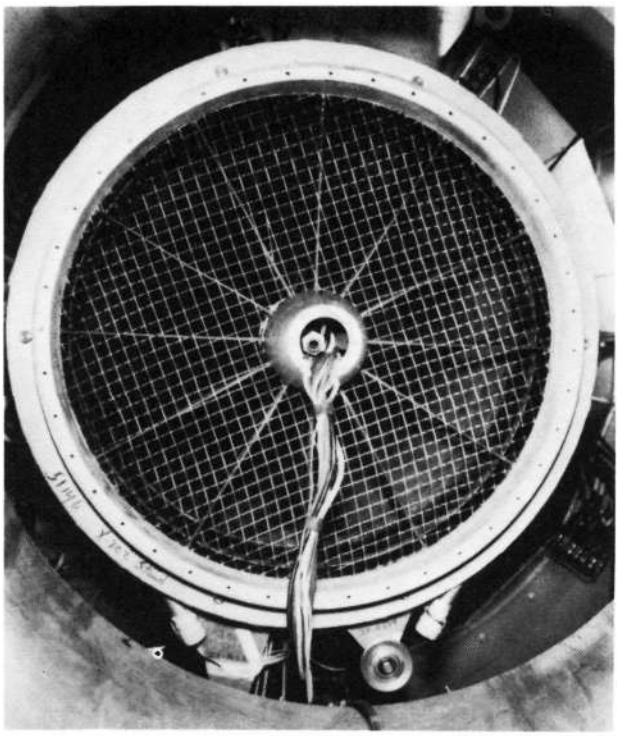

TEST COMPRESSOR WITH DISTORTION SUPPORT SCREEN INSTALLED

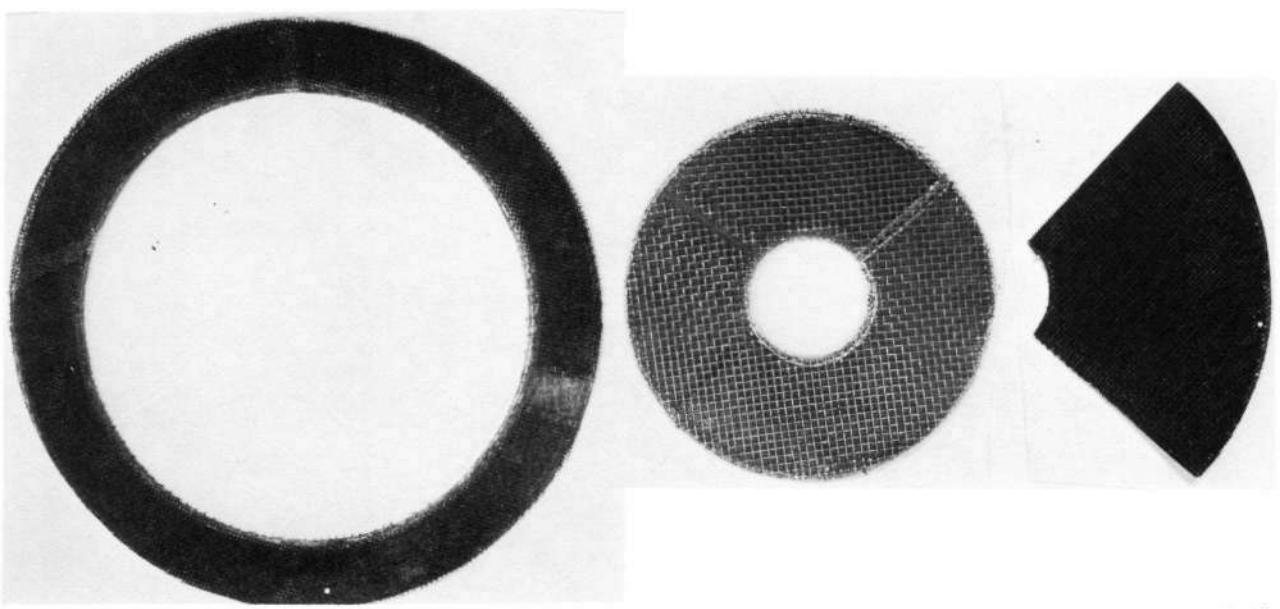

TIP RADIAL HUB RADIAL CIRCUMFERENTIAL

DISTORTION SCREENS

Figure 13 Support Screen and Inlet Distortion Screens

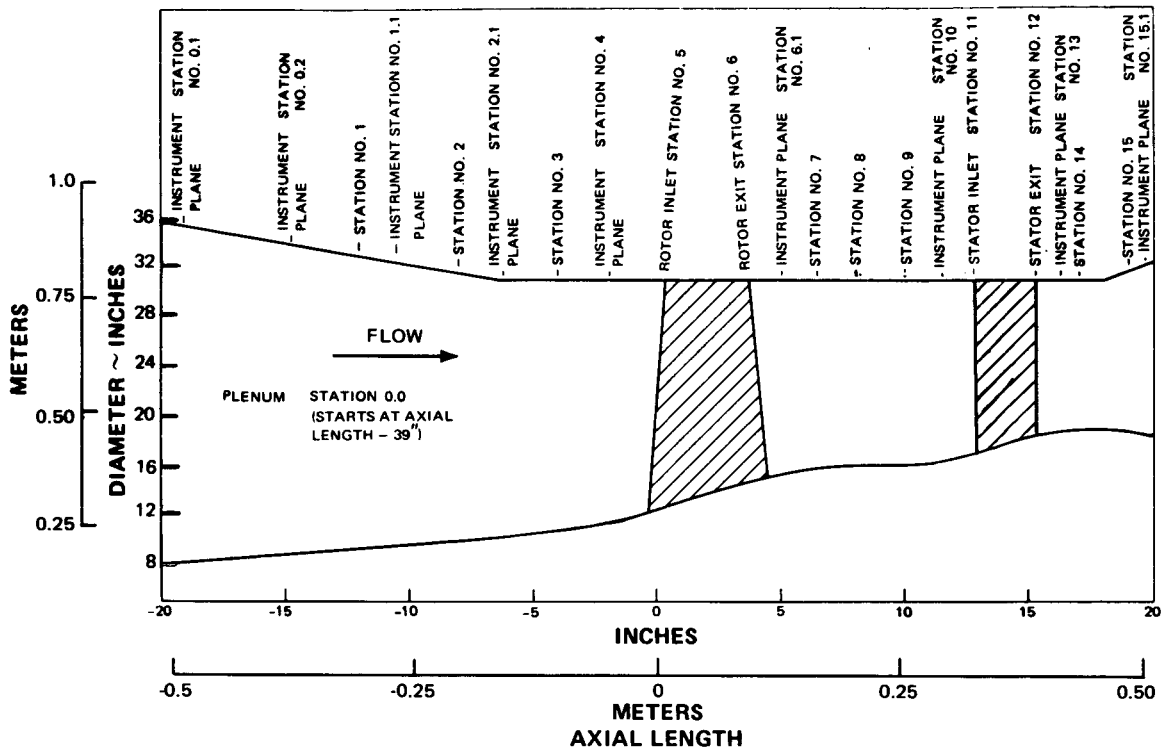

AXIAL LOCATION OF FLOWPATH INSTRUMENTATION

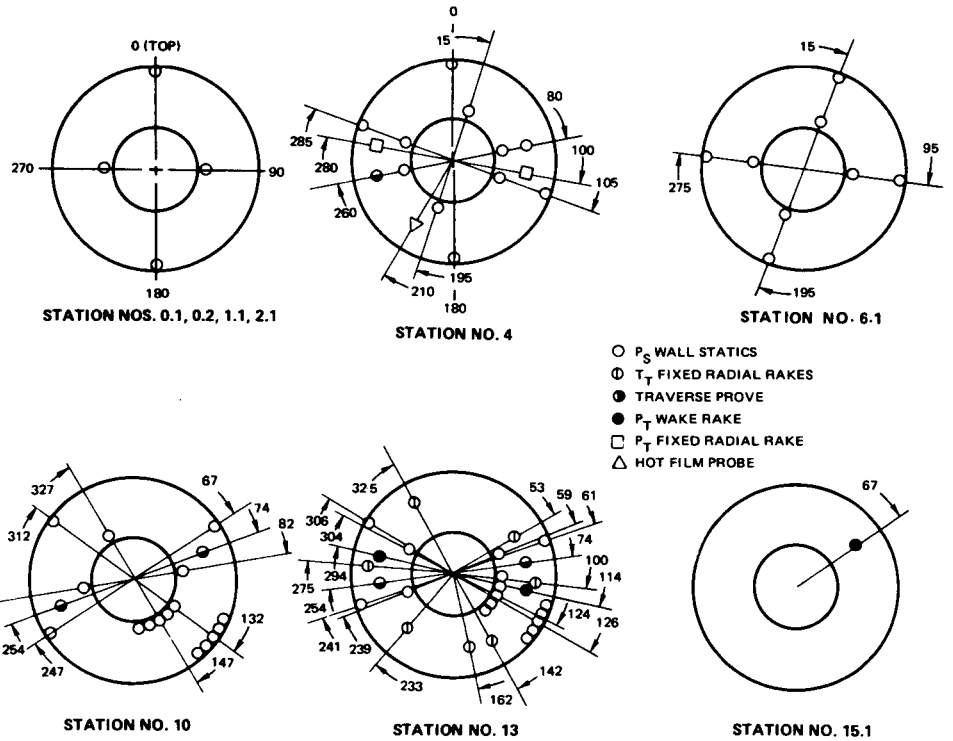

CIRCUMFERENTIAL LOCATIONS OF INSTRUMENTATION, LOOKING DOWNSTREAM, ROTOR ROTATION IS COUNTERCLOCKWISE.

Figure 14 Location of Flowpath Instrumentation

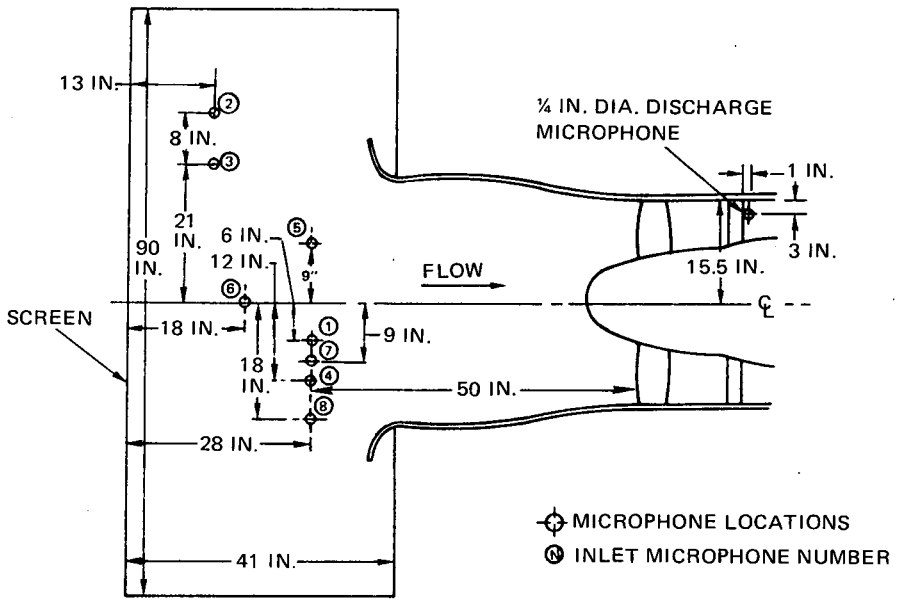

Figure 15 Acoustic Microphone Locations for Fan Noise Tests

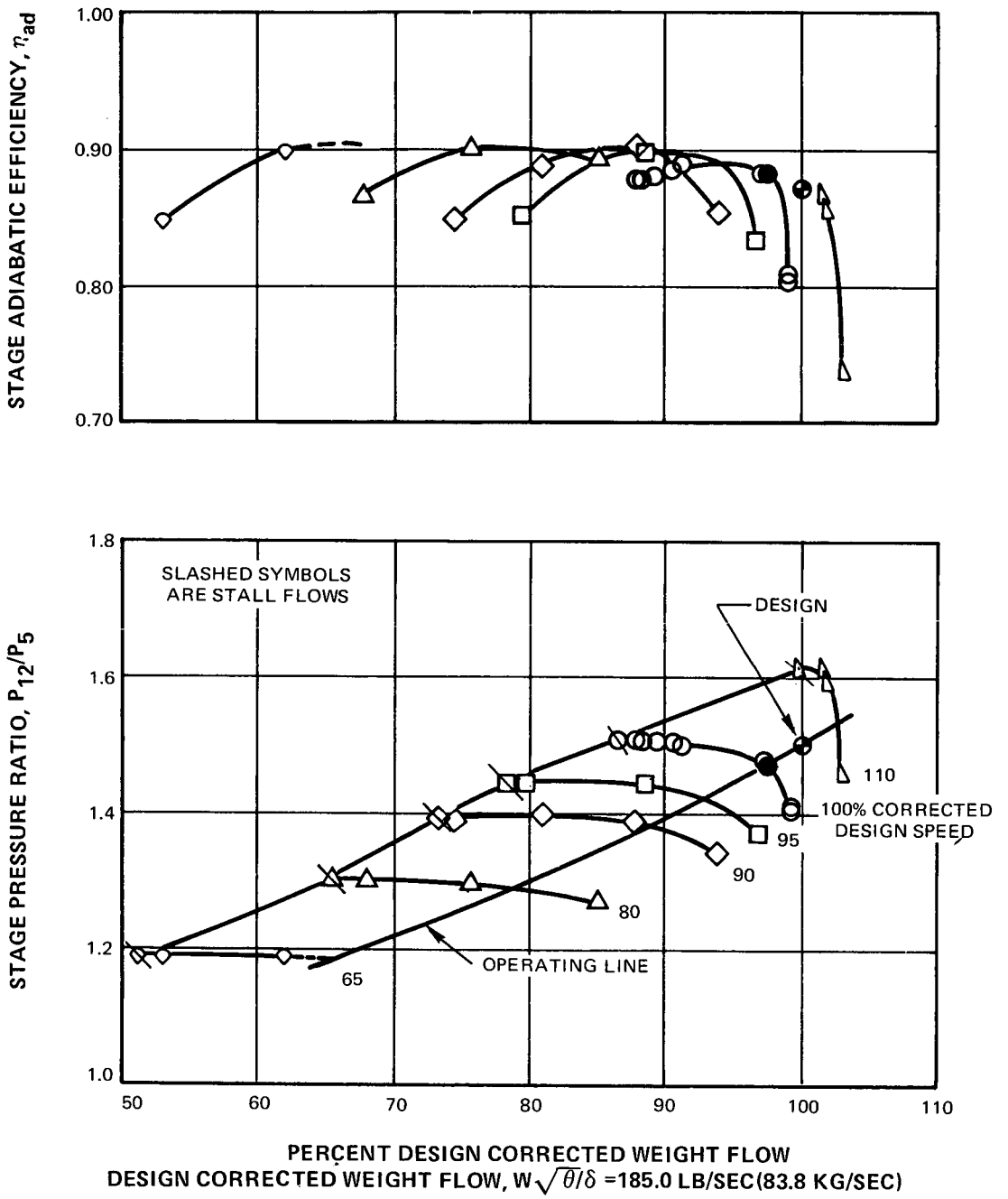

Figure 16 Overall Fan Performance With Uniform Inlet Flow, Slotted Rotor and Redesigned Stator

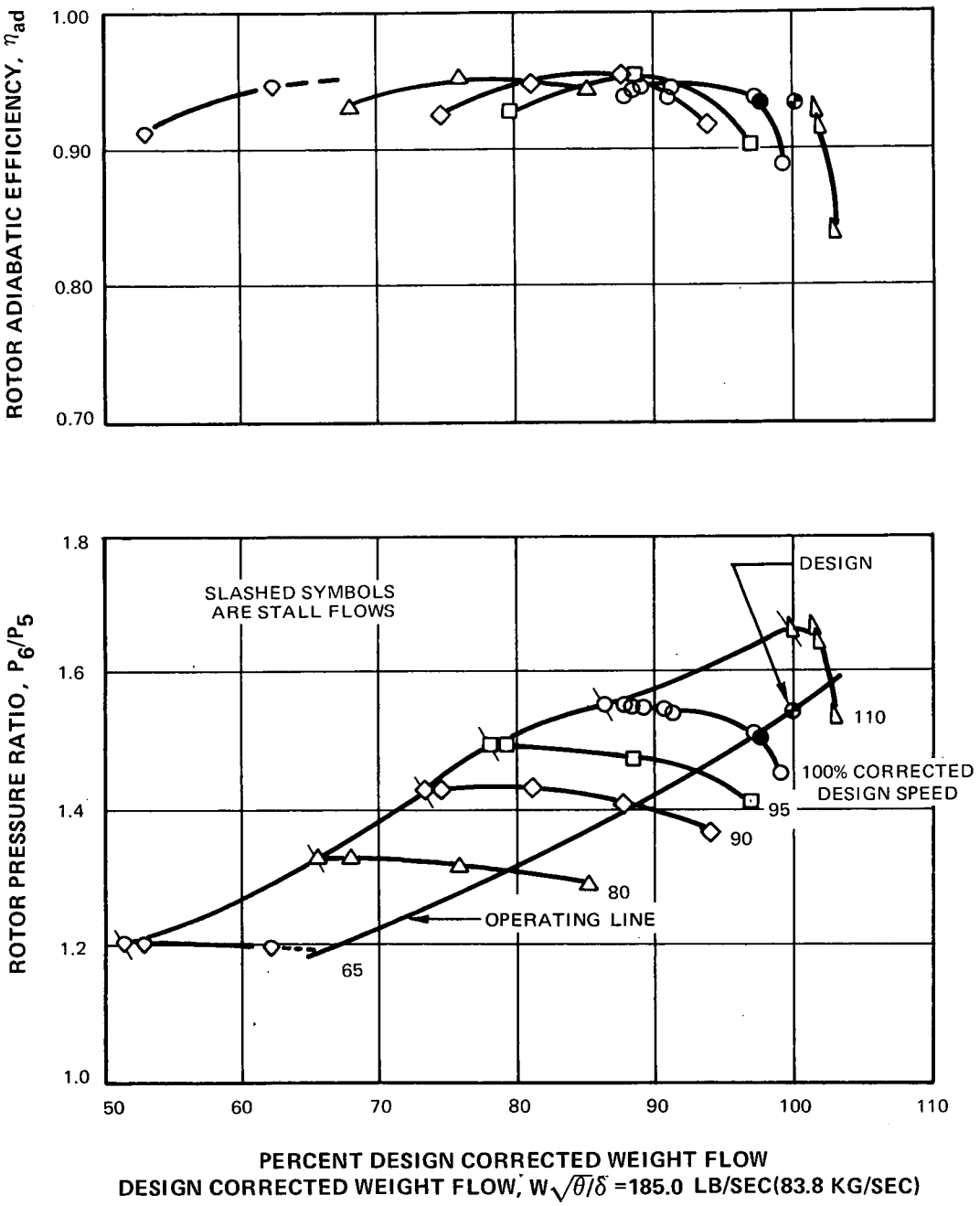

Figure 17 Overall Performance of Slotted Rotor With Uniform Inlet Flow

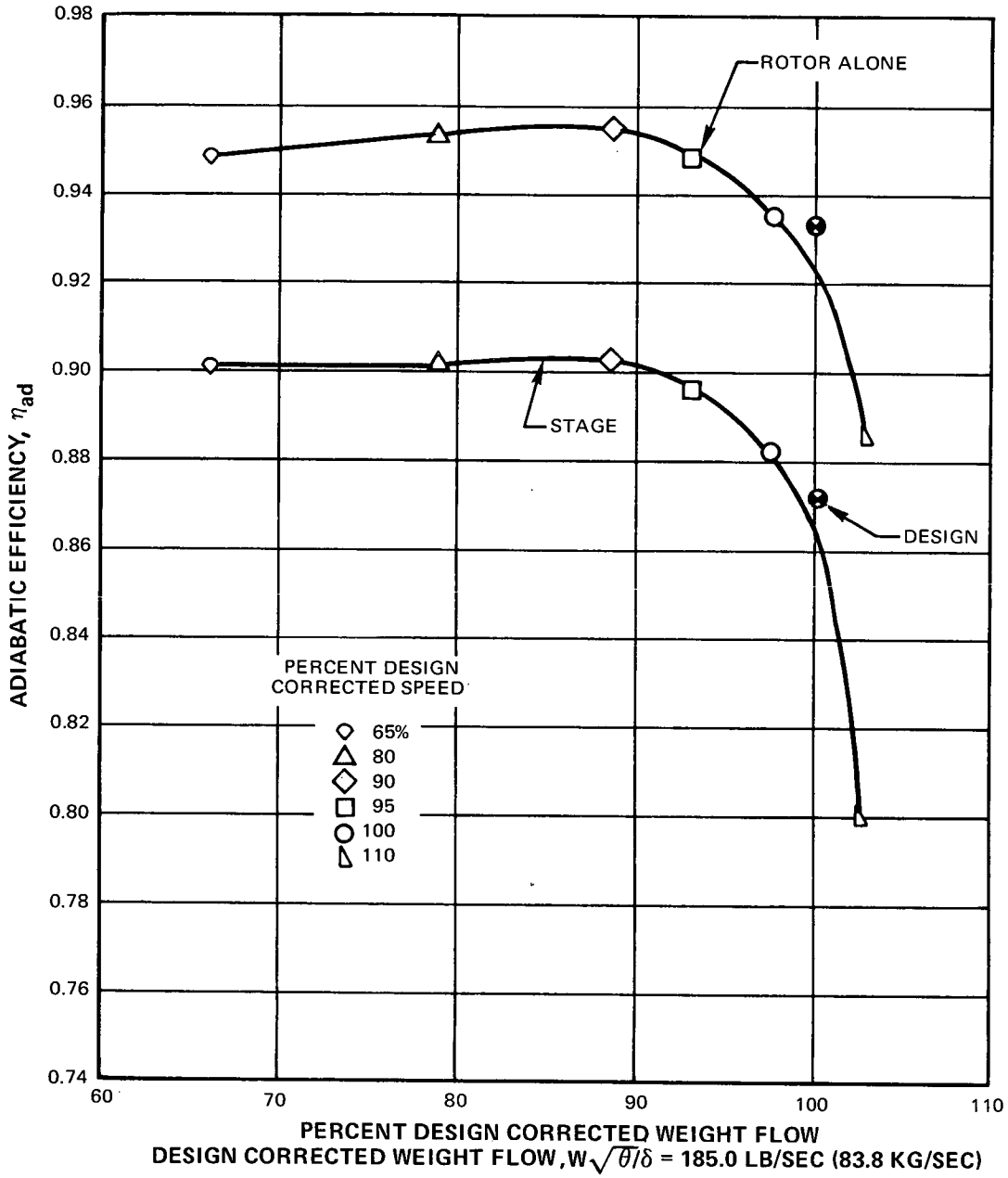

Figure 18 Efficiency vs Flow on Constant-Throttle Operating Line Having 15% Stall Margin at Design Speed

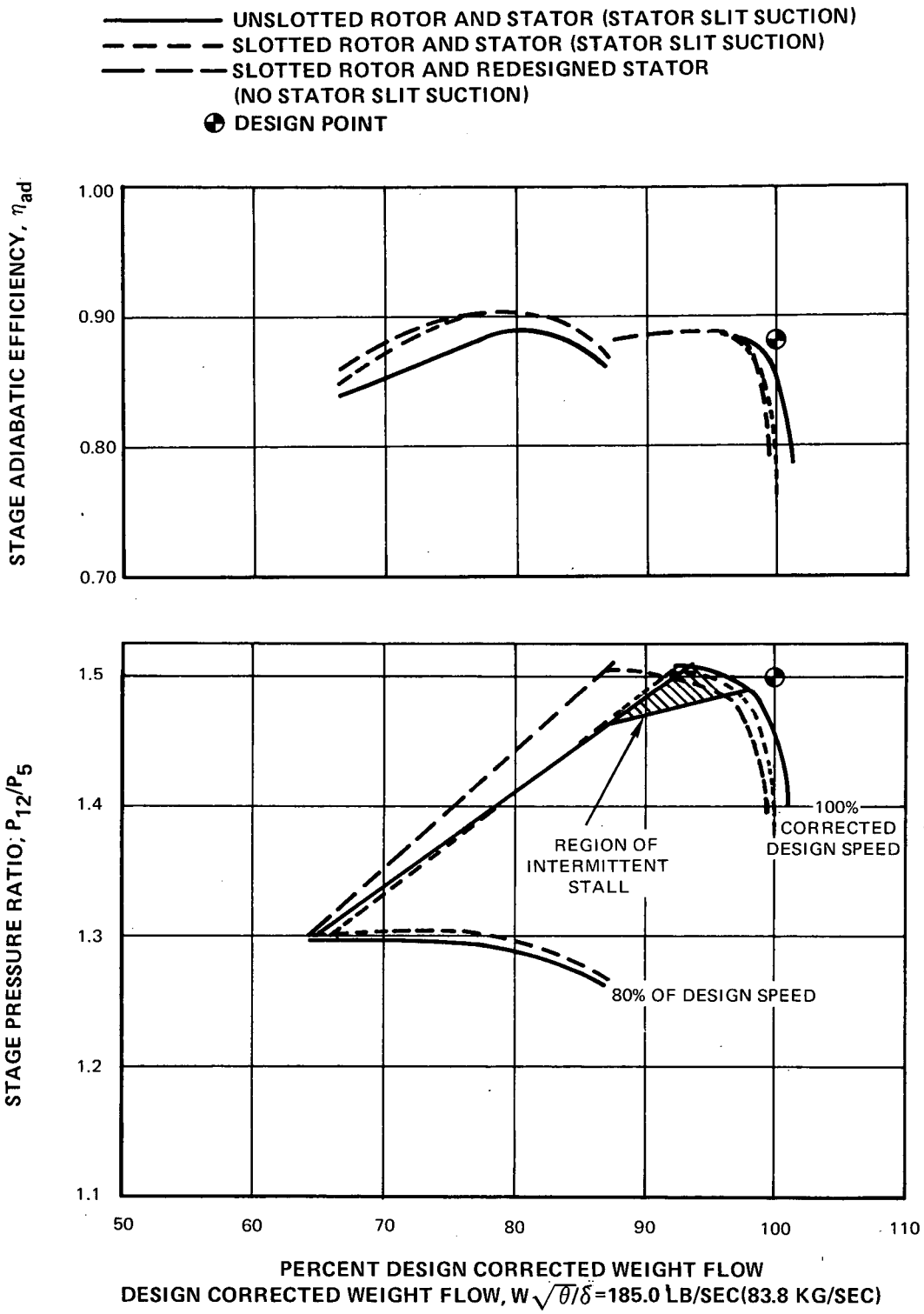

Figure 19 Fan Overall Performance Maps for Unslotted Rotor and Stator, Slotted Rotor and Stator, and Slotted Rotor and Redesigned Stator

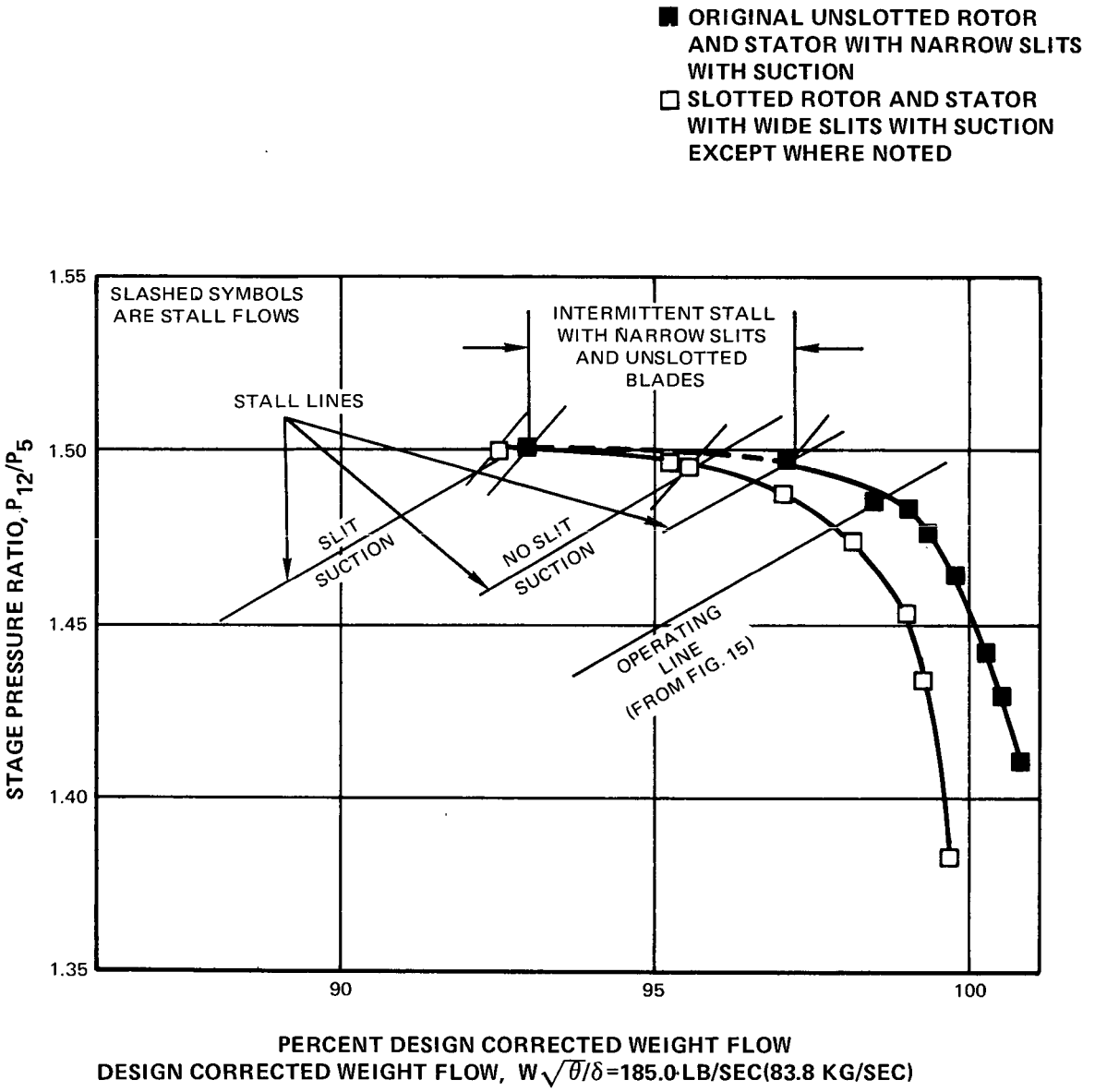

Figure 20 Effect of Airfoil Slots and Stator Hub Slit Suction on Stall Line at Design Speed

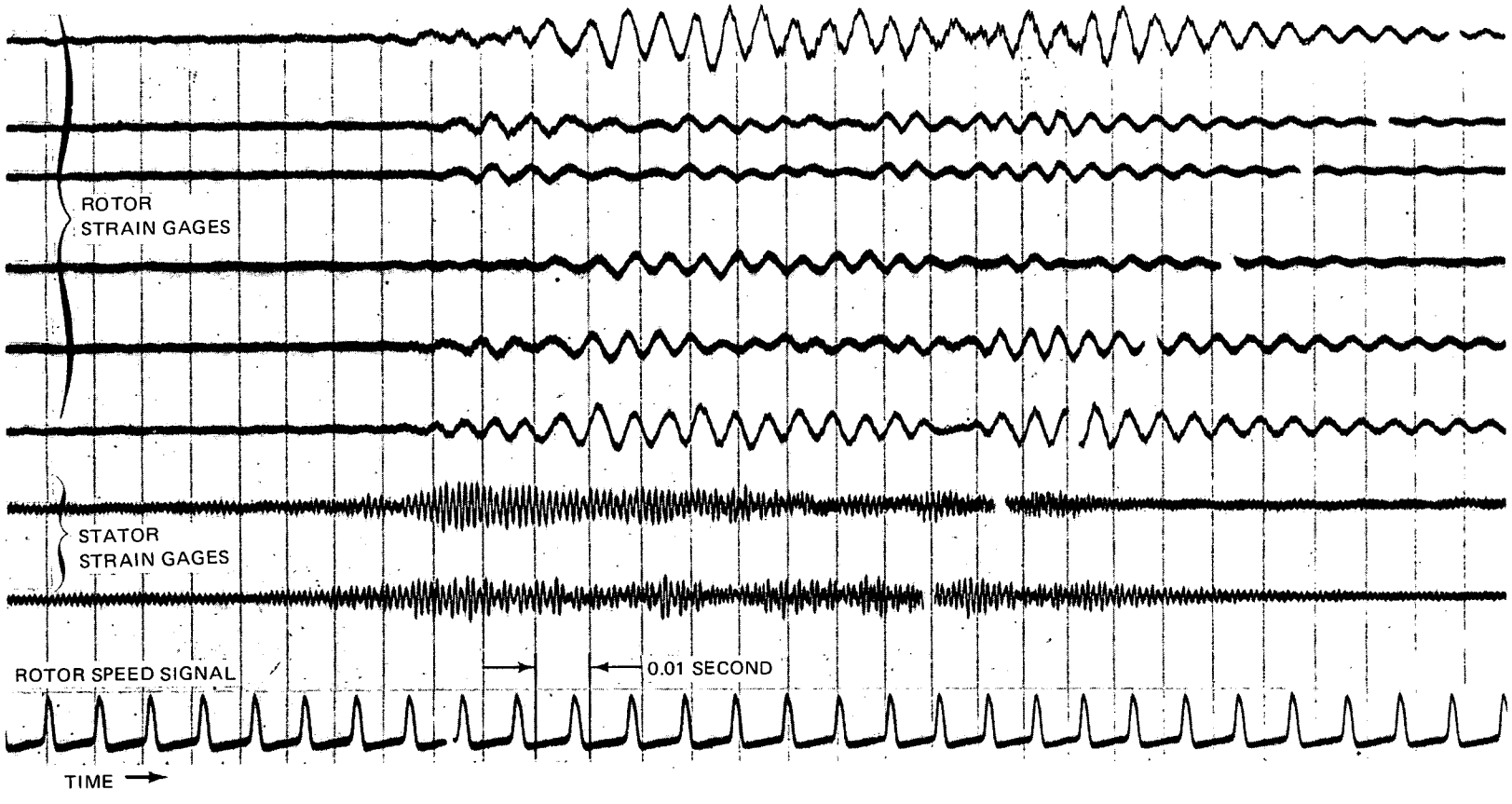

Figure 21 Oscillograph Trace of Stator Initiated Stall at 80% Design Speed With Uniform Inlet Flow, Slotted Rotor and Stator Without Stator Hub Slit Suction

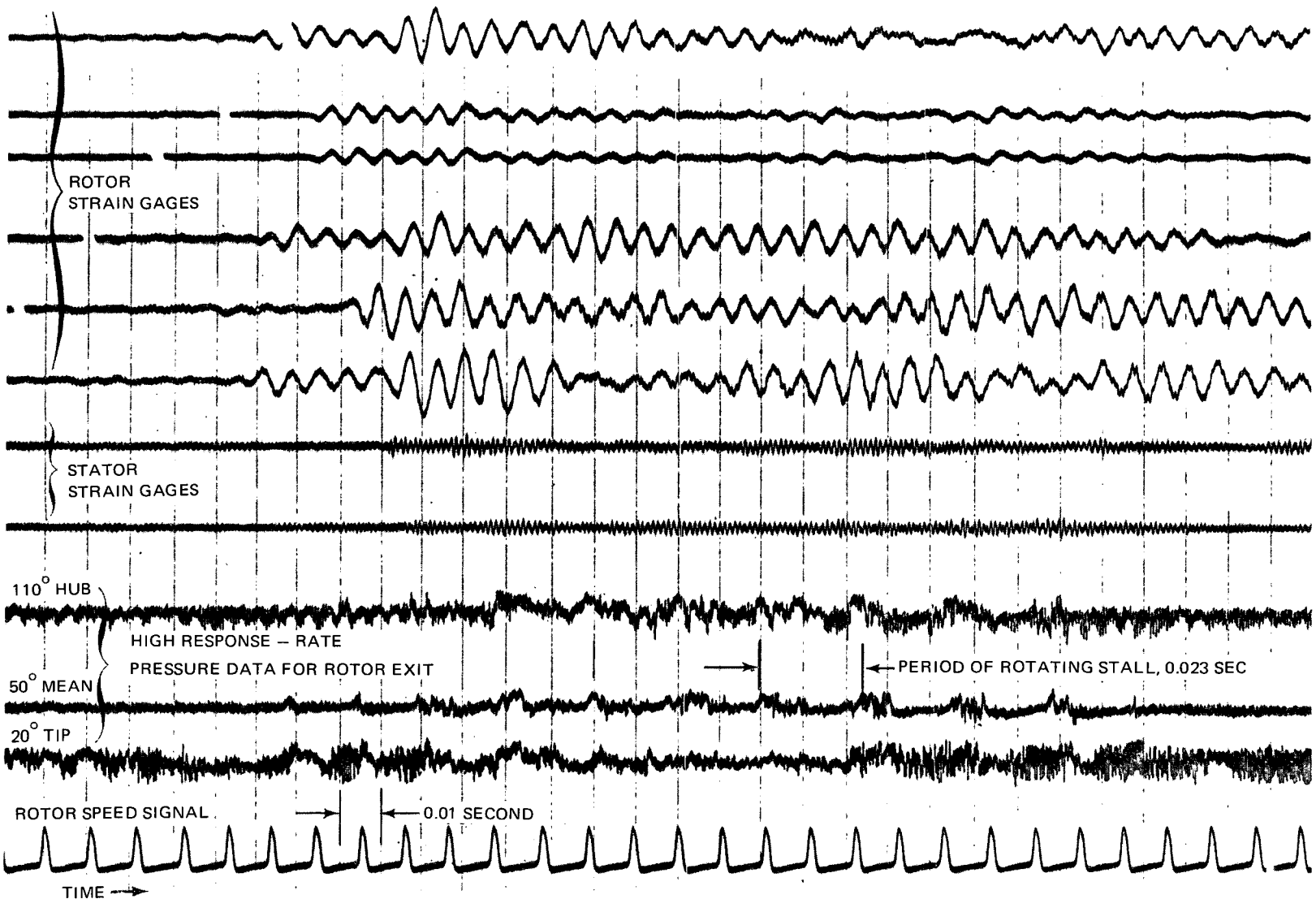

Figure 22 Oscillograph Trace of Rotor Initiated Stall at 80% of Design Speed, Uniform Inlet Flow, Slotted Rotor and Stator With Hub Slit Suction

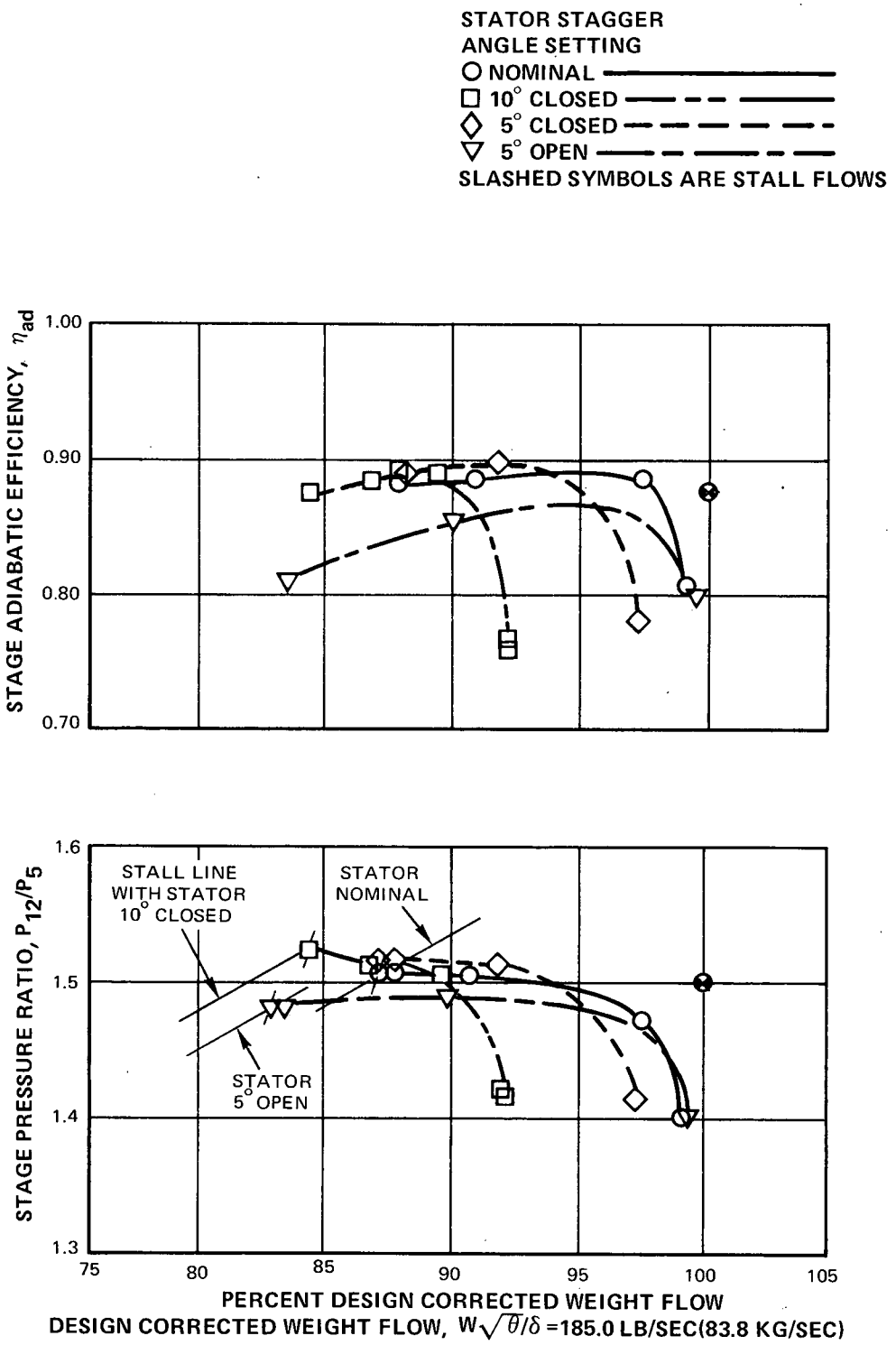

Figure 23 Performance at Design Speed With Stator at Nominal and Reset Stagger Angles

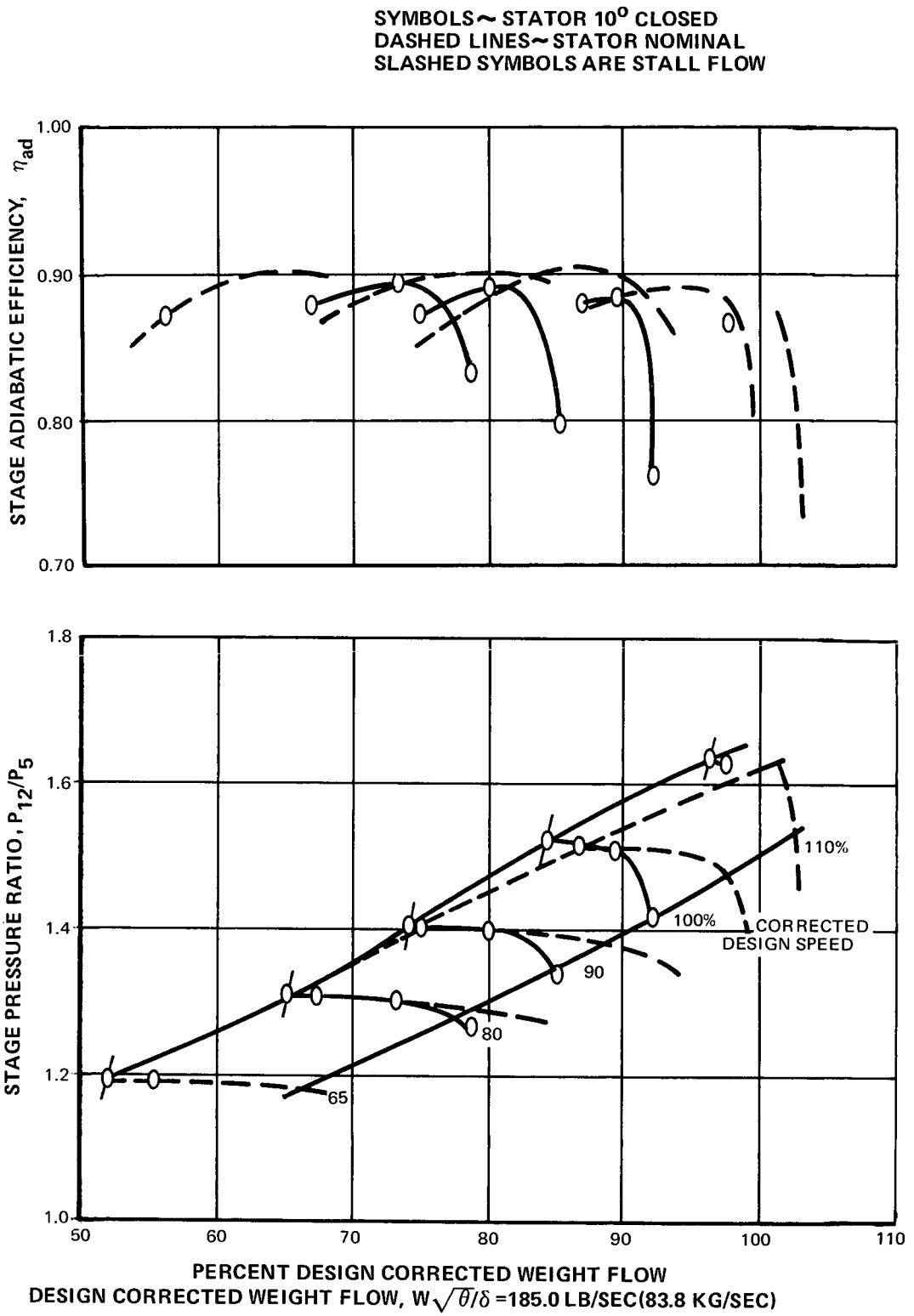

Figure 24 Fan Performance With Nominal and 10° Closed Stator Settings

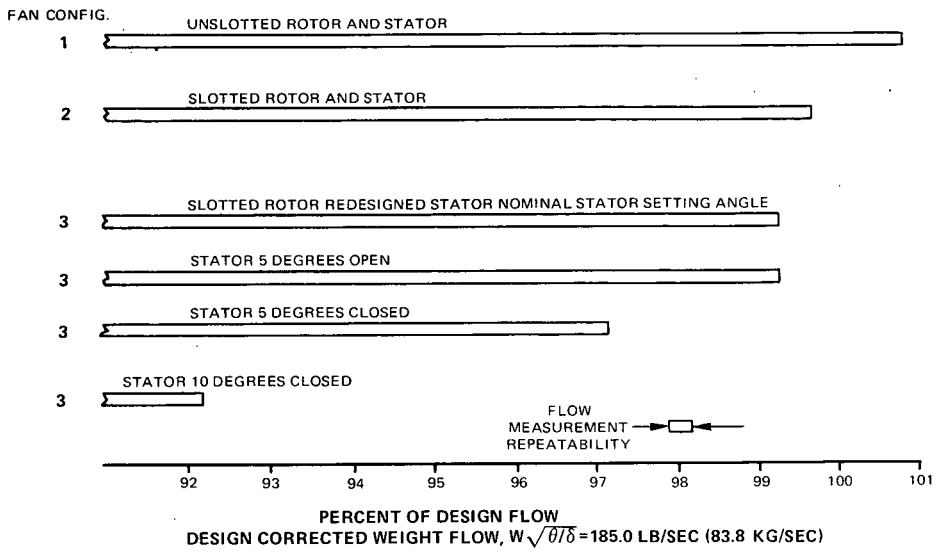

Figure 25 Maximum Weight Flow at Design Speed for Different Fan Configurations

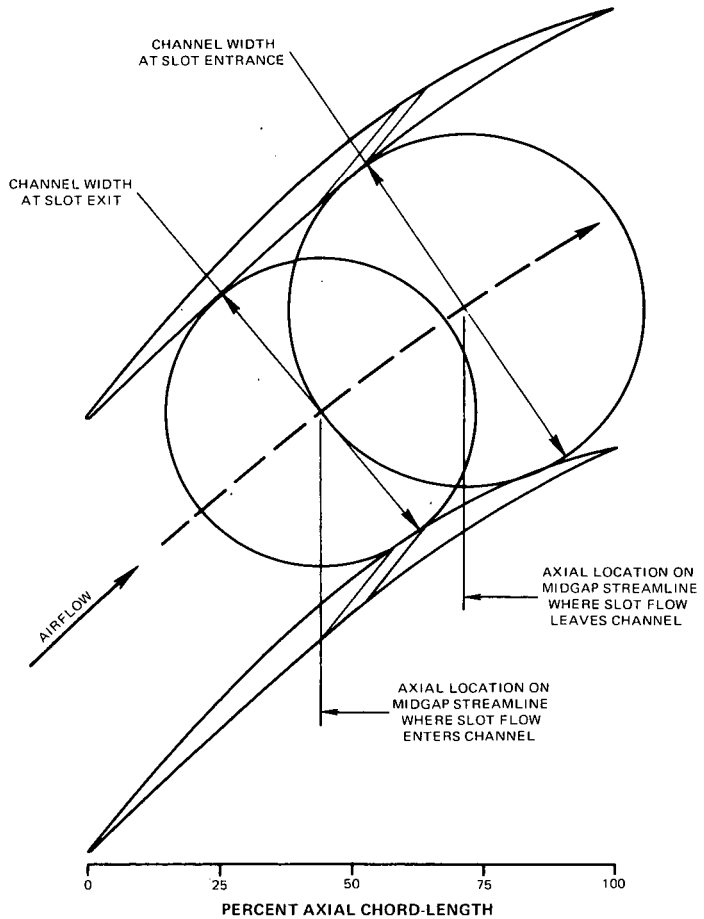

Figure 26 Location of Rotor Airfoil Slot Entrance and Exit Relative to Channel Between Blades at 73% Span From Hub

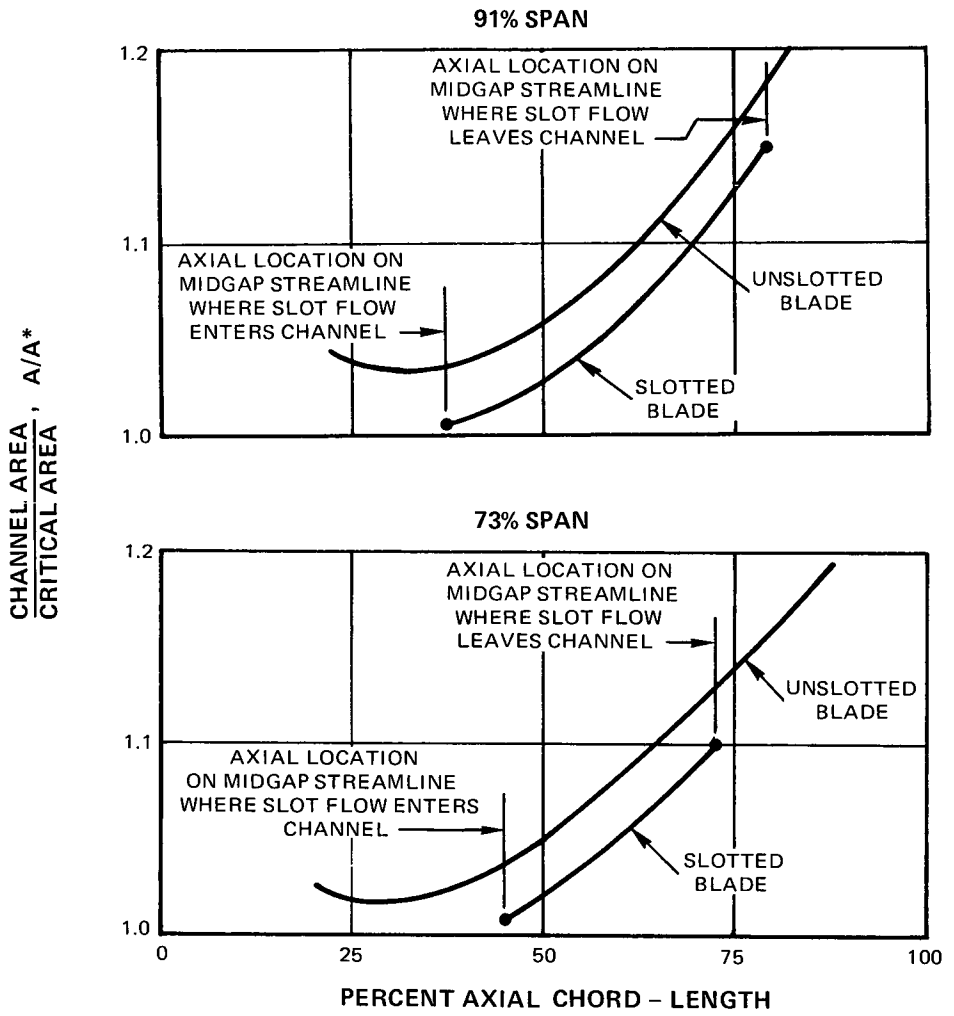

Figure 27 Rotor Critical-Area Ratios vs Axial Location at 73 and 91% of Span Showing Effect of Slot

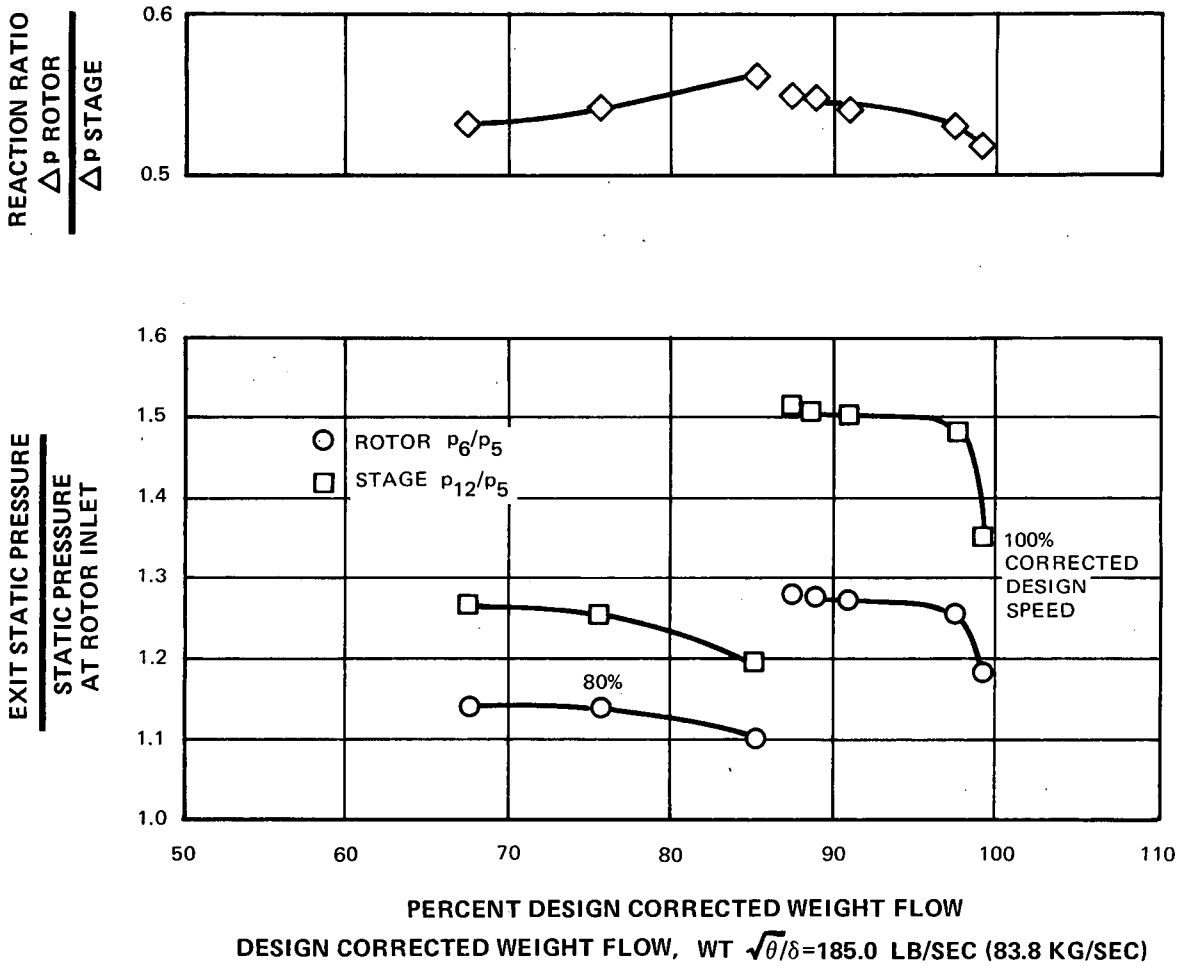

Figure 28 Static Pressure Ratio for Rotor and Stage, and Reaction Ratio vs Percent Design Corrected Flow

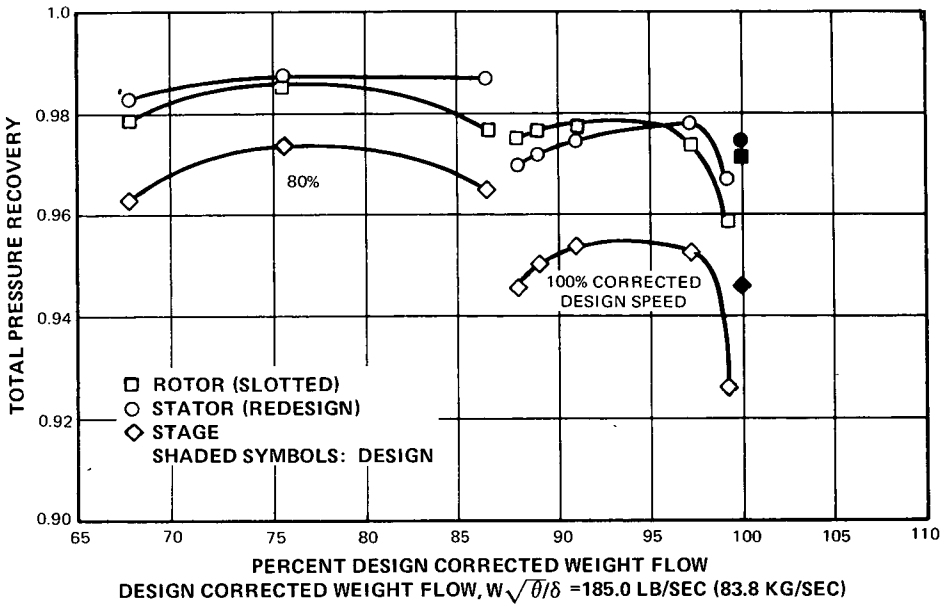

Figure 29 Total Pressure Recovery for Rotor, Stator, and Stage vs Percent Design Corrected Weight Flow

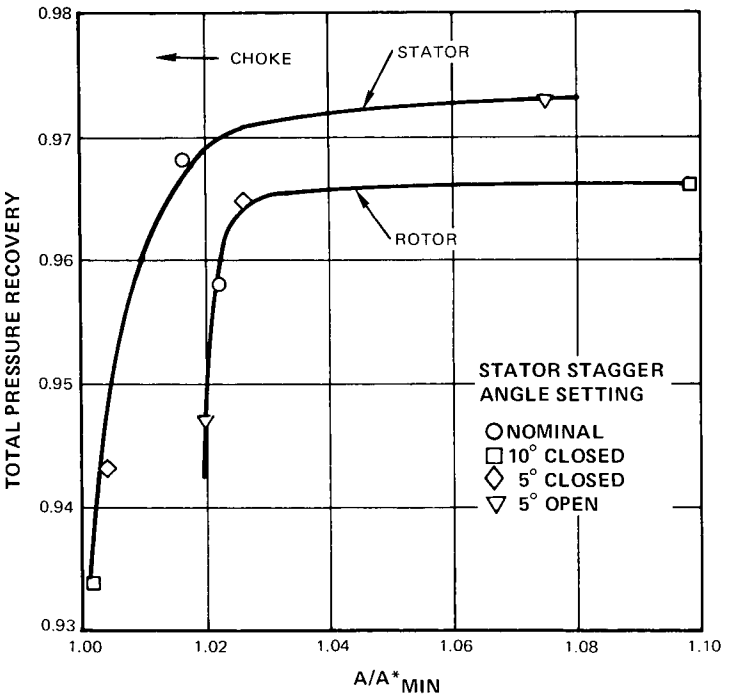

Figure 30 Total-Pressure Recovery of Slotted Rotor and of Redesigned Stator vs A/A* Minimum for Open-Throttle-Design-Speed Data Points With Different Stator Stagger Angle Settings

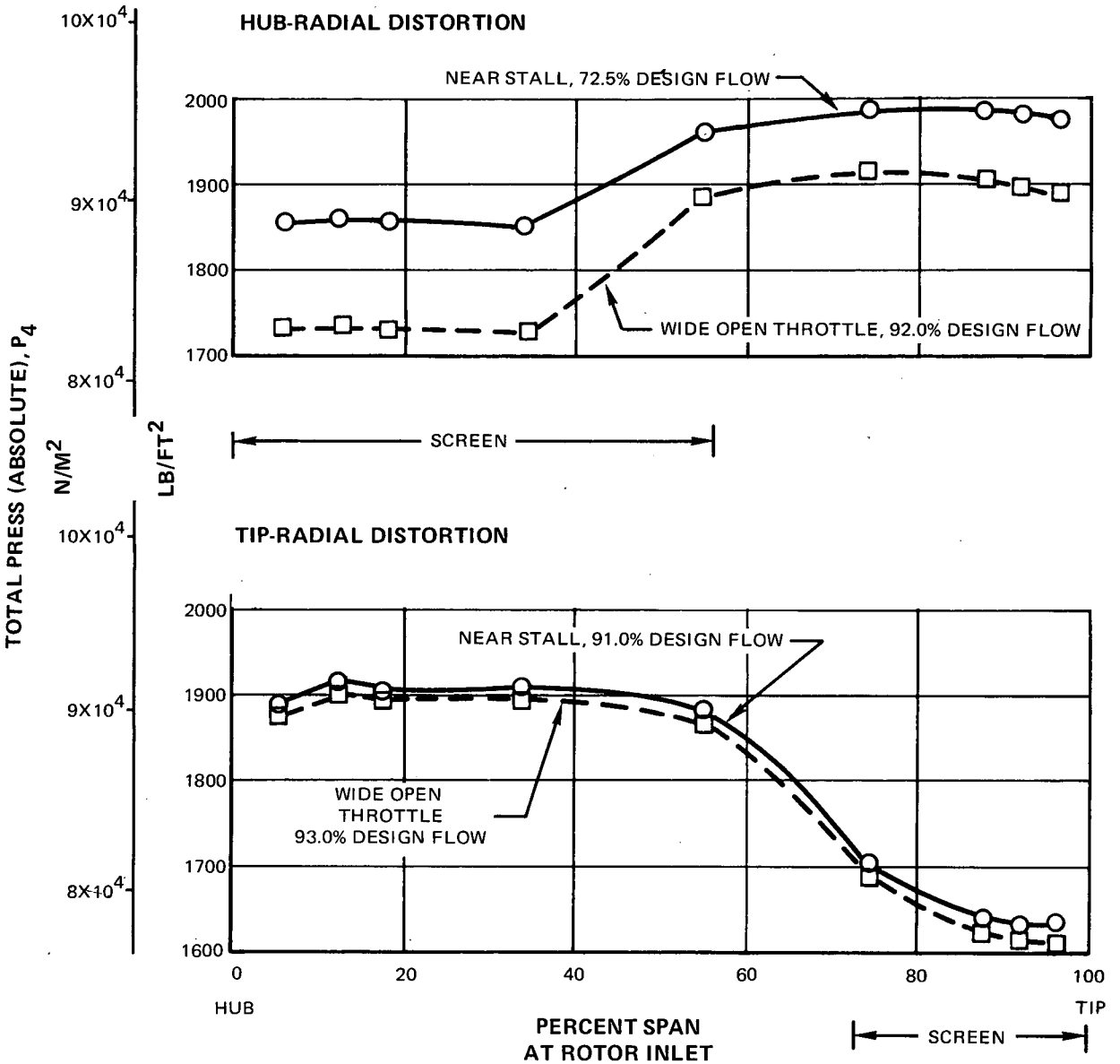

Figure 31 Radial Total Pressure Patterns at Rotor Inlet With Tip-Radial and Hub-Radial Distortions at 95% Design Speed

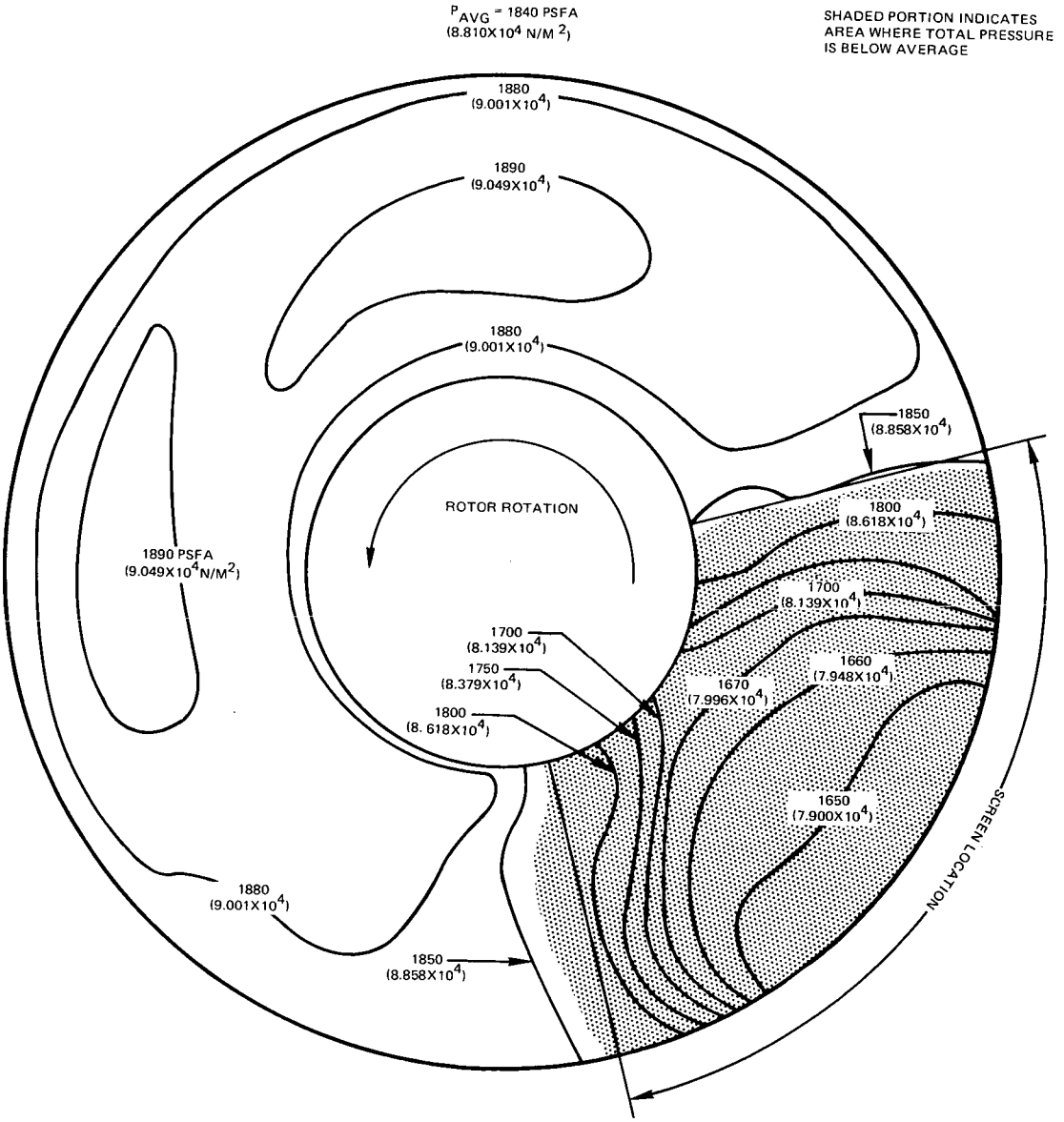

Figure 32 Total Pressure Contour Map at Rotor Leading Edge With Circumferentially Distorted Inlet Flow at 95% Design Speed and 93.7% Design Flow for Slotted-Rotor, Redesigned Stator Configuration

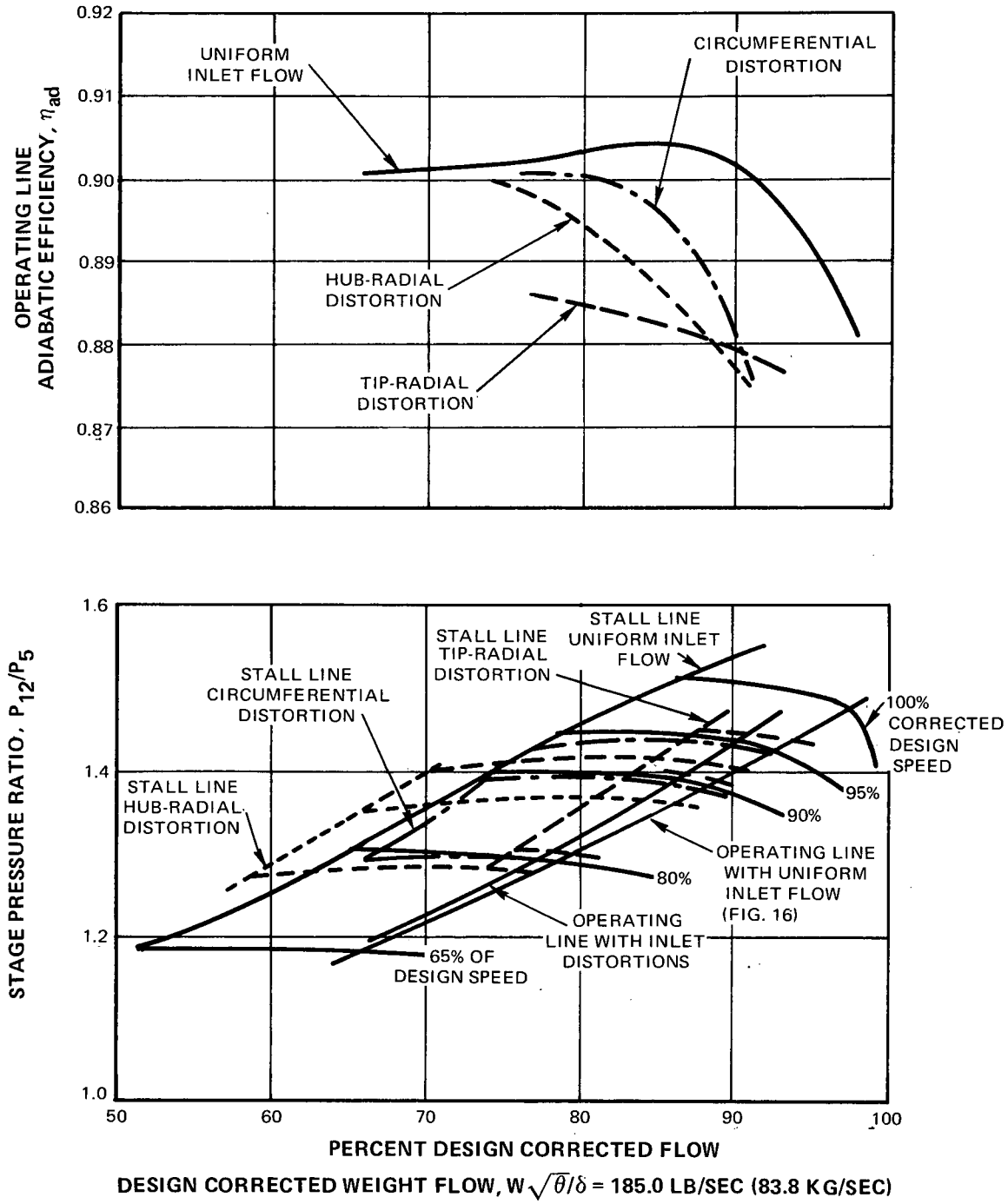

Figure 33 Composite Performance Map Showing Effects of Inlet Distortions

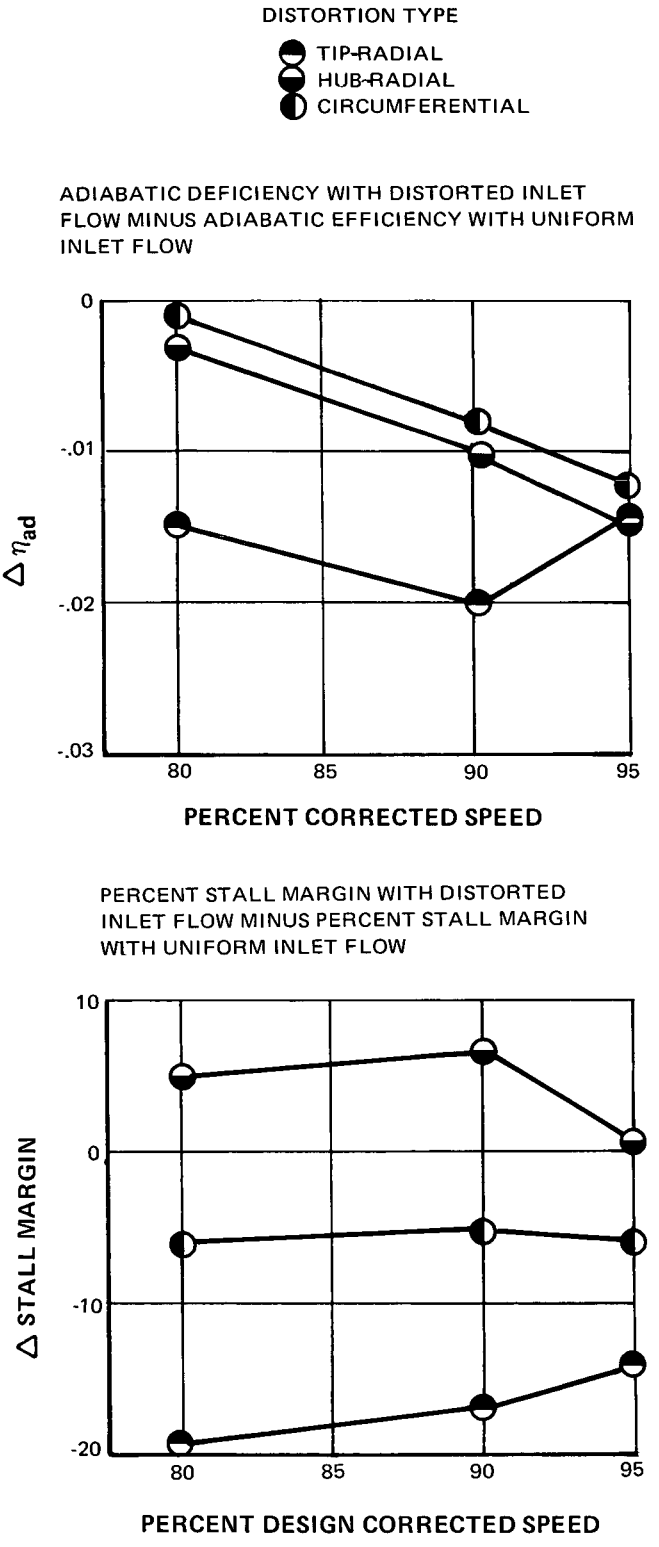

Figure 34 Effects of Distorted Inlet Flow on Operating-Line Efficiency and Stall Margin vs Speed for Slotted Rotor, Redesigned Stator Fan Configuration

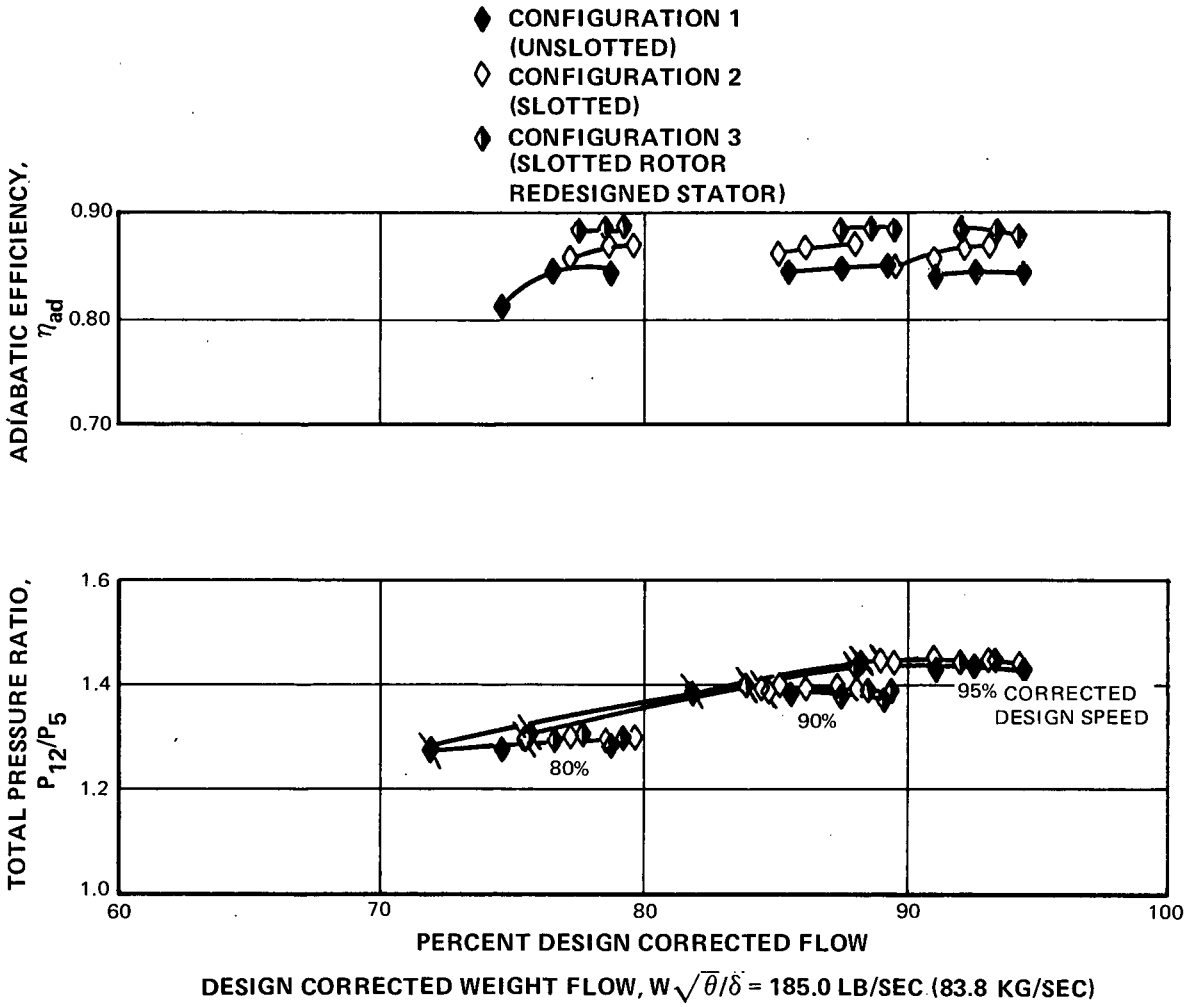

Figure 35 Fan Overall Performance With Tip-Radial Distortion of Different Fan Configurations

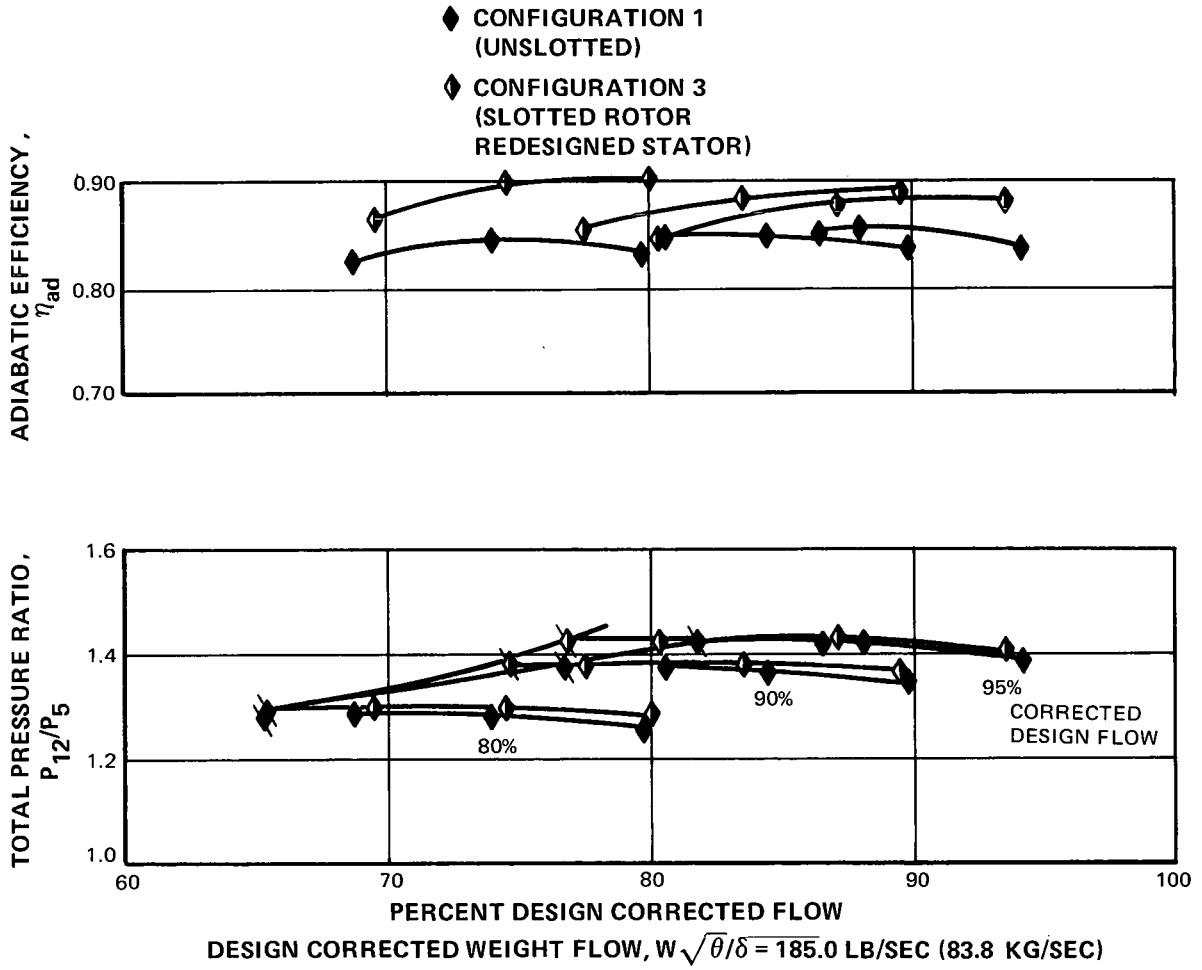

Figure 36 Fan Overall Performance With Circumferential Distortion of Different Fan Configurations

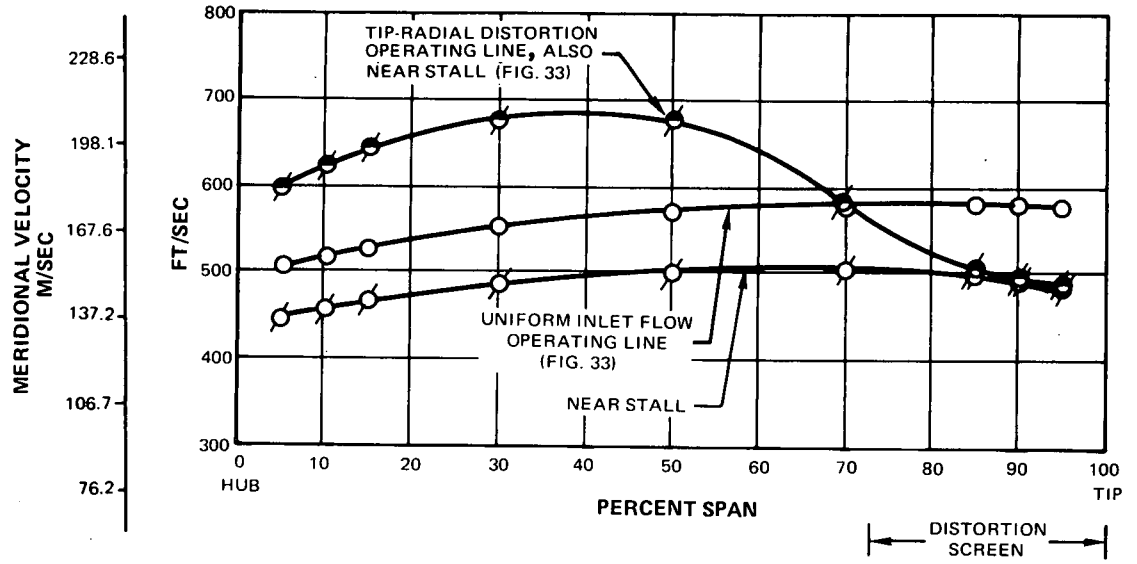

Figure 37 Fan Inlet Meridional Velocity Comparison Between Uniform Inlet and Tip-Radial Distortion Tests at 95% Design Speed With Slotted Rotor and Redesigned Stator

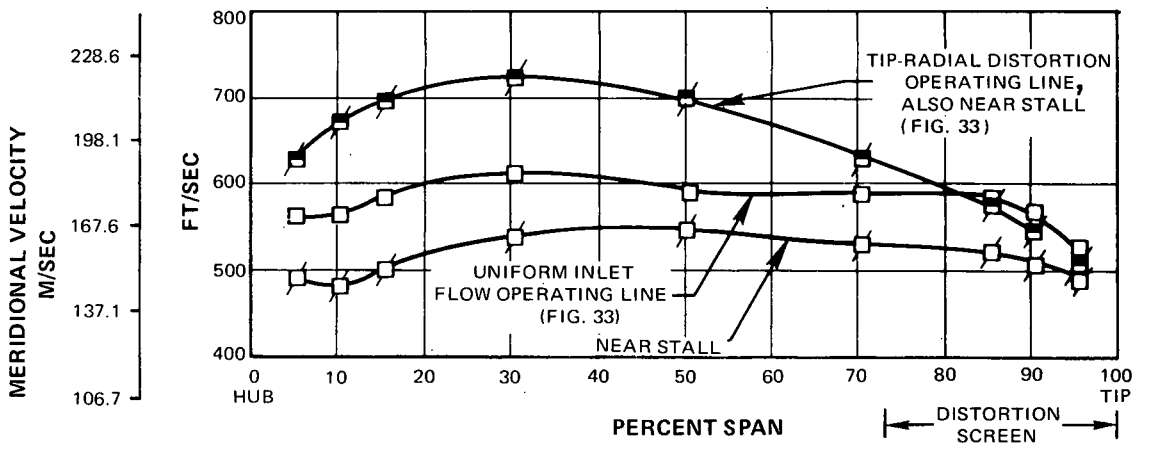

Figure 38 Fan Exit Meridional Velocity Comparison Between Uniform Inlet and Tip-Radial Distortion Tests at 95% Design Flow With Slotted Rotor and Redesigned Stator

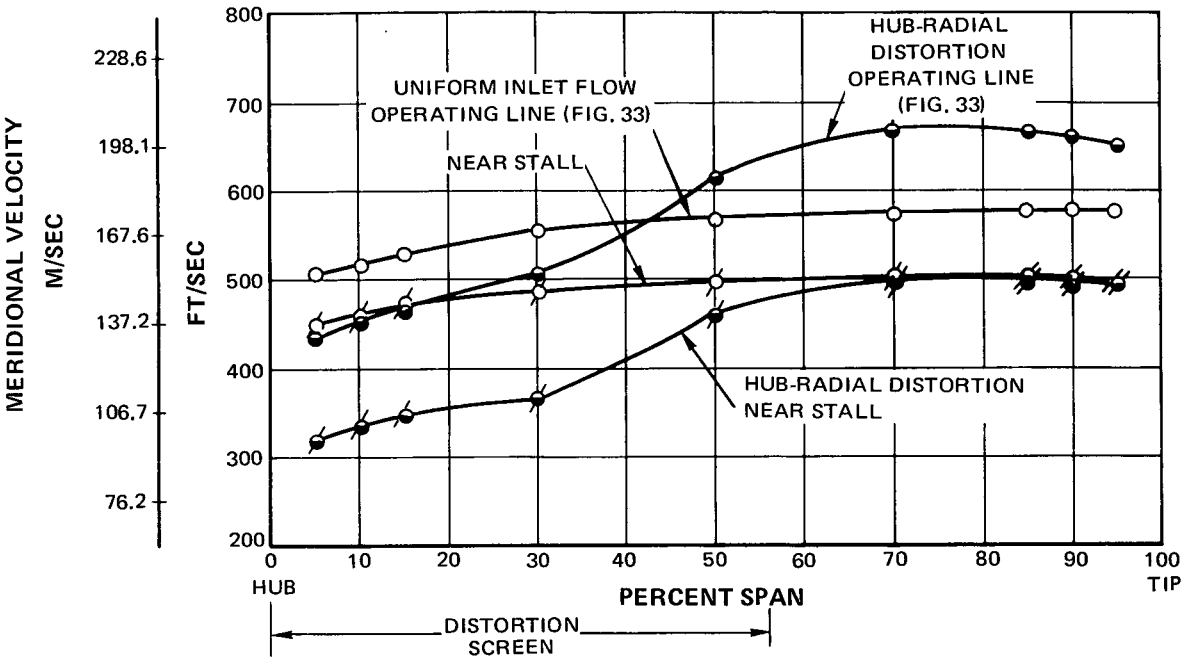

Figure 39 Fan Inlet Meridional Velocity Comparison Between Uniform Inlet and Hub-Radial Distortion Tests at 95% Design Speed With Slotted Rotor and Redesigned Stator

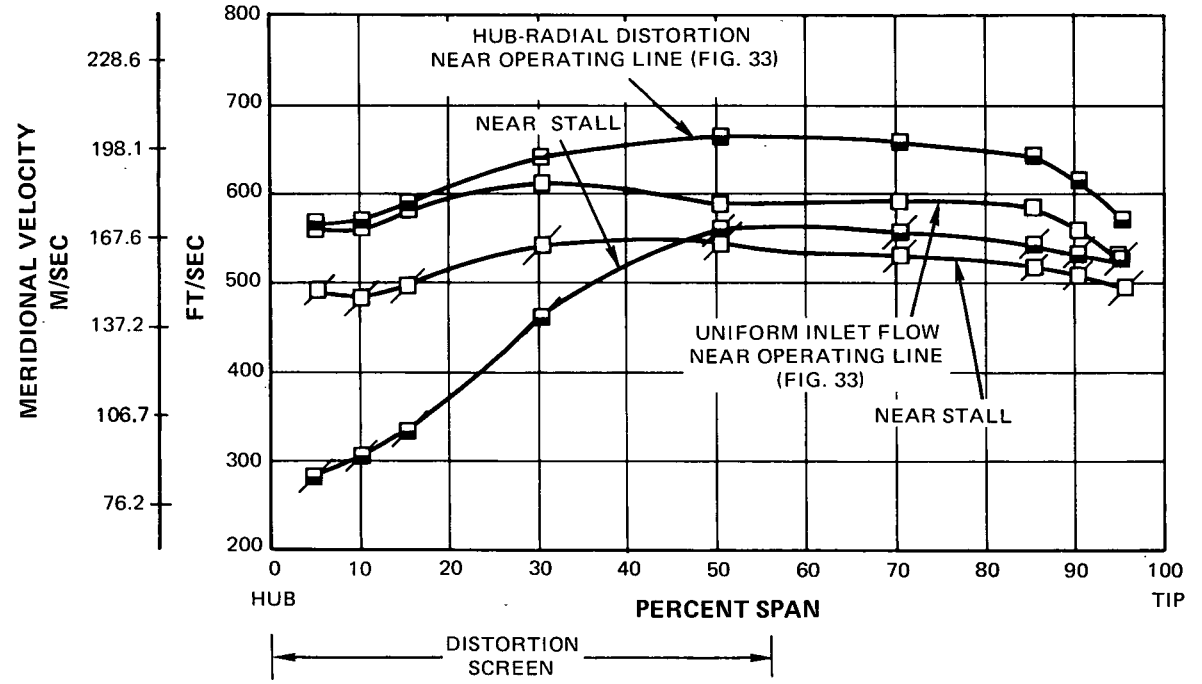

Figure 40 Fan Exit Meridional Velocity Comparison Between Uniform Inlet and Hub-Radial Distortion Tests at 95% of Design Speed With Slotted Rotor and Redesigned Stator

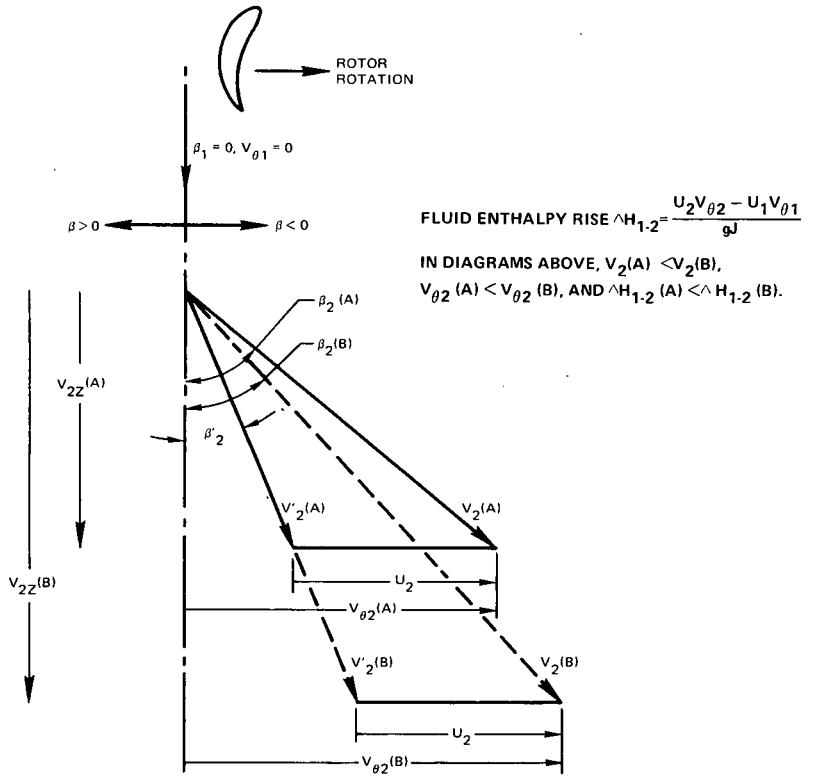

Figure 41 Effect of Rotor Exit Velocity on Fluid Enthalpy Rise for Past-Axial Relative Flow Angle at Rotor Exit

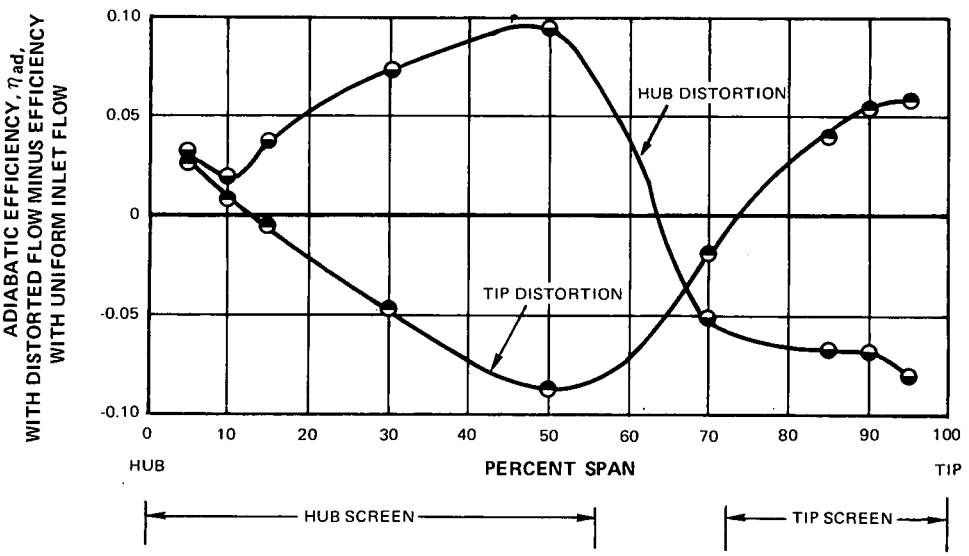

Figure 42 Effect of Radial-Distortions on Rotor Efficiency vs Span for Operating-Line Data Points at 95% of Design Speed With Slotted-Rotor, Redesigned Stator Configuration

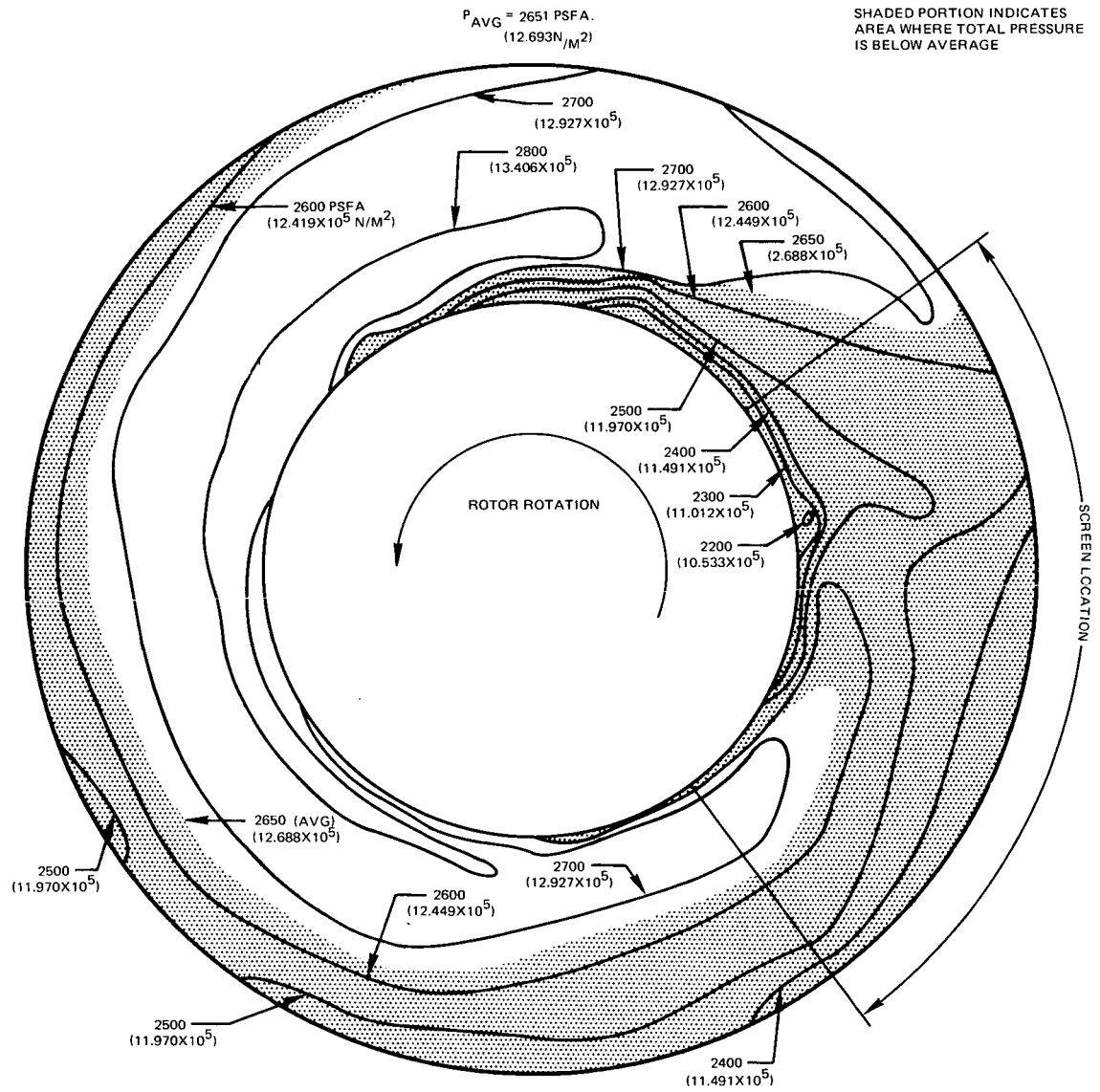

Figure 43 Total Pressure Contour Map at Stator Leading Edge With Circumferentially Distorted Inlet Flow at 95% of Design Speed and 93.7% of Design Corrected Flow

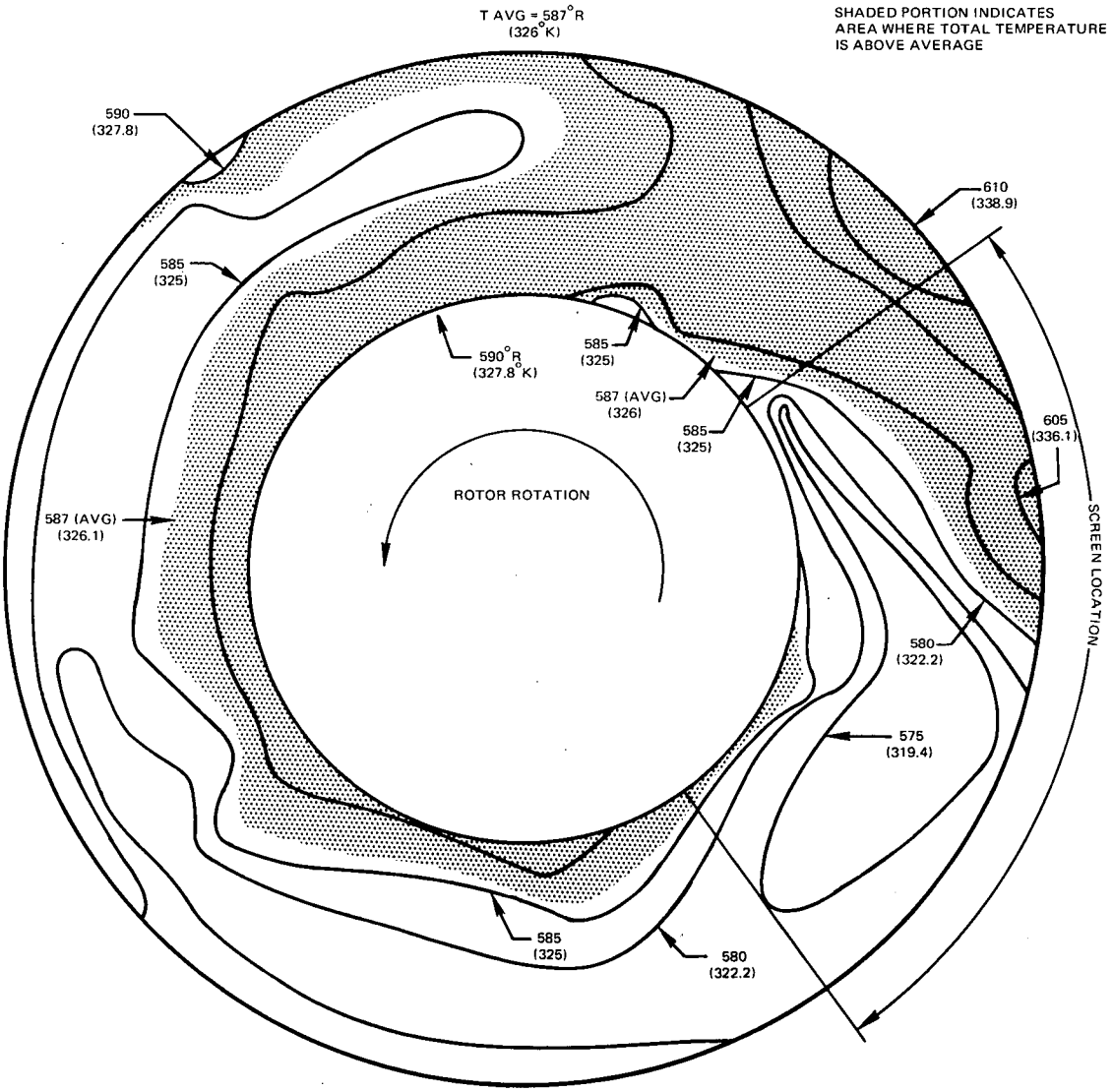

Figure 44 Total Temperature Contour Map at Stator Leading Edge With Circumferentially Distorted Inlet Flow at 95% of Design Speed and 93.7% of Design Corrected Flow

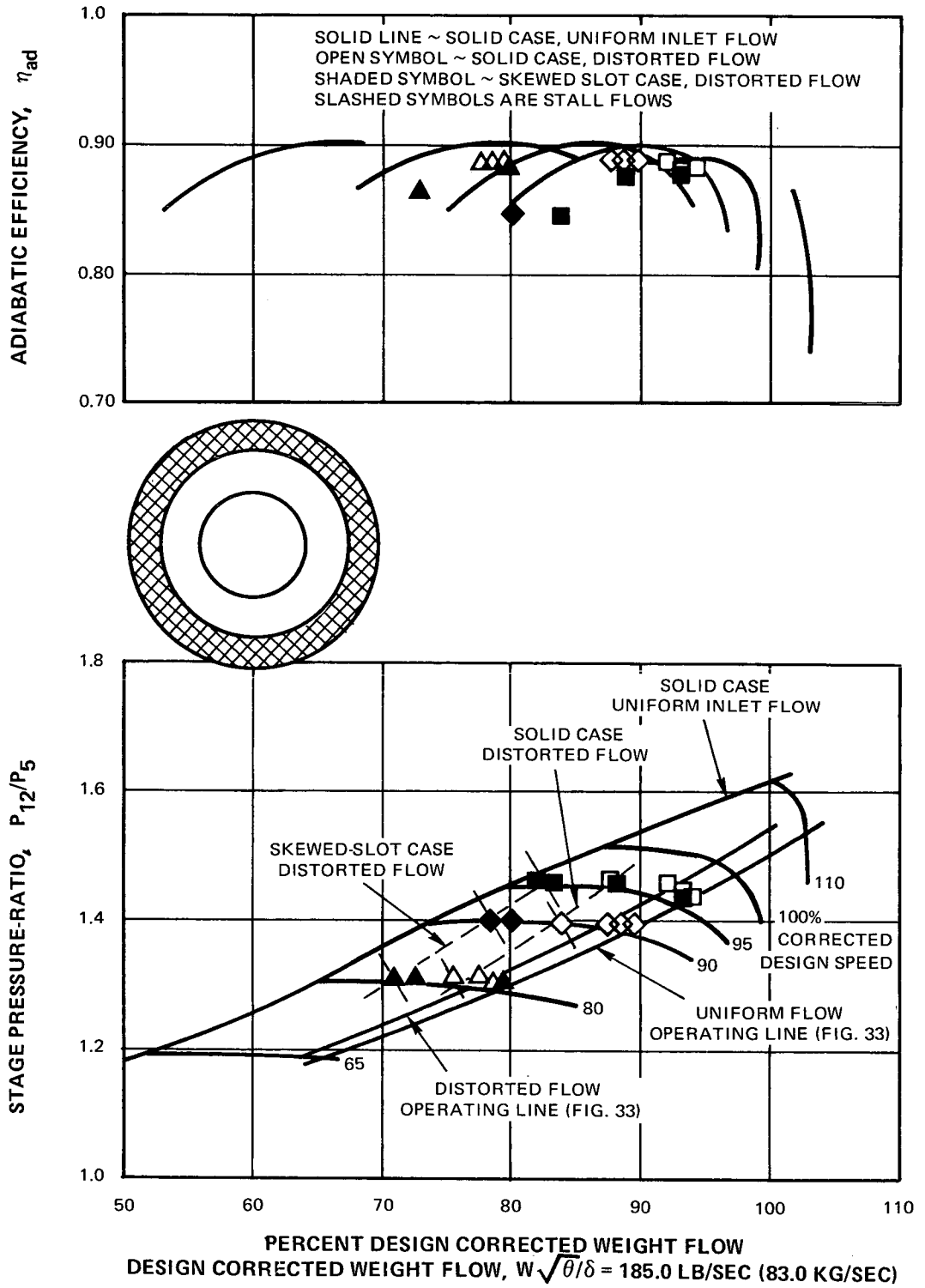

Figure 45 Effect of Skewed-Slot Casing Over Rotor Tip on Fan Overall Performance With Tip-Radial Distortion for Slotted-Rotor, Redesigned-Stator Fan-Configuration

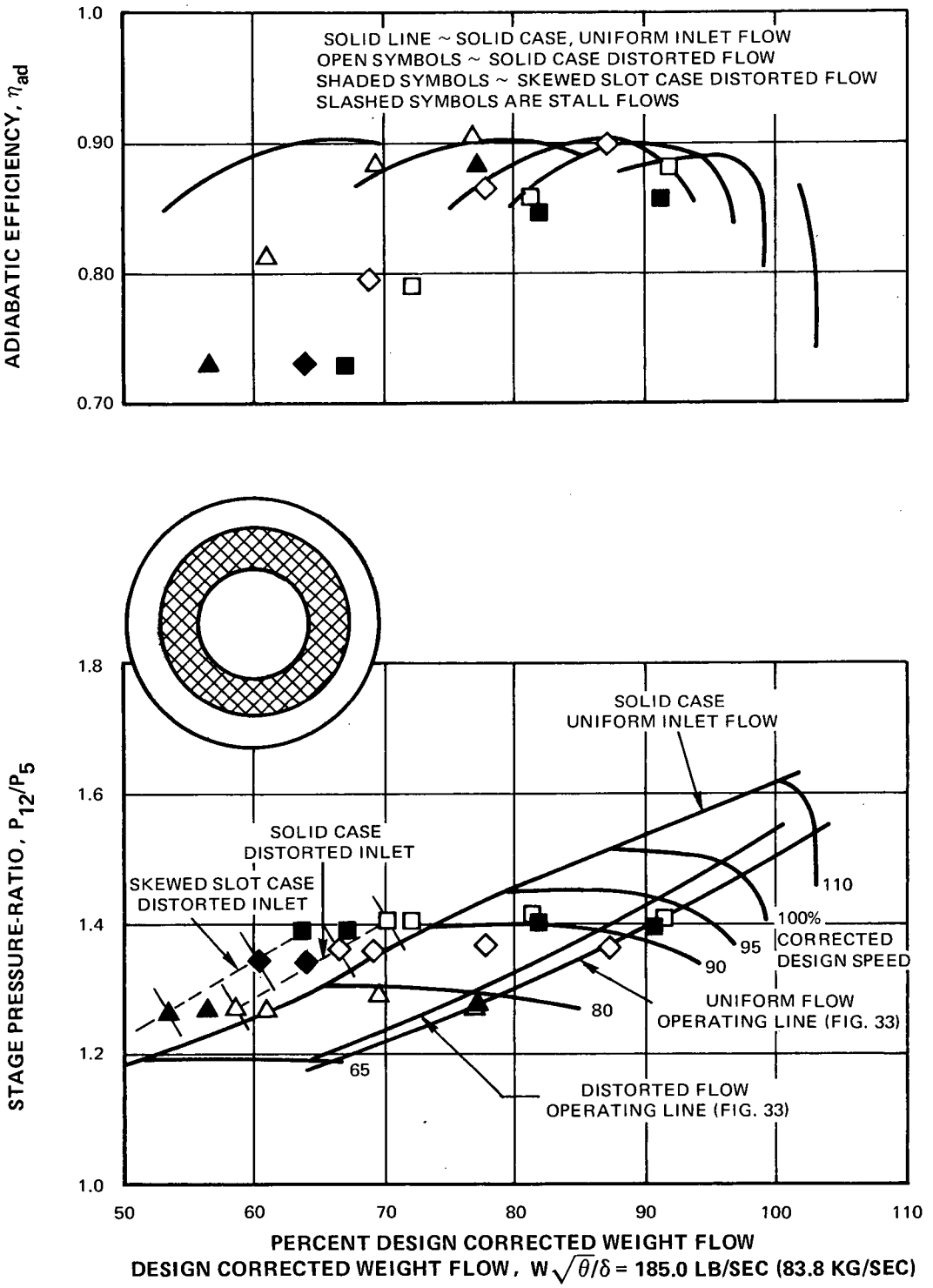

Figure 46 Effects of Skewed-Slot Casing Over Rotor Tip on Fan Overall Performance With Hub-Radial Distortion for Slotted-Rotor, Redesigned-Stator Fan-Configuration

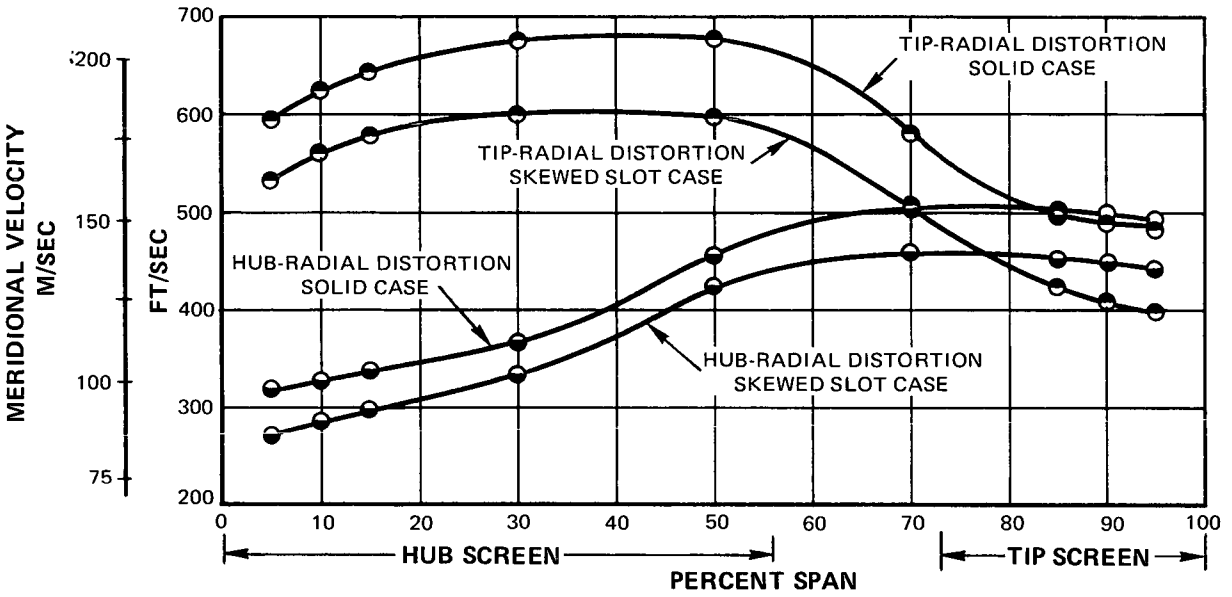

Figure 47 Effect of Skewed Slot Casing Over Rotor Tip on Fan-Inlet, Meridional Velocity for Hub-Radial and Tip-Radial Distortion Tests at 95% of Design Speed, Near-Stall With Slotted-Rotor, Redesigned-Stator Fan-Configuration

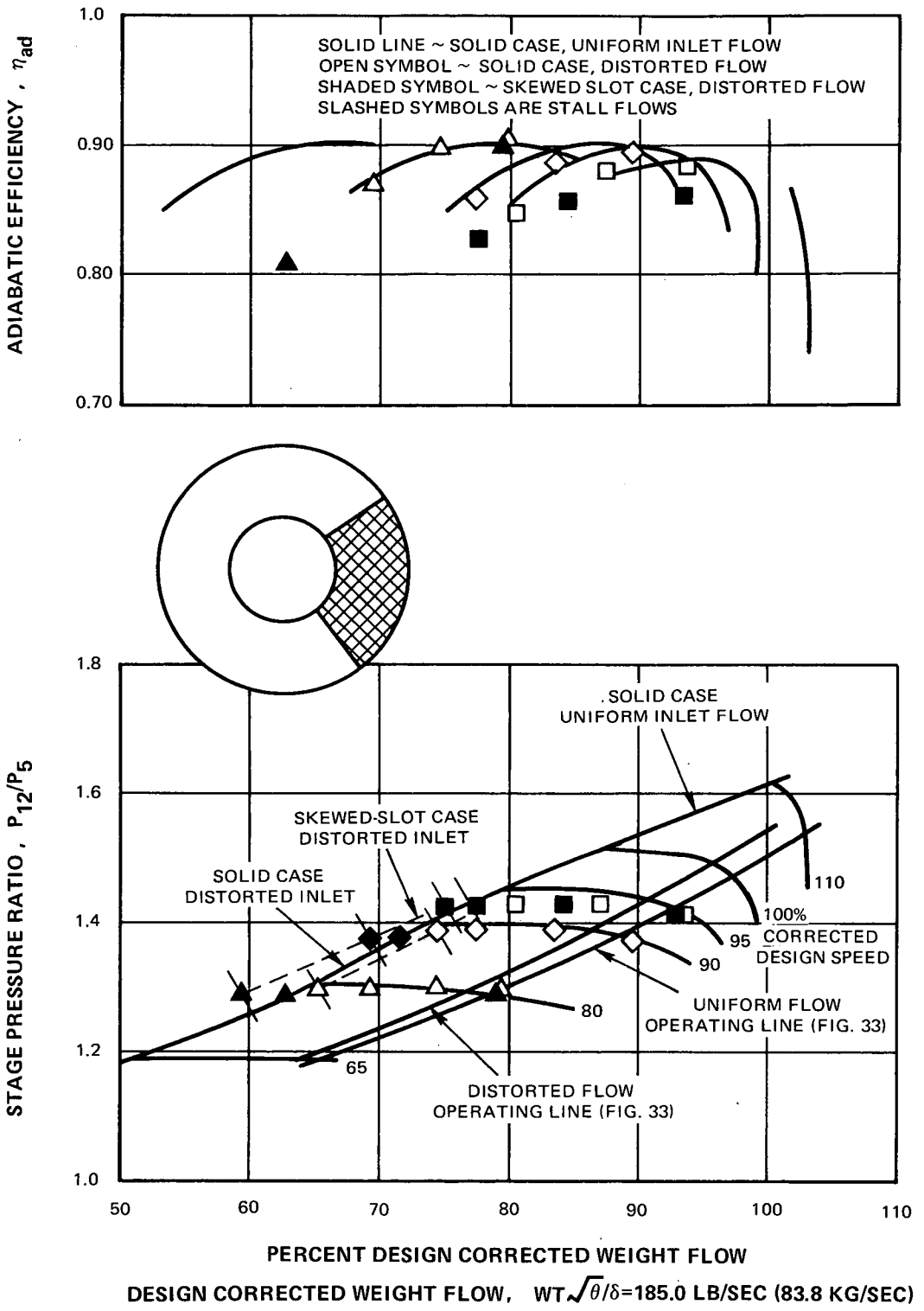

Figure 48 Effect of Skewed-Slot Casing Over Rotor Tip on Fan Overall Performance With Circumferential Distortion for the Slotted-Rotor, Redesigned-Stator Fan-Configuration

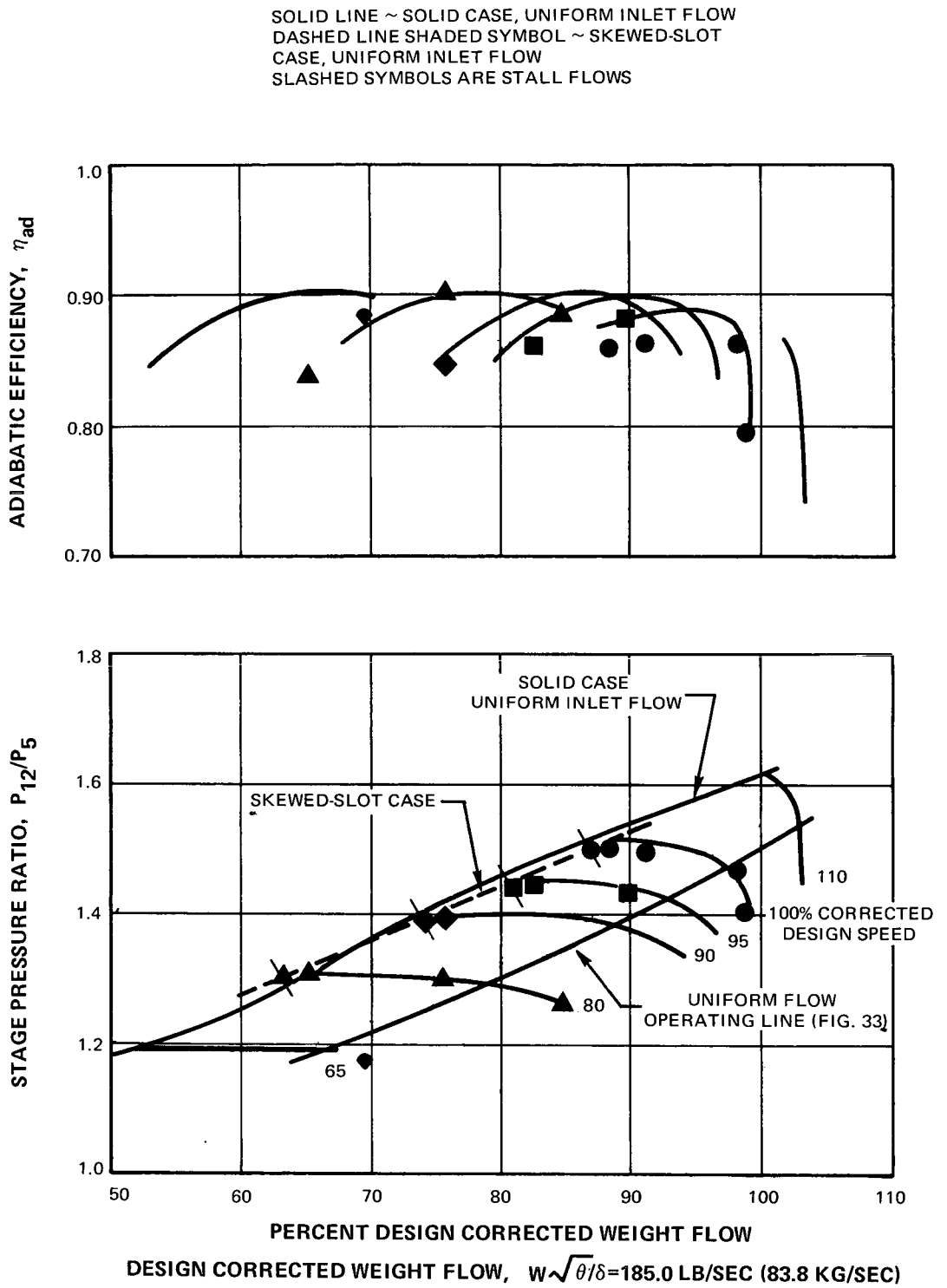

Figure 49 Effect of Skewed-Slot Casing Over Rotor Tip on Fan Overall Performance With Uniform Inlet Flow for Slotted-Rotor, Redesigned-Stator Fan-Configuration

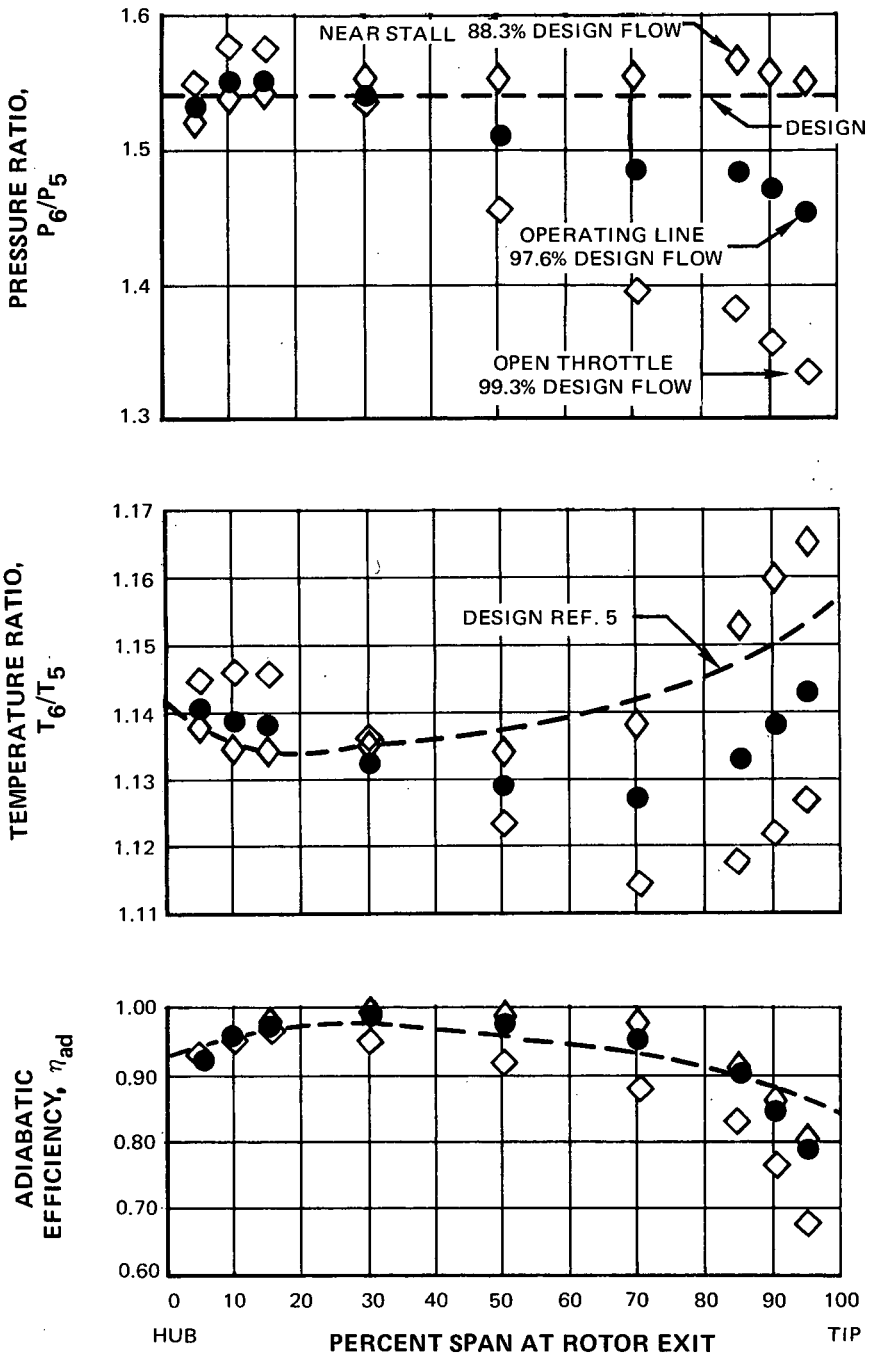

Figure 50 Spanwise Distributions of Slotted-Rotor Pressure Ratio, Temperature Ratio, and Efficiency at Design Speed With Uniform Inlet Flow and Redesigned Stator

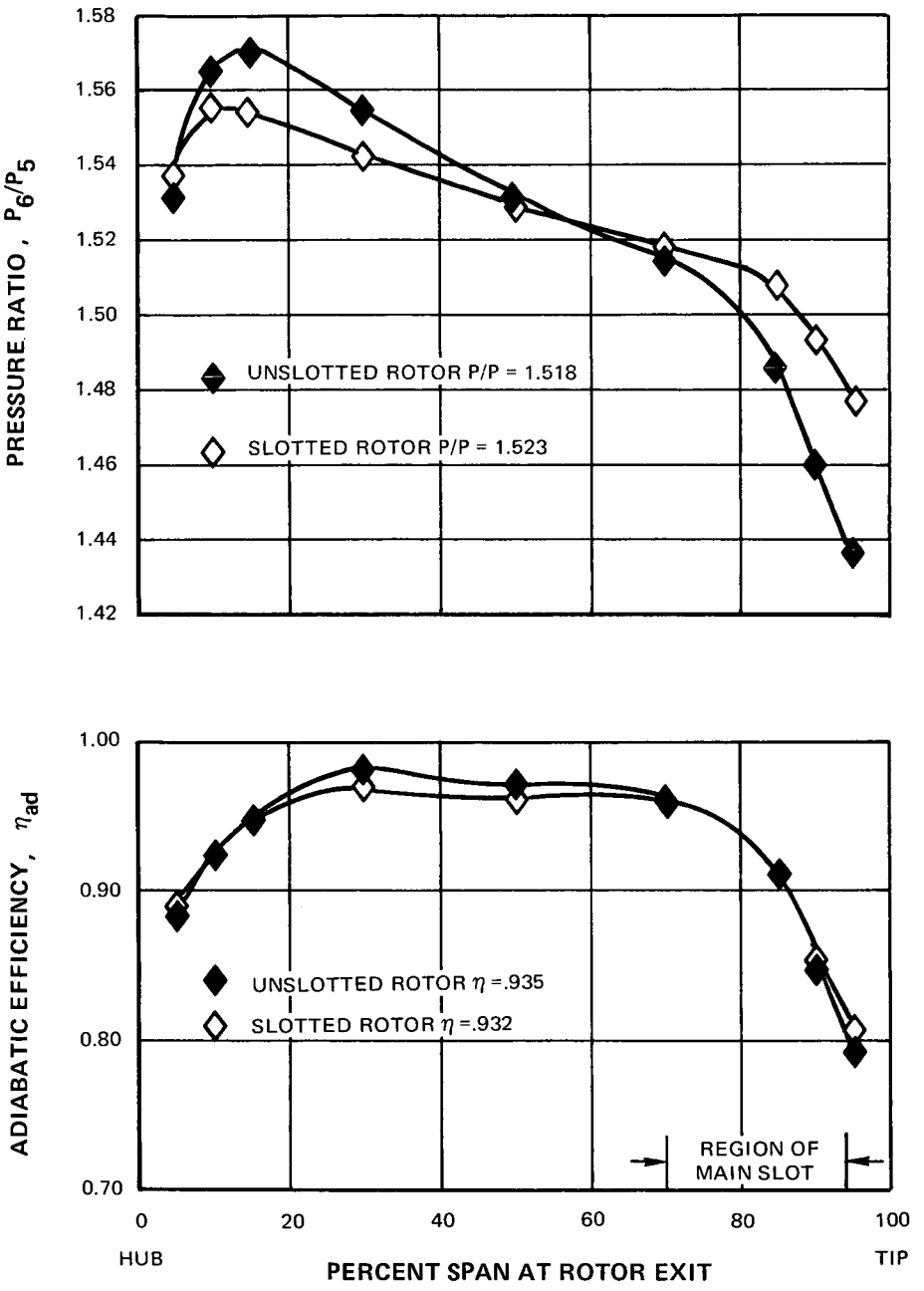

Figure 51 Spanwise Profiles of Pressure Ratio and Efficiency for Slotted and Unslotted Rotor Blades at Design Speed With Original Stators

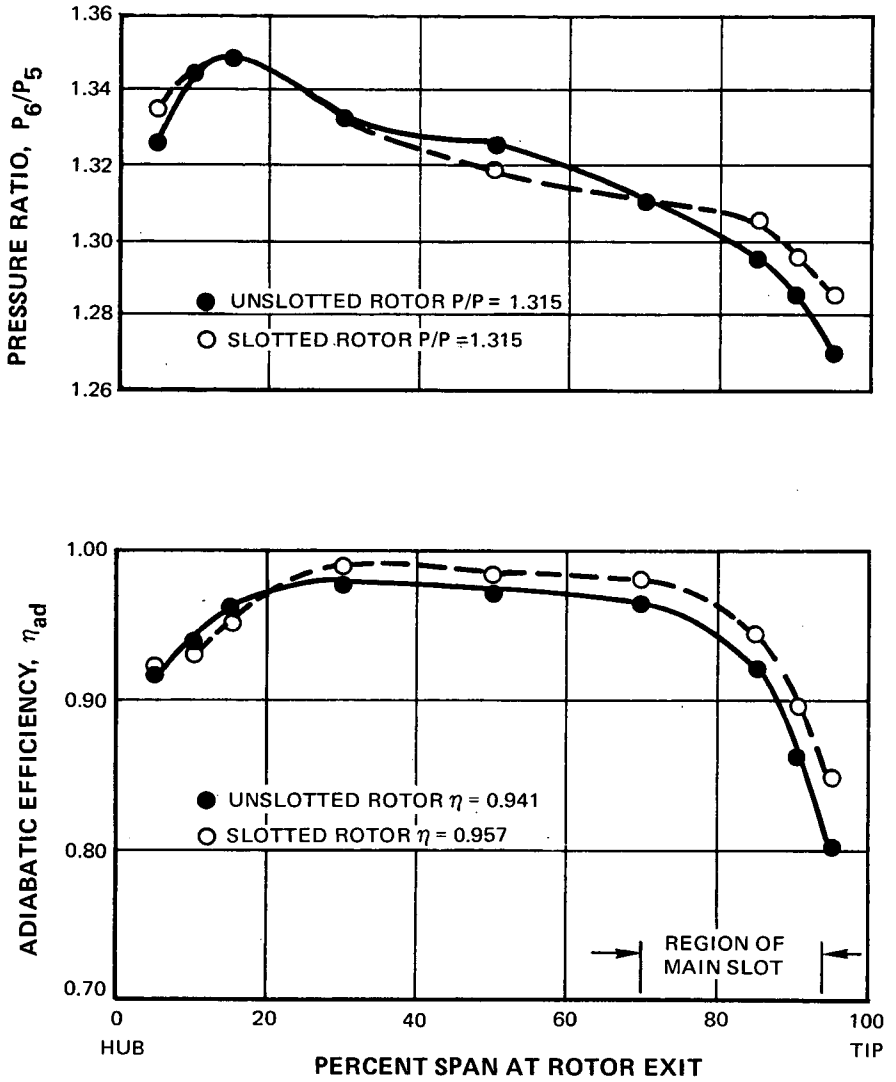

Figure 52 Spanwise Profiles of Pressure Ratio and Efficiency for Slotted and Unslotted Rotor Blades at 80% Design Speed With Original Stators

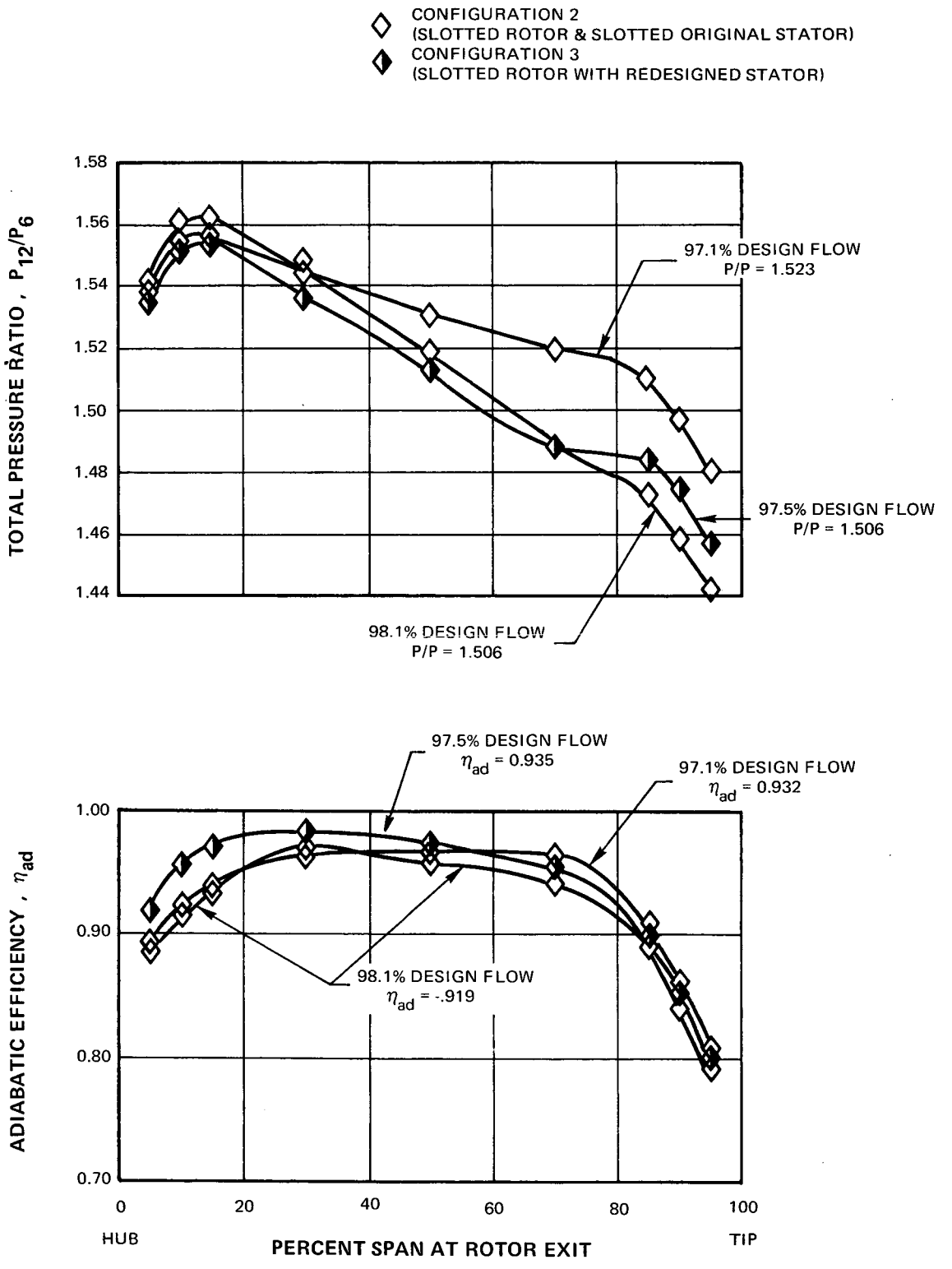

Figure 53 Spanwise Profile of Pressure Ratio and Efficiency for Slotted Rotor With Slotted-Original and Redesigned Stators at Design Speed

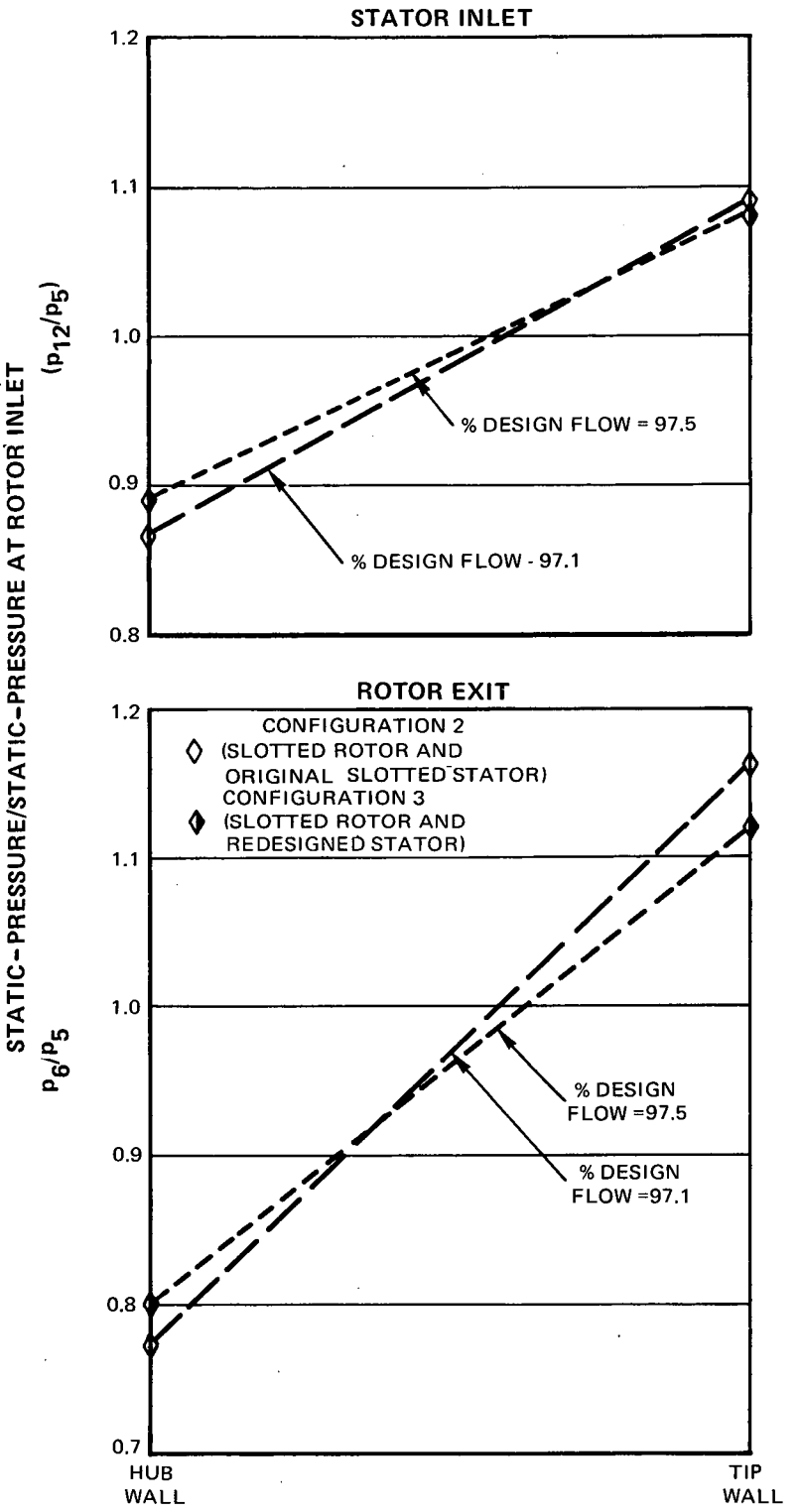

Figure 54 Effect of Stator Configuration on Overall Radial Gradients of Static Pressure at Rotor Exit and Stator Inlet

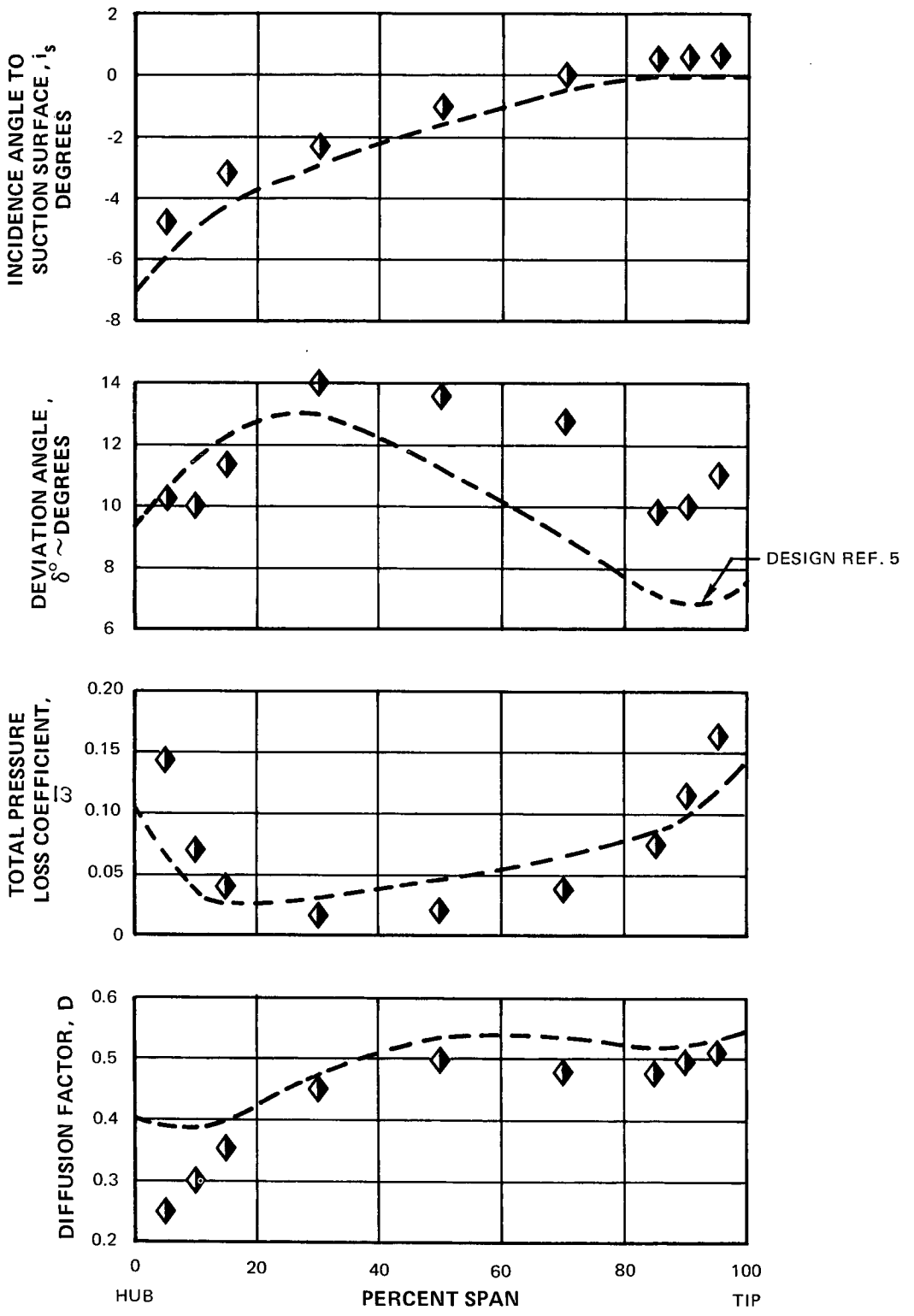

Figure 55 Spanwise Distributions of Slotted-Rotor (With Redesinged Stator) Blade Element Performance Parameters Near the Operating Line at 97.5% of Design Flow Compared to Design Estimates

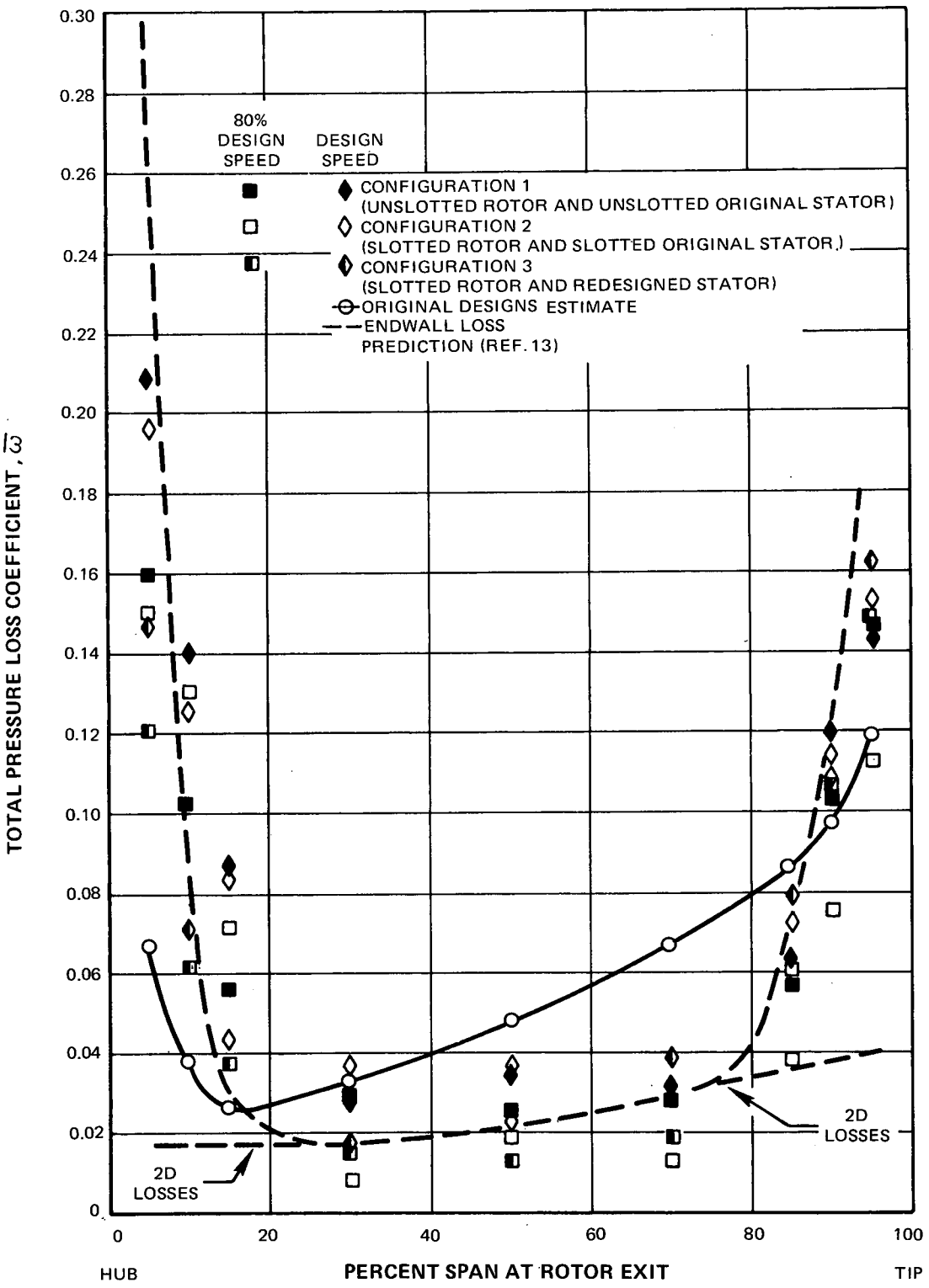

Figure 56 Spanwise Distribution of Rotor Loss Coefficient Near the Operating Line Compared to Design Estimate and Endwall Loss Prediction System

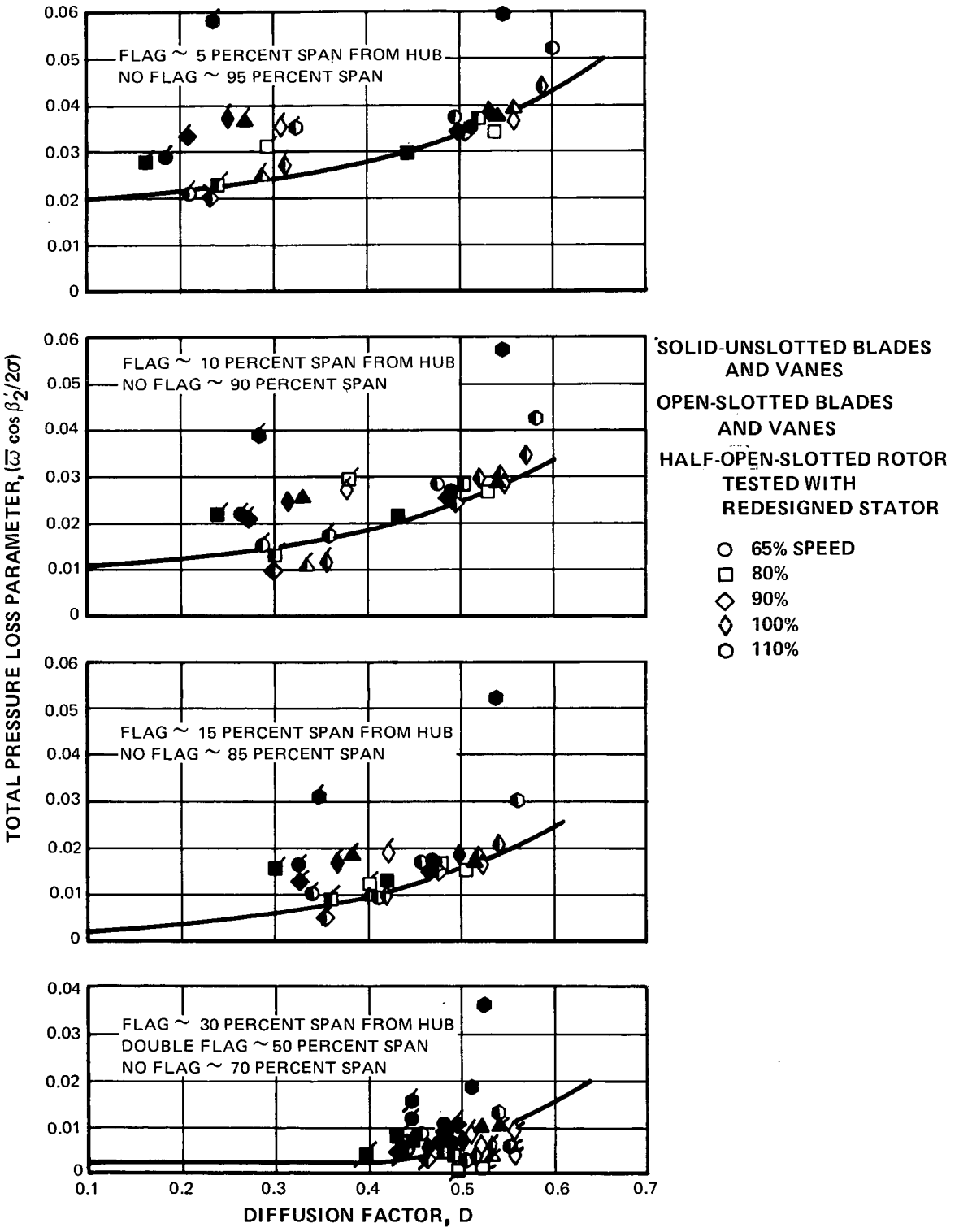

Figure 57 Rotor Total Loss Parameter vs Diffusion Factor

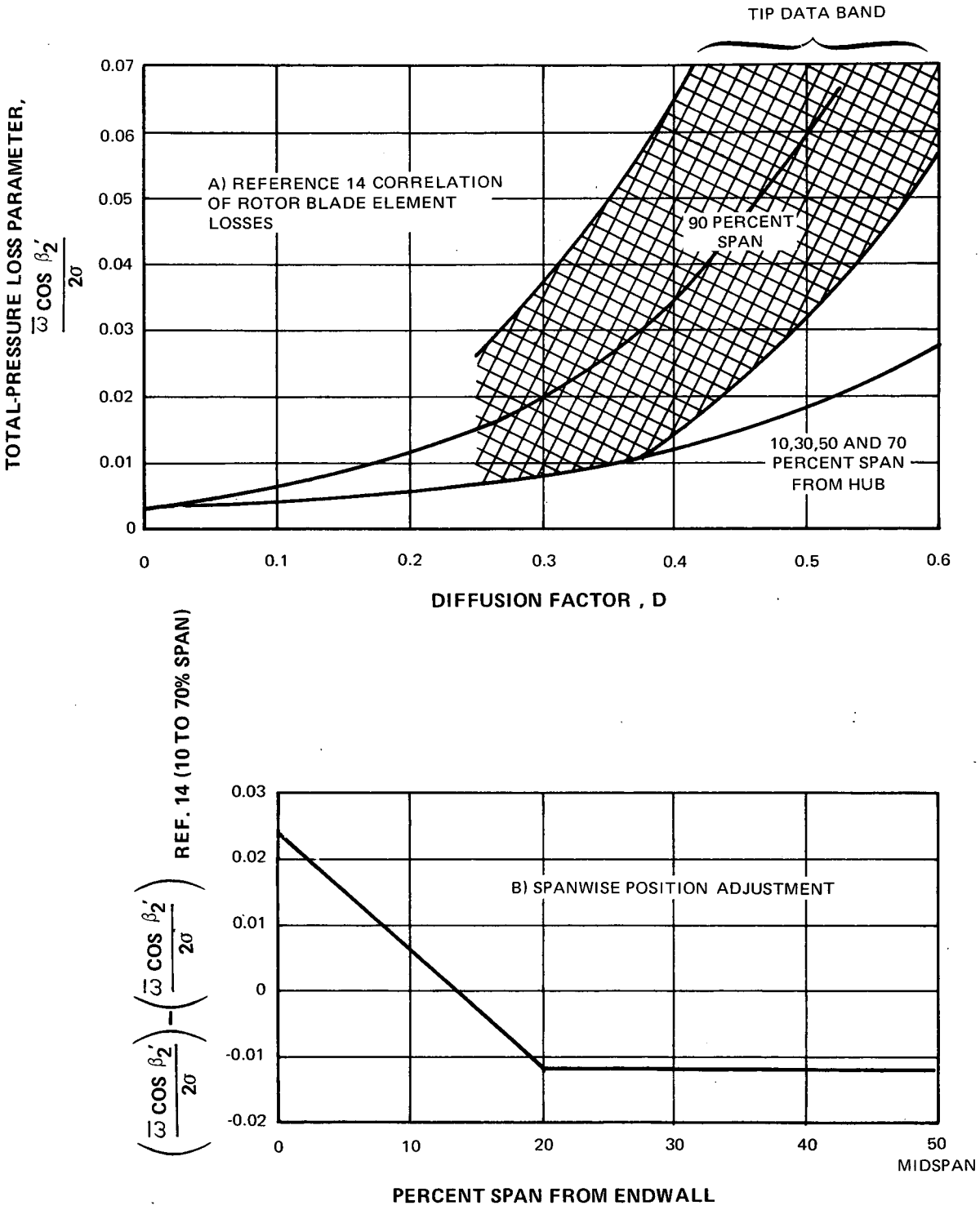

Figure 58 Correlation of Rotor Loss Parameter vs Diffusion Factor Showing Spanwise Position Effect

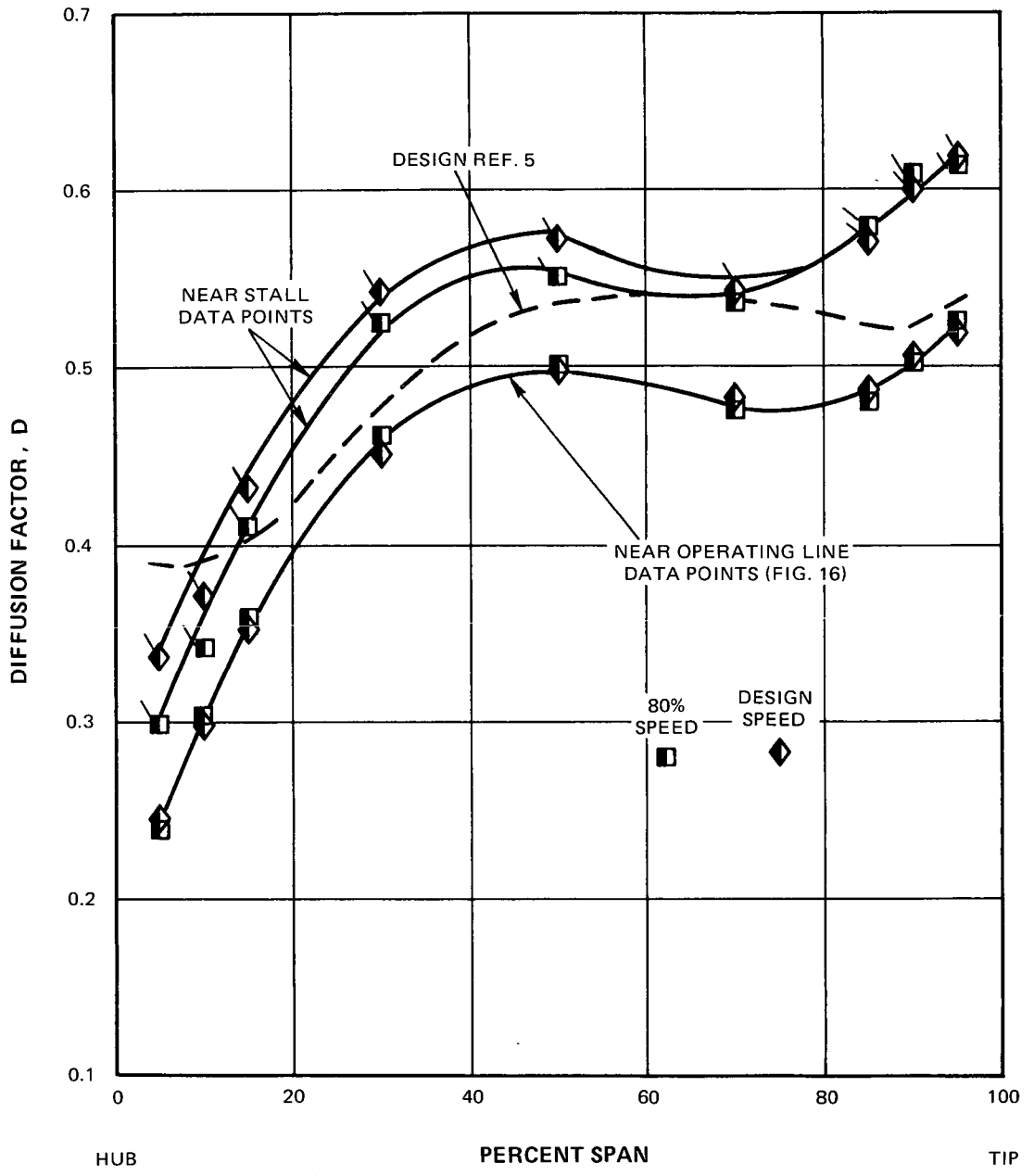

Figure 59 Spanwise Distribution of Rotor Loadings Near Operating Line and Near Stall for the Slotted Rotor With the Redesigned Stator

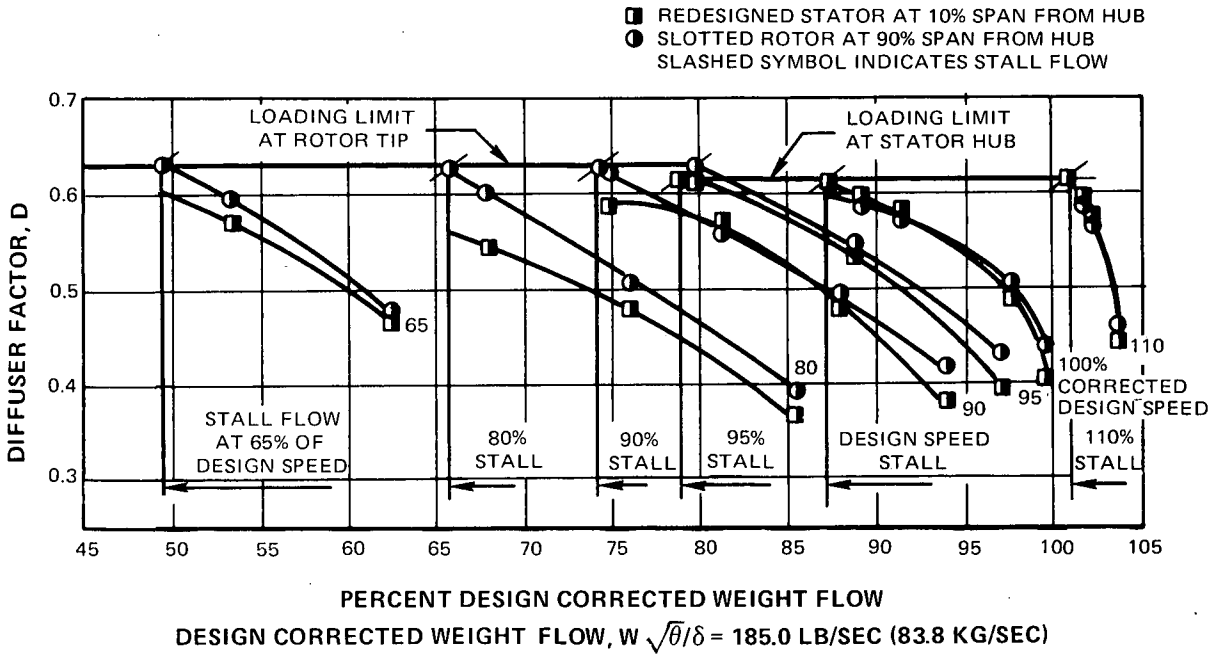

Figure 60 Correlation of Fan Stall vs Loading for Slotted Rotor and Redesigned Stator

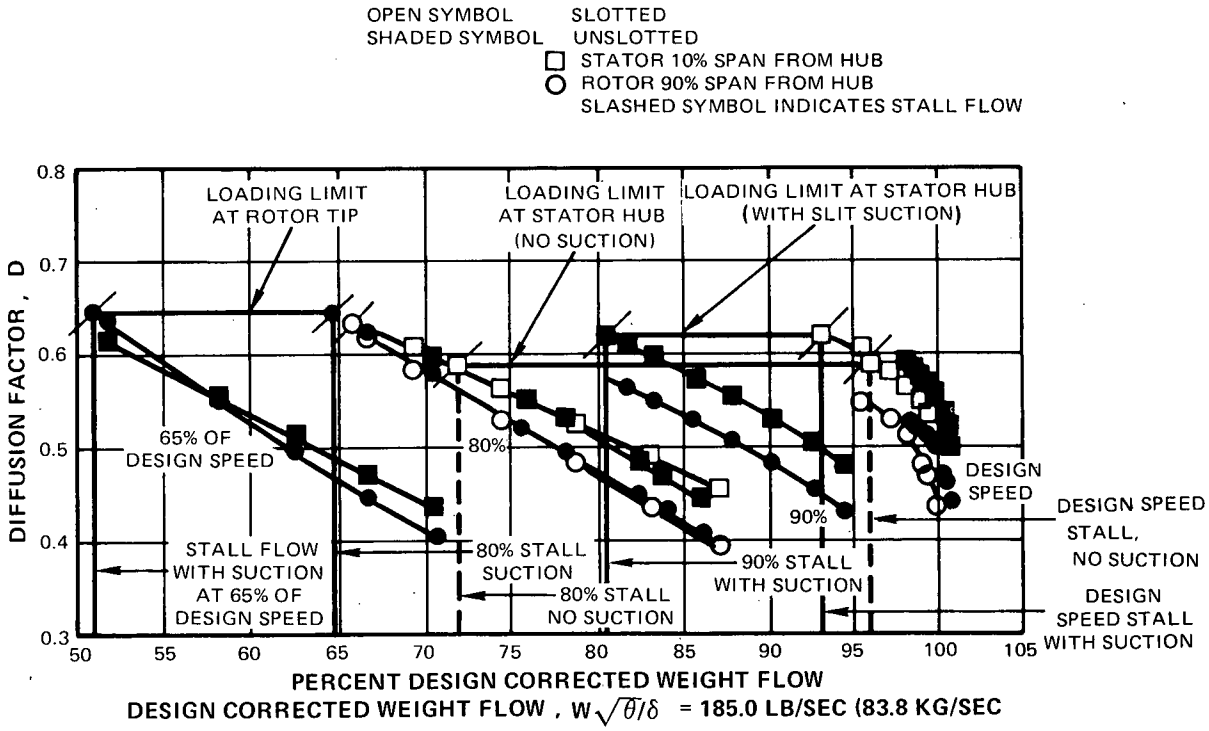

Figure 61 Correlation of Fan Stall as a Function of Blade and Vane Loading for Unslotted and Slotted Rotor and Stator With and Without Suction at Stator Hub

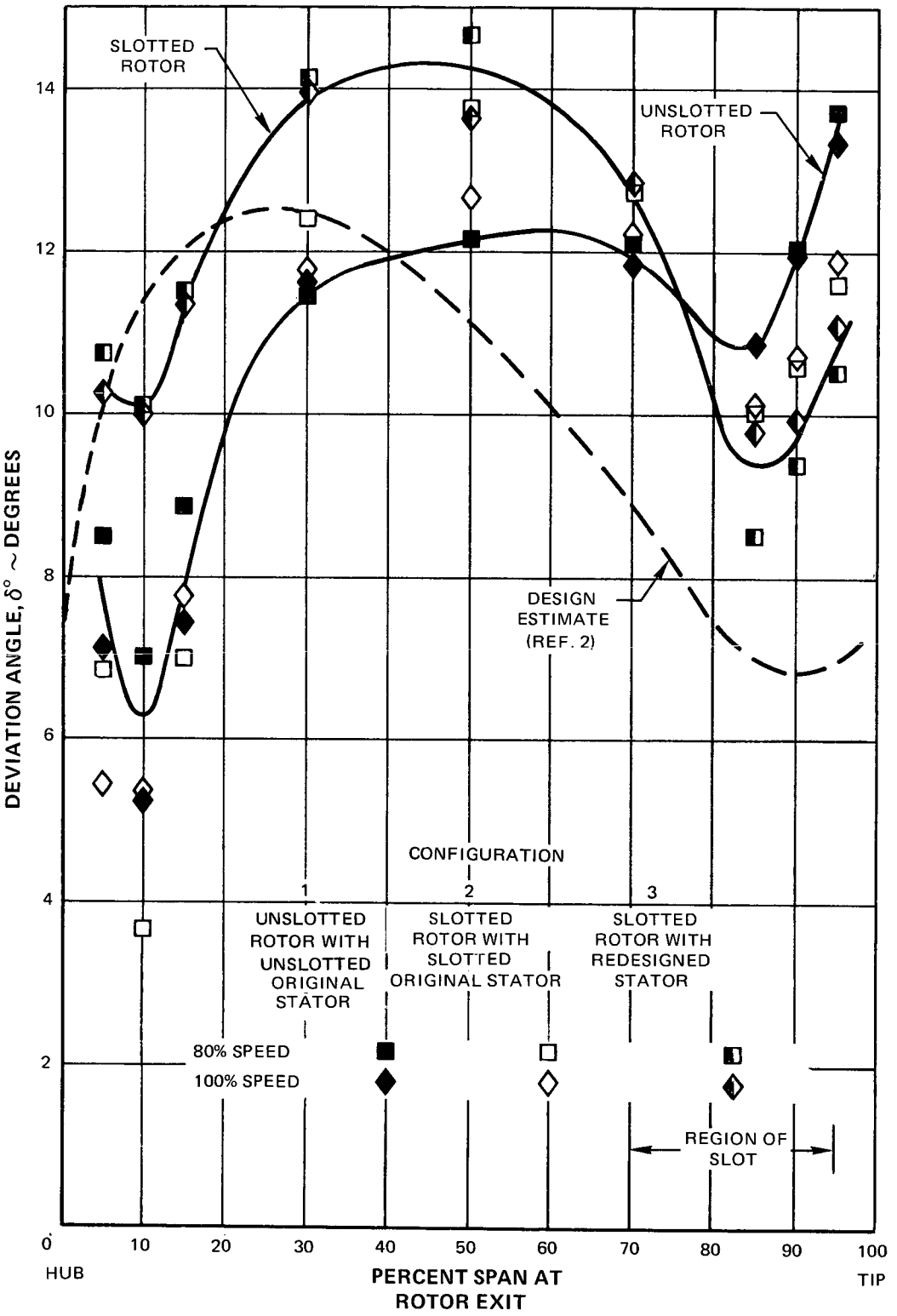

Figure 62 Rotor Deviation Angle at Minimum Loss Incidence Angles vs Span for Unslotted and Slotted Blades

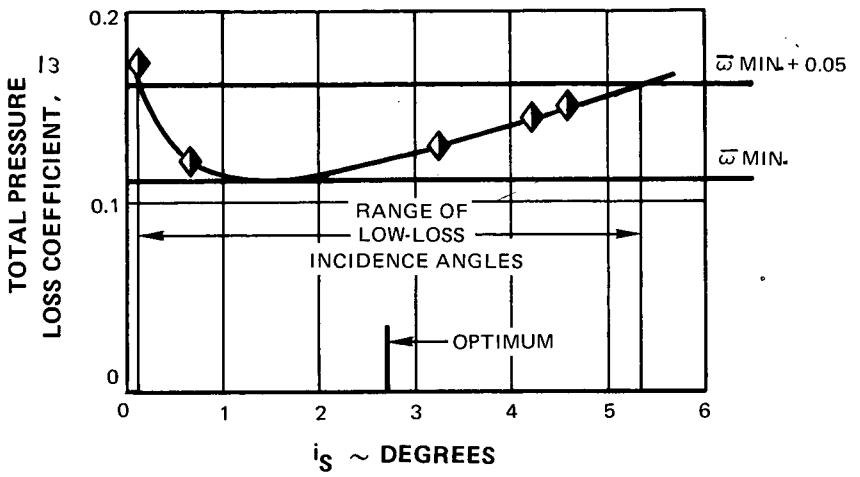

Figure 63 Range and Optimum Incidence of Slotted Rotor (With Redesigned Stator) at 90% Span from Hub

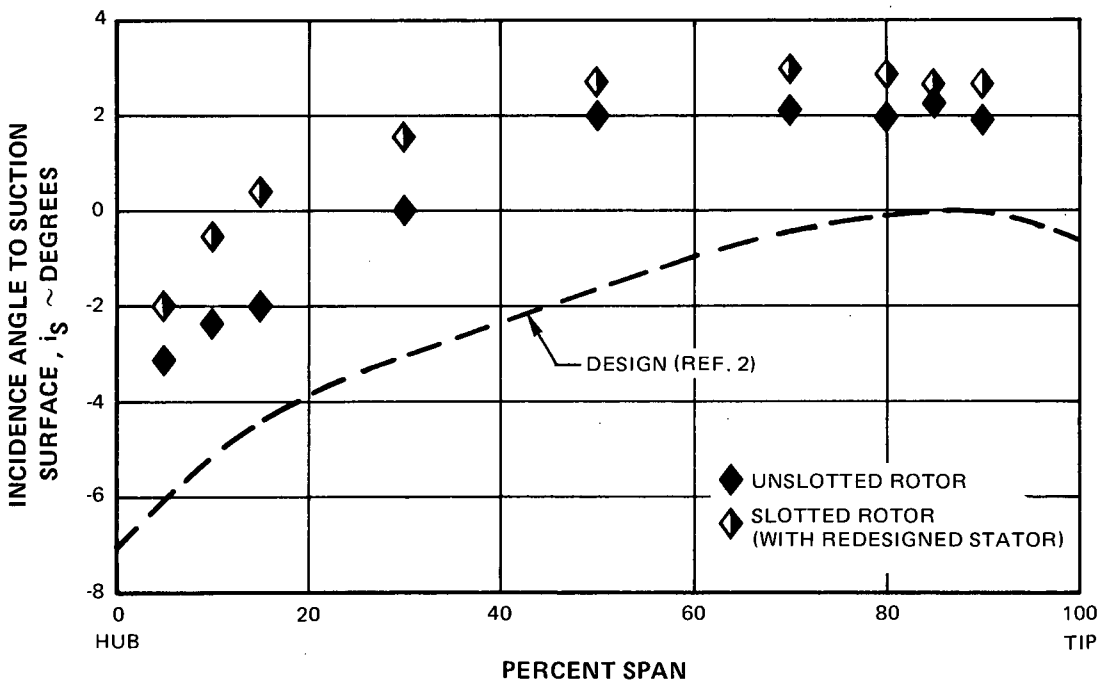

Figure 64 Rotor Optimum Incidence Angles vs Span Compared to Design

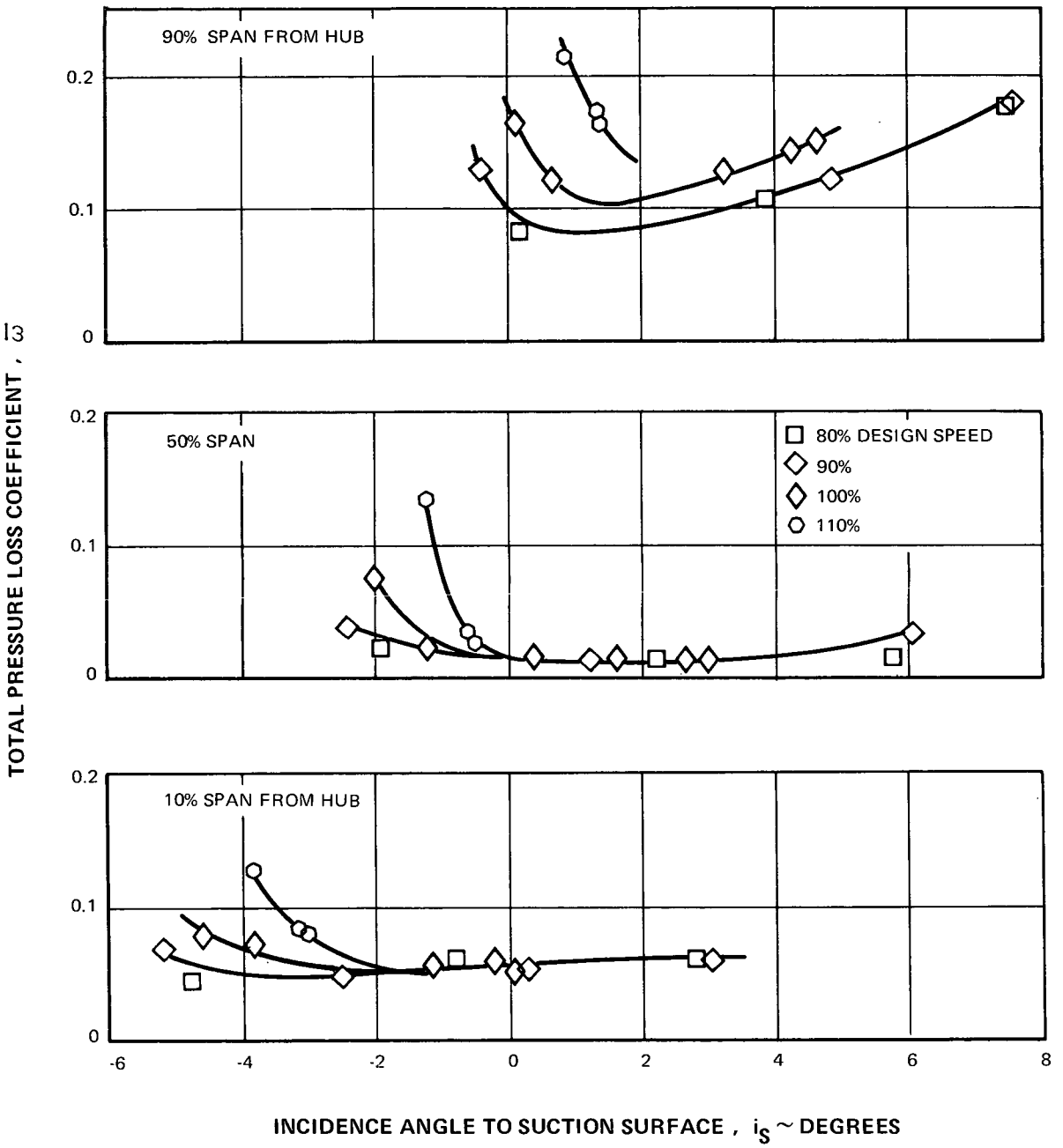

Figure 65 Slotted Rotor (With Redesigned Stator) Loss Coefficient vs Incidence Angle at 10, 50, and 90% Span from the Hub

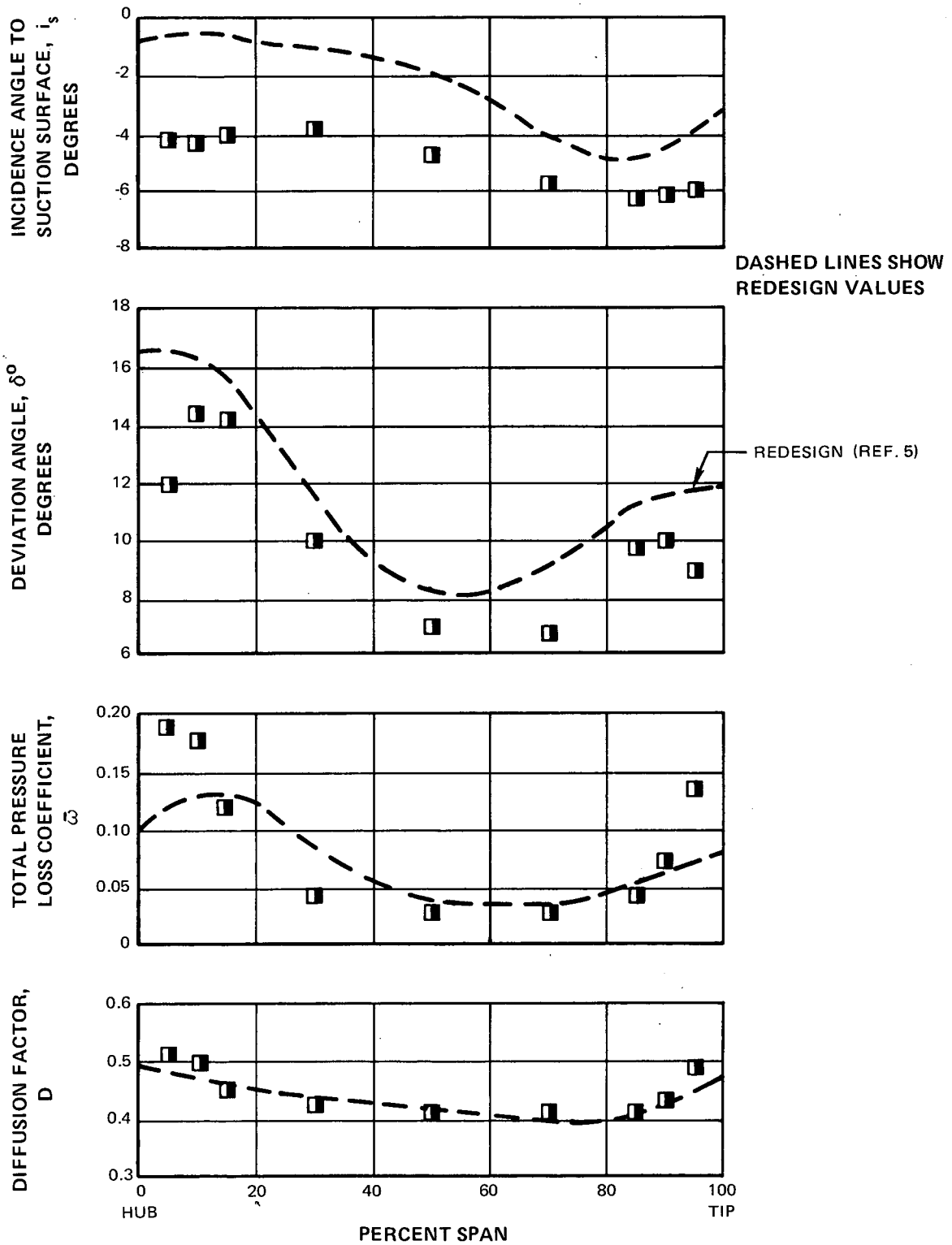

Figure 66 Spanwise Distributions of Redesigned-Stator Blade Element Performance Parameters on an Operating Line at 97.5% of Design Flow Compared to Redesign Estimates

C-2

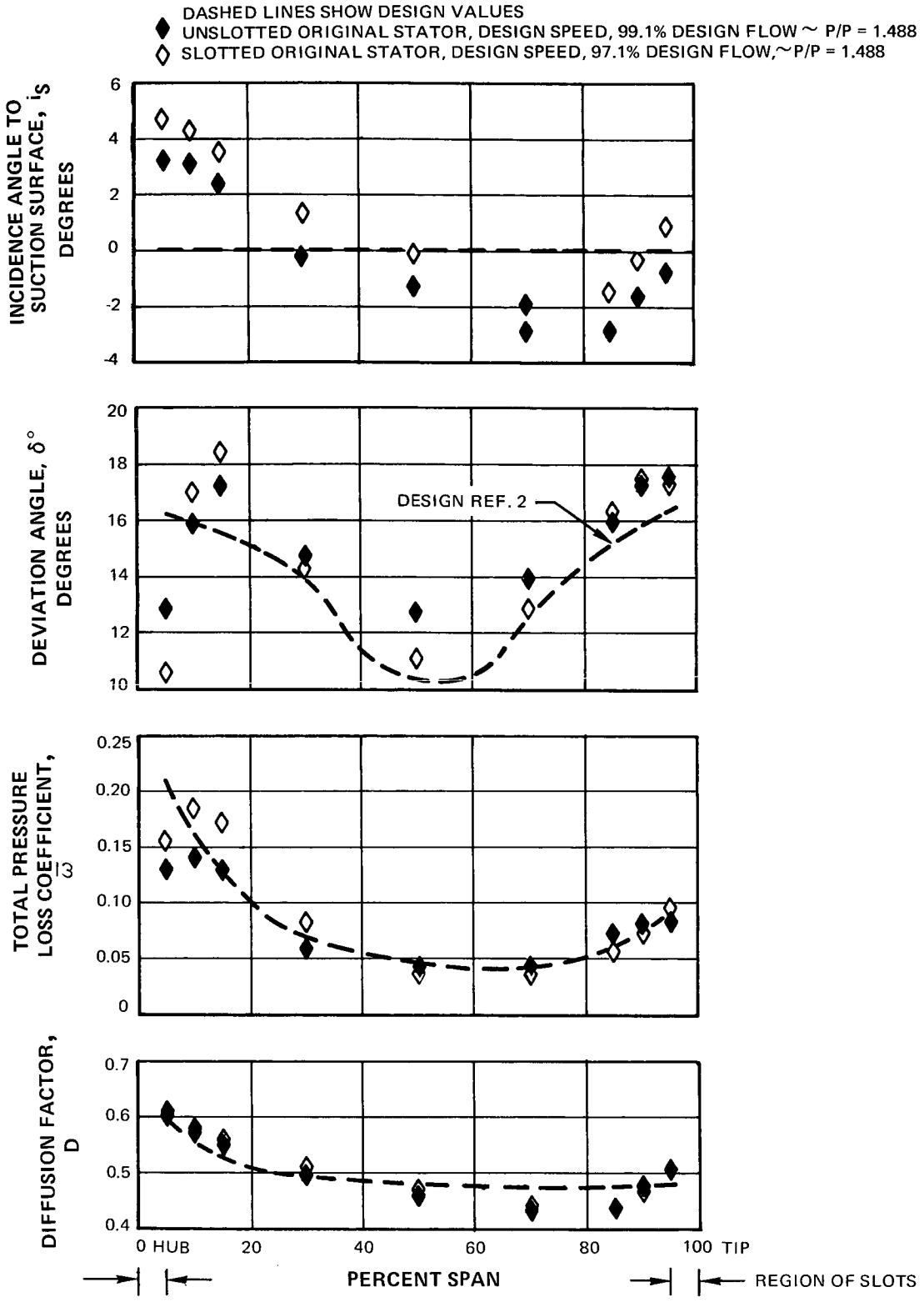

Figure 67 Spanwise Distribution of Original Stator Slotted and Unslotted (Both With Suction) Performance Parameters Near the Operating Line Compared to Original-Design Estimate

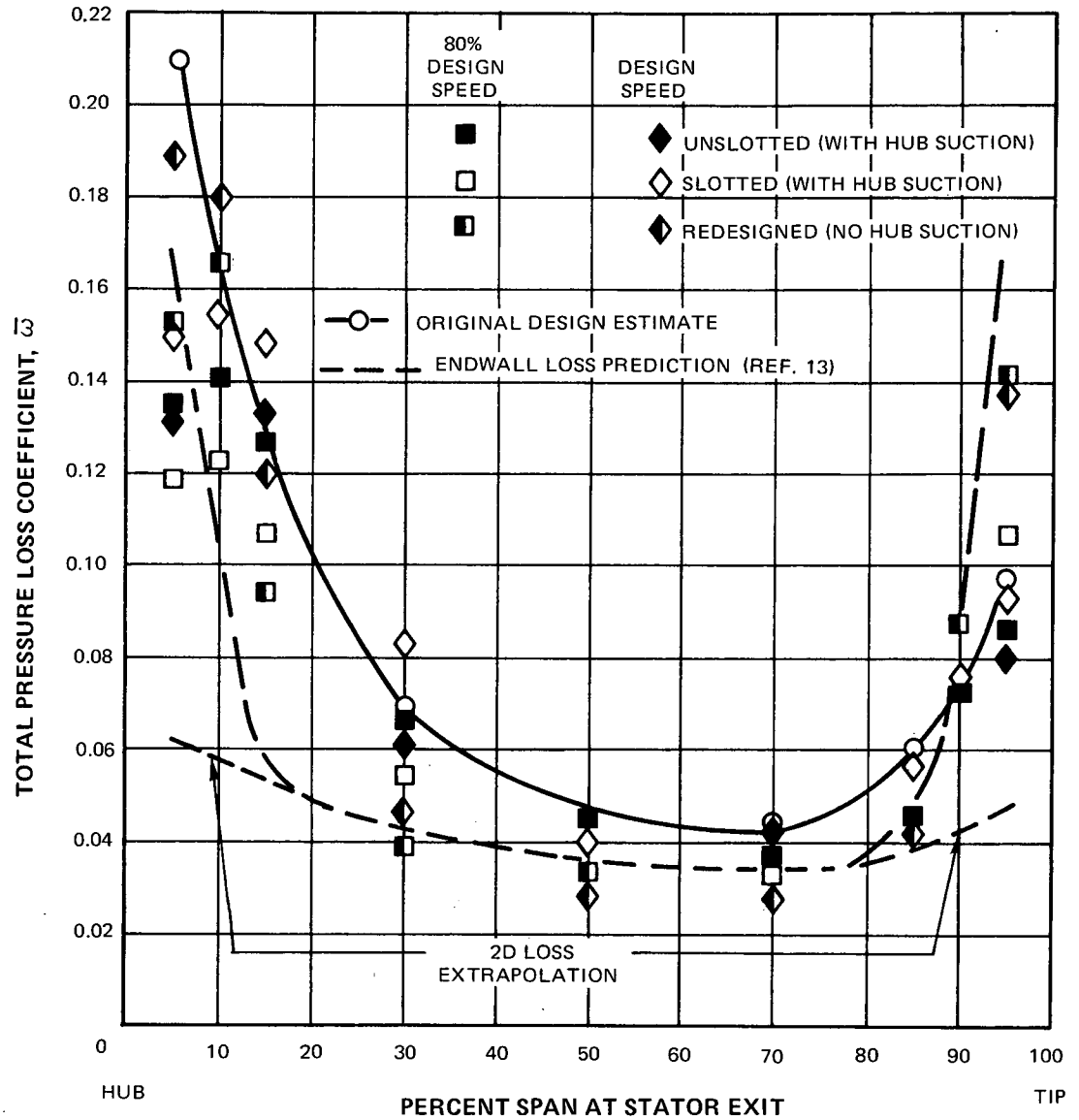

Figure 68 Spanwise Distribution of Stator Loss Coefficient Near the Operating Line Compared to Design Estimates and Endwall Loss Predictions

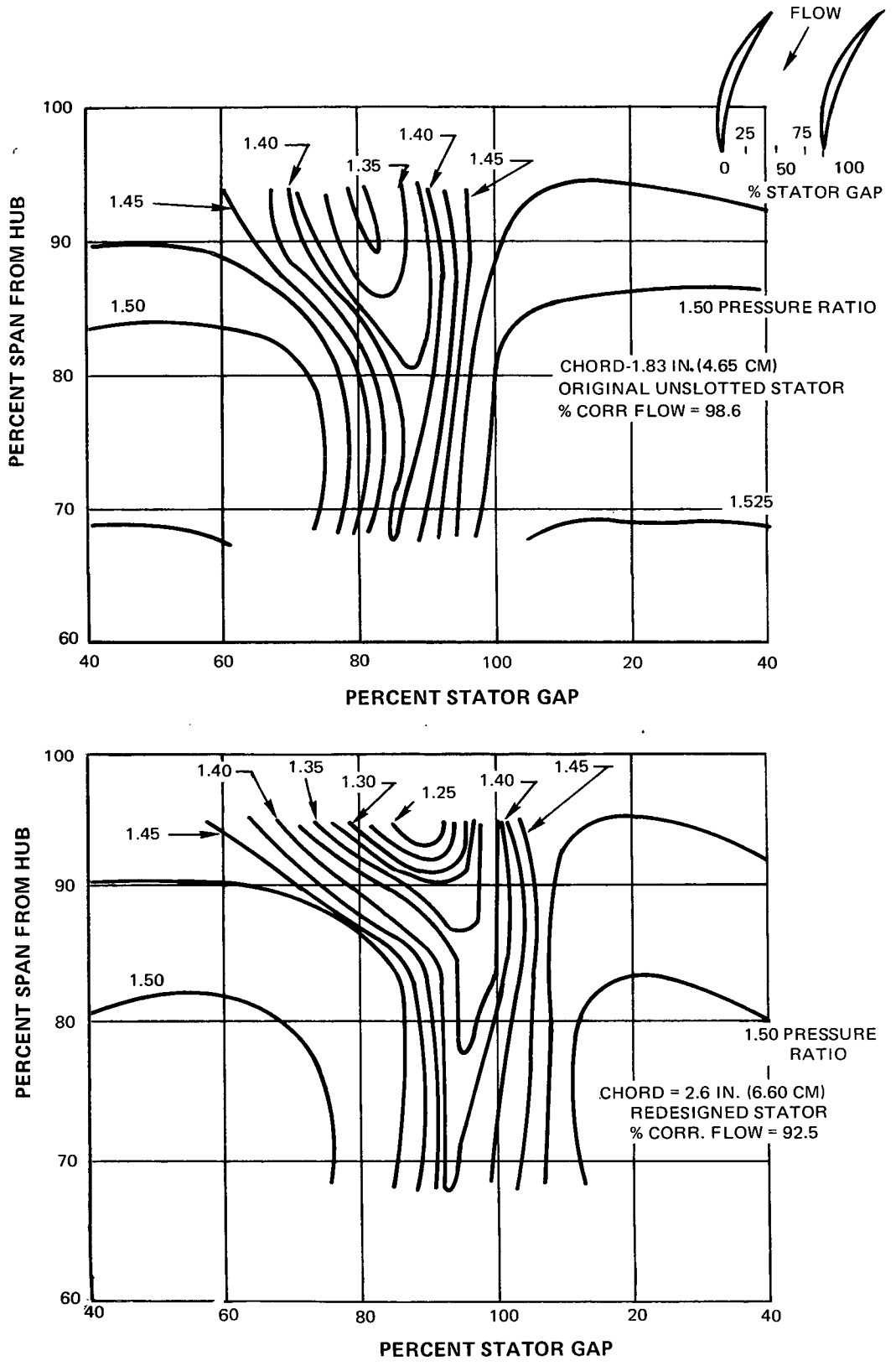

Figure 69 Stator-Exit Total-Pressure Contours at Outer Case for Redesigned and Original Stators at Design Speed

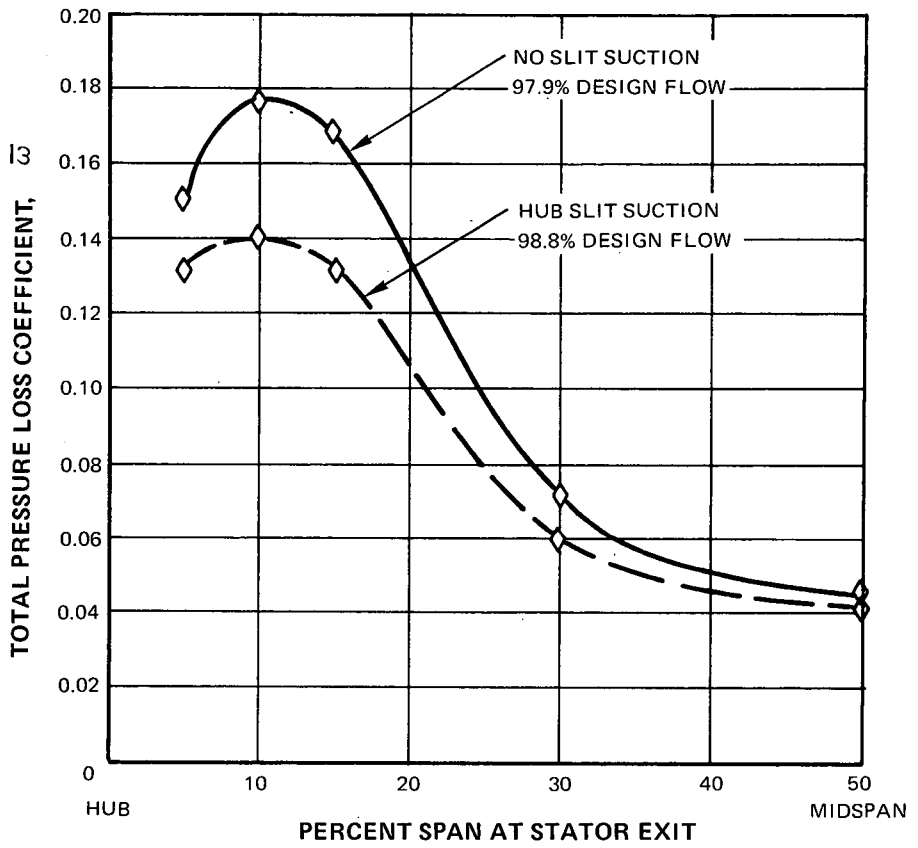

Figure 70 Comparison of Stator Hub Losses Showing Effect of Hub Slit Suction on Original-Stator Design

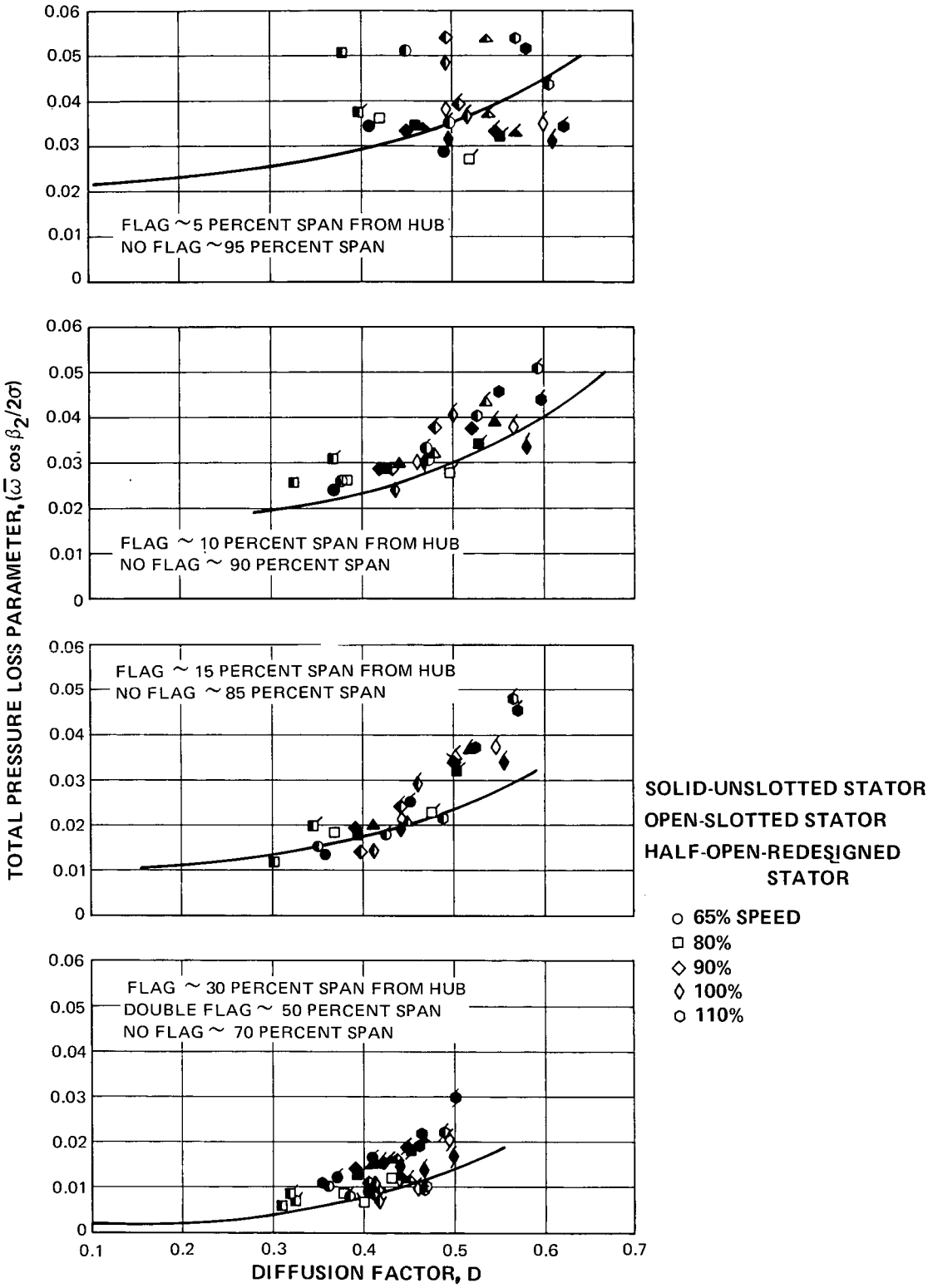

Figure 71 Stator Total Pressure Loss Parameter vs Diffusion Factor

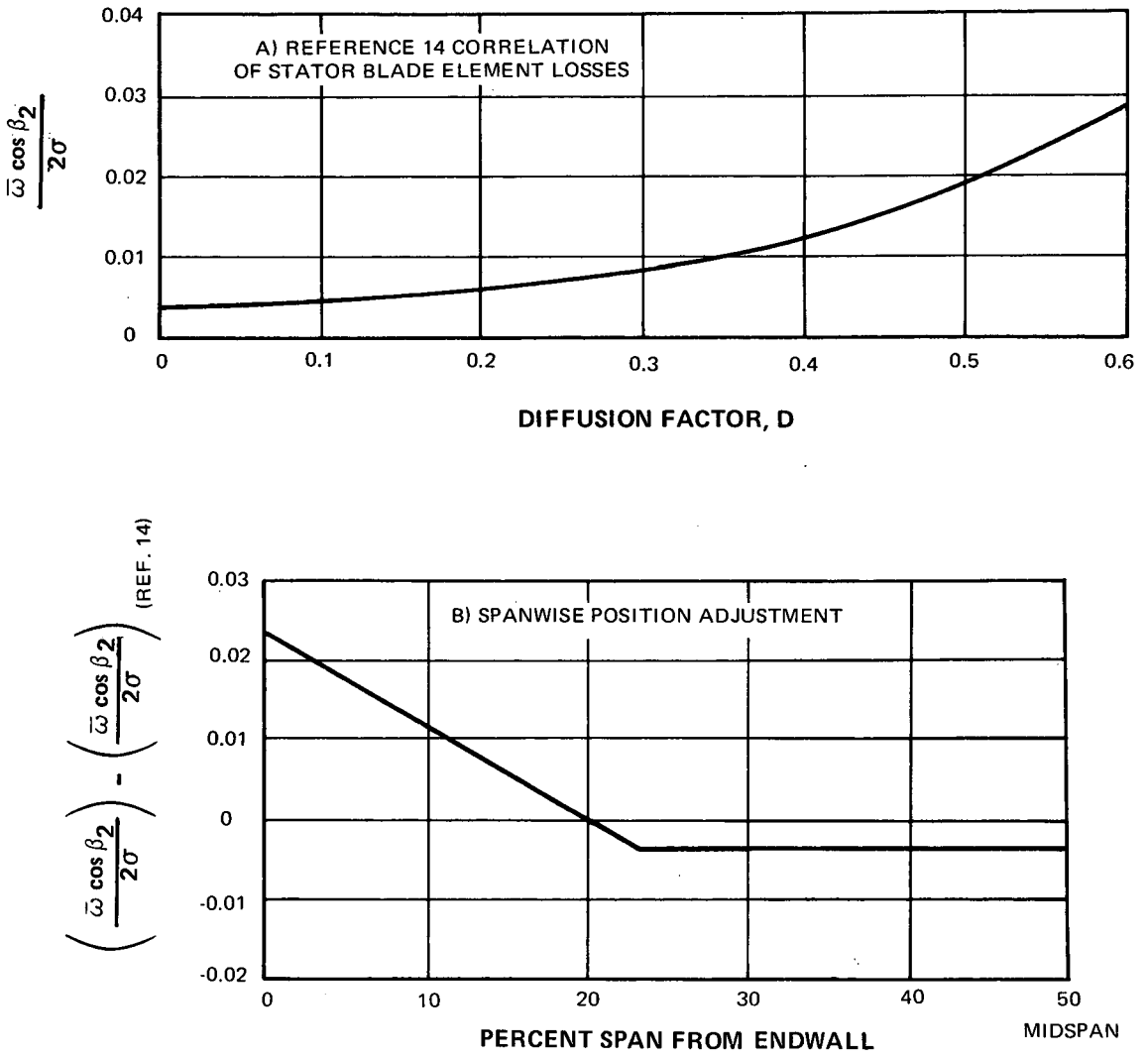

Figure 72 Correlation of Stator Loss Parameter vs Diffusion Factor Showing Spanwise Position Effect

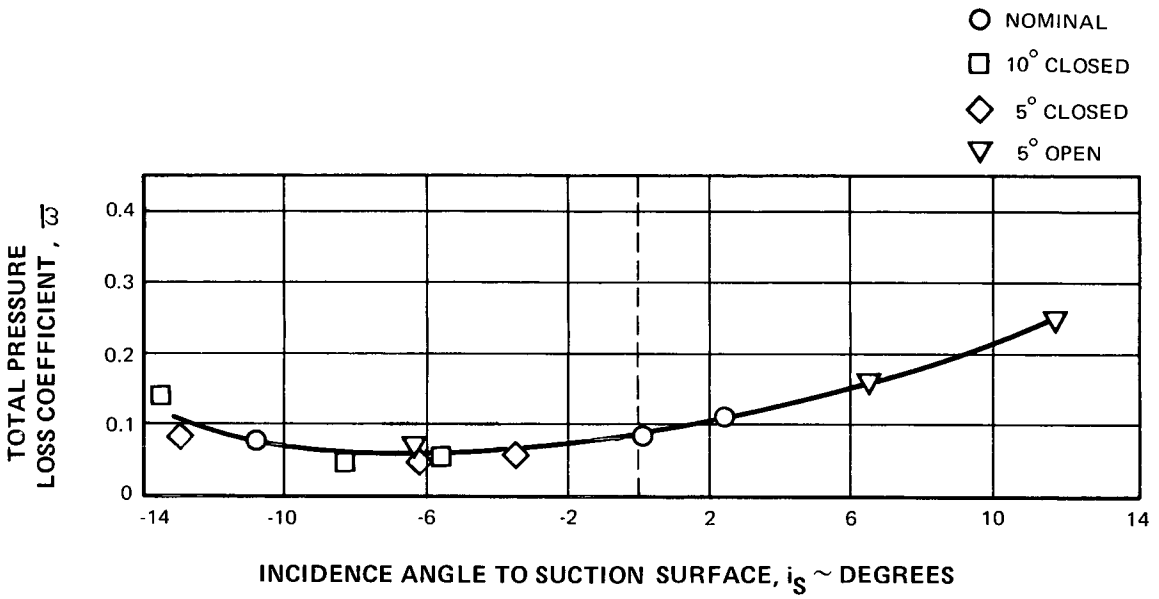

Figure 73 Redesigned Stator Blade Element Losses vs Incidence Angle for Various Stator Setting Angles at 90% Span from Hub

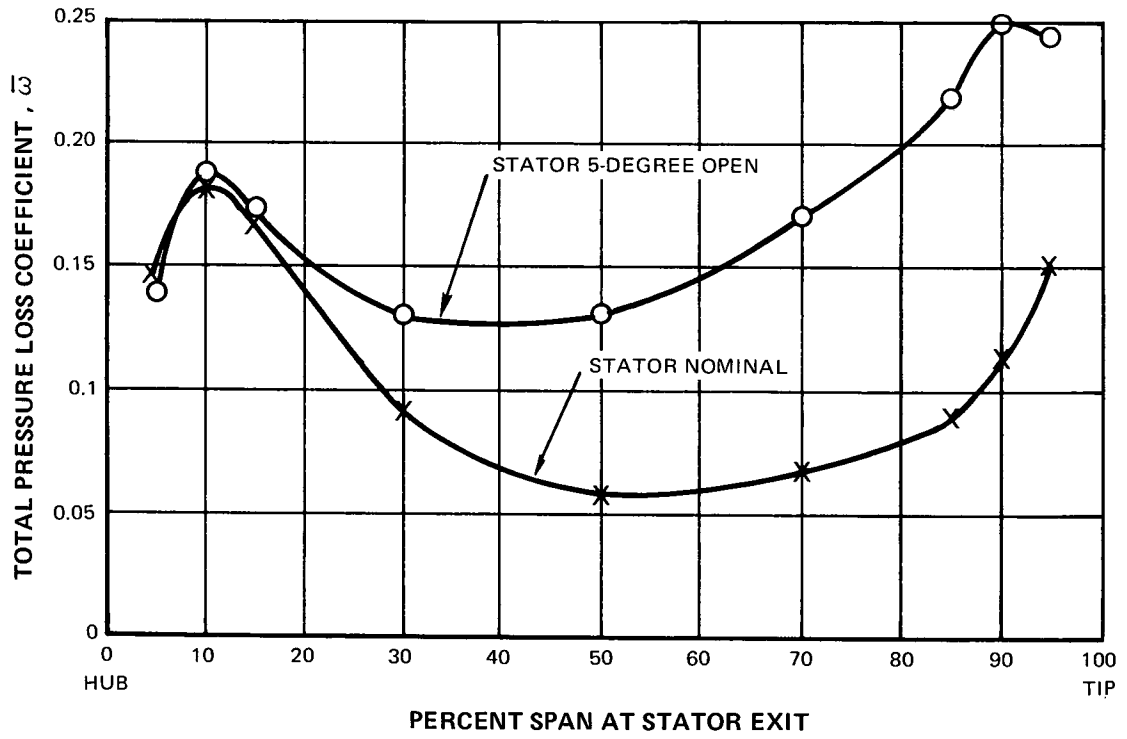

Figure 74 Effect of Stator Setting on Spanwise Loss Distribution Near Stall

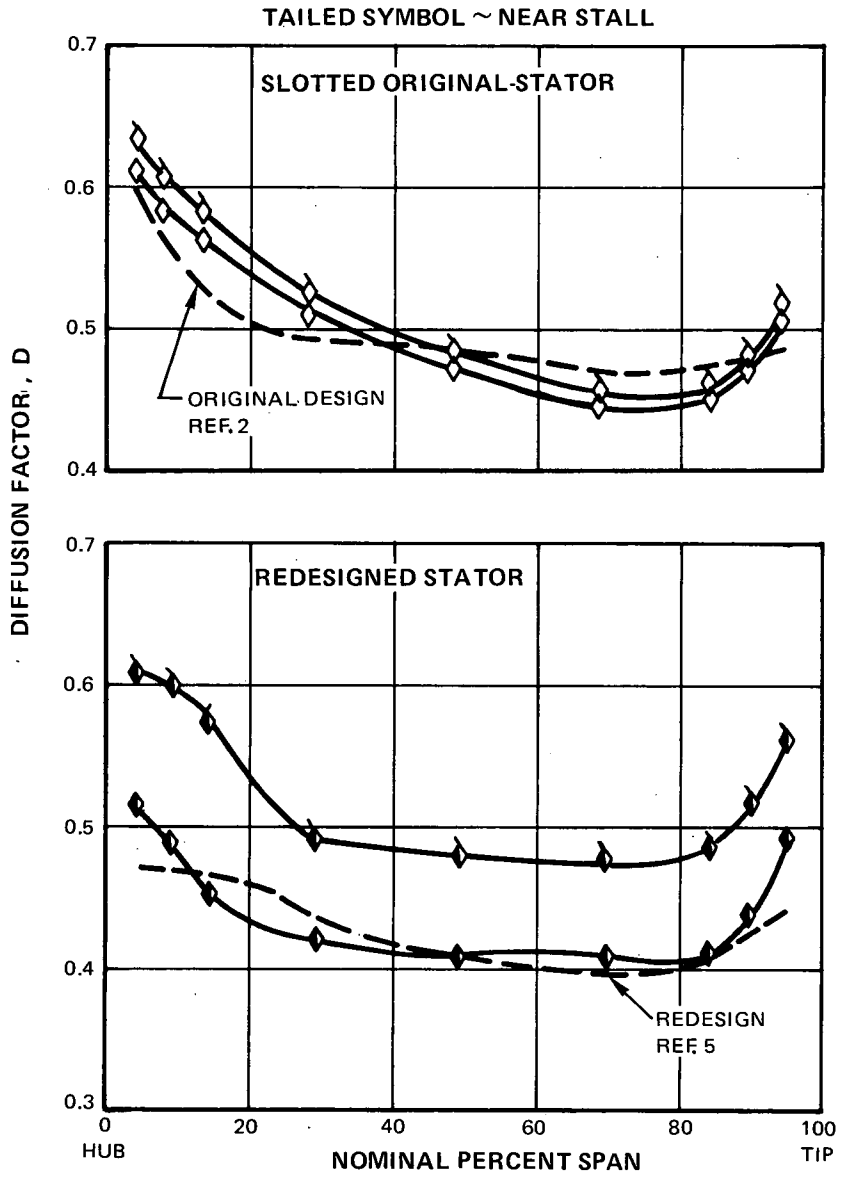

Figure 75 Spanwise Profiles of the Slotted Original-Stator and Redesigned Stator Loadings Near the Operating Line and Near Stall at Design Speed

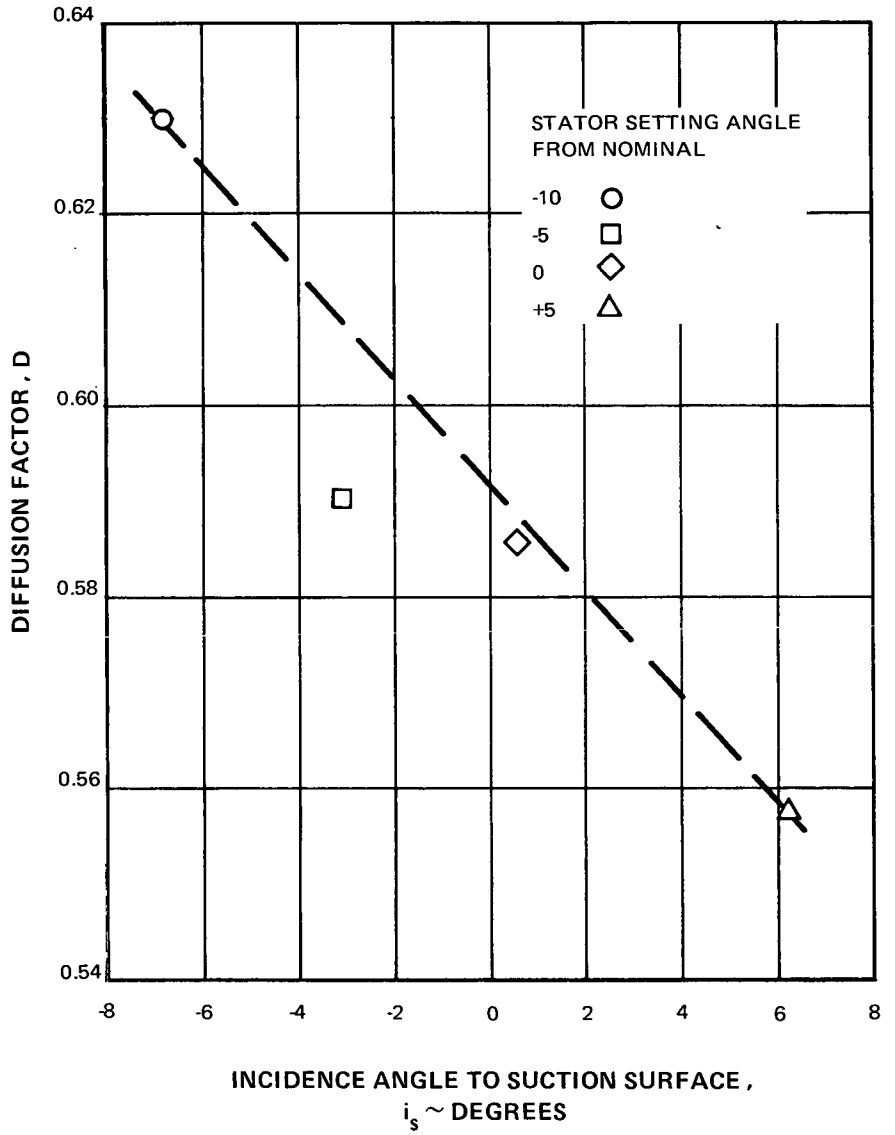

Figure 76 Stator Loading vs Incidence Angle to Suction Surface at 10% Span from Hub for Near-Stall Design-Speed Data Points With Different Stator-Setting-Angles

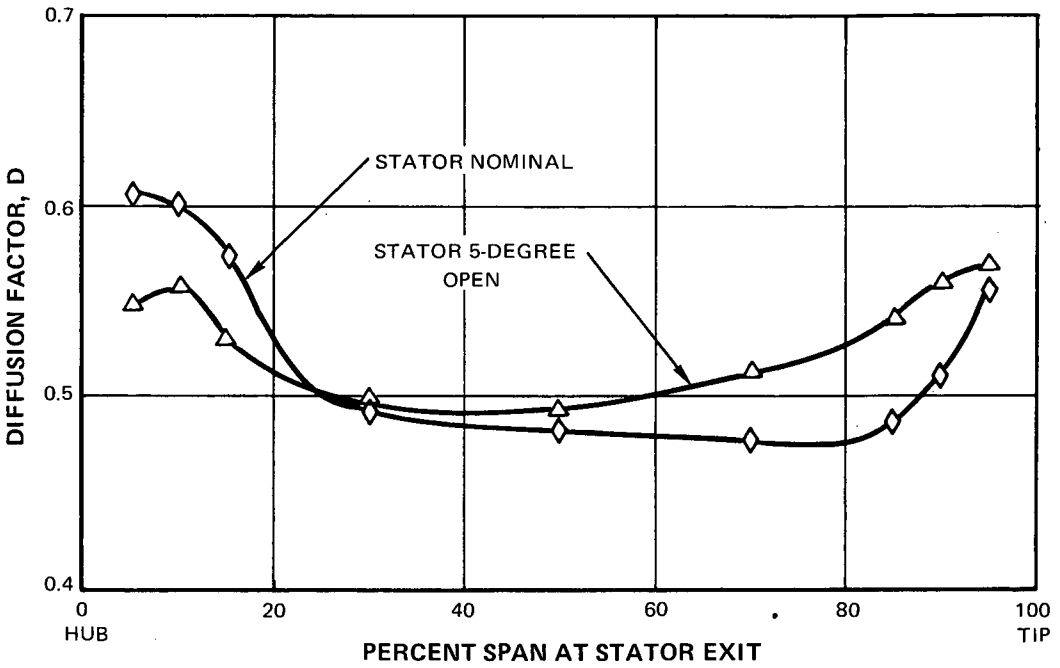

Figure 77 Effect of Stator Setting Angle on Spanwise Loading Distribution Near-Stall at Design Speed

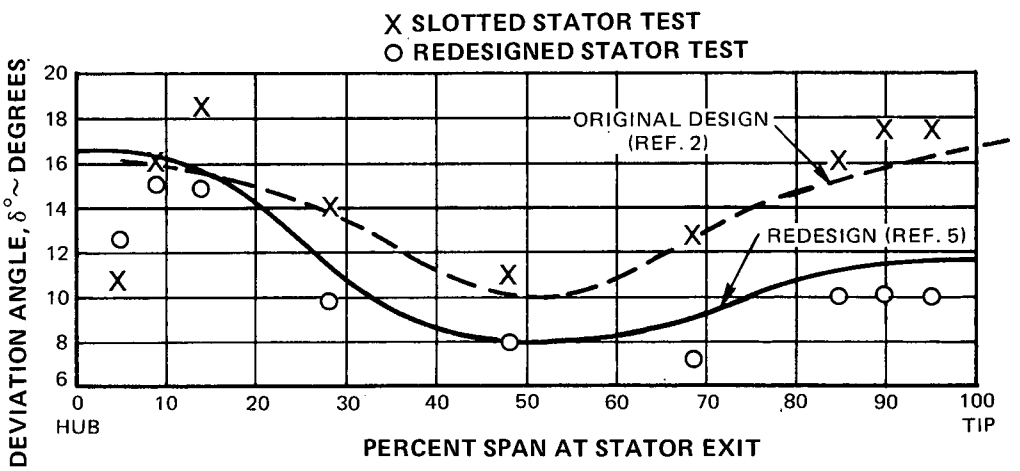

Figure 78 Stator Deviation Angle at Minimum Loss Incidence Angle

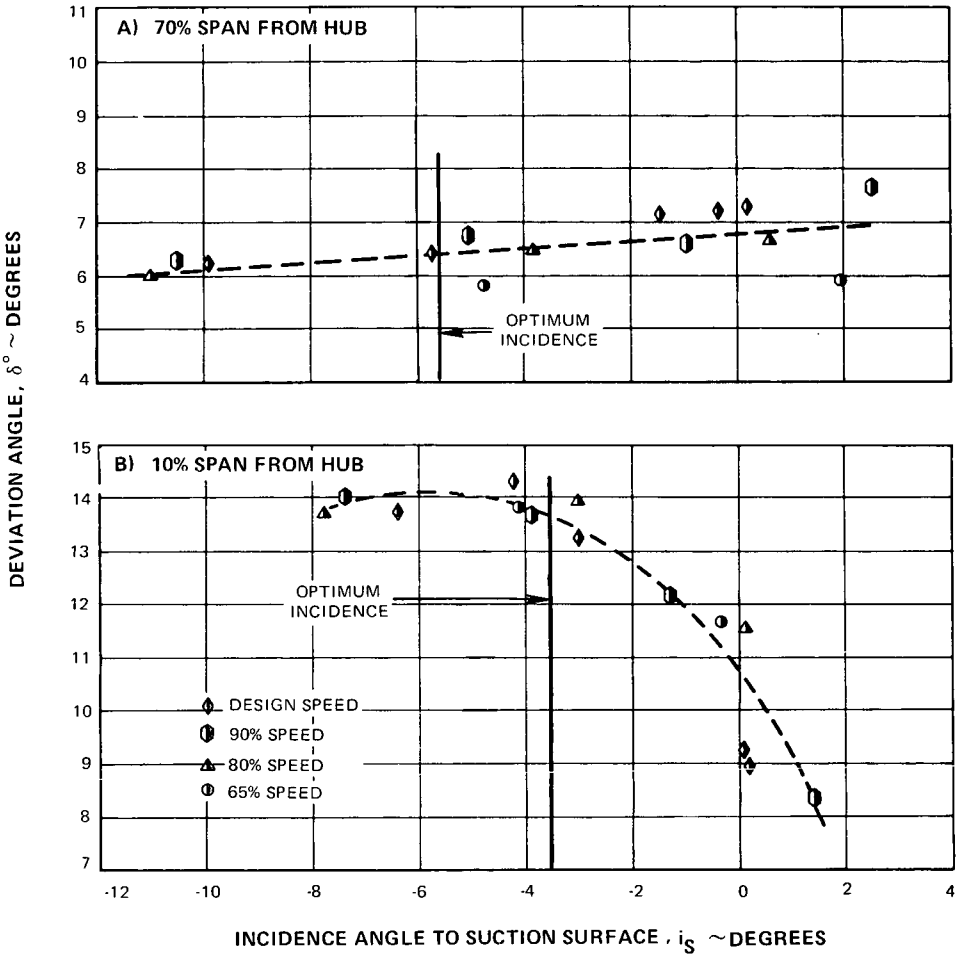

Figure 79 Redesigned Stator Deviation Angle vs Incidence Angle

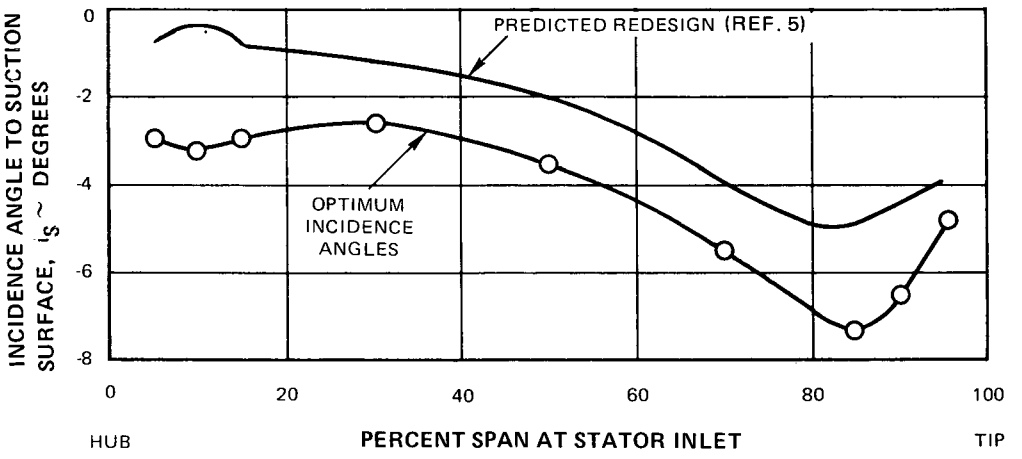

Figure 80 Stator Optimum Incidence Angles for Redesigned Stator

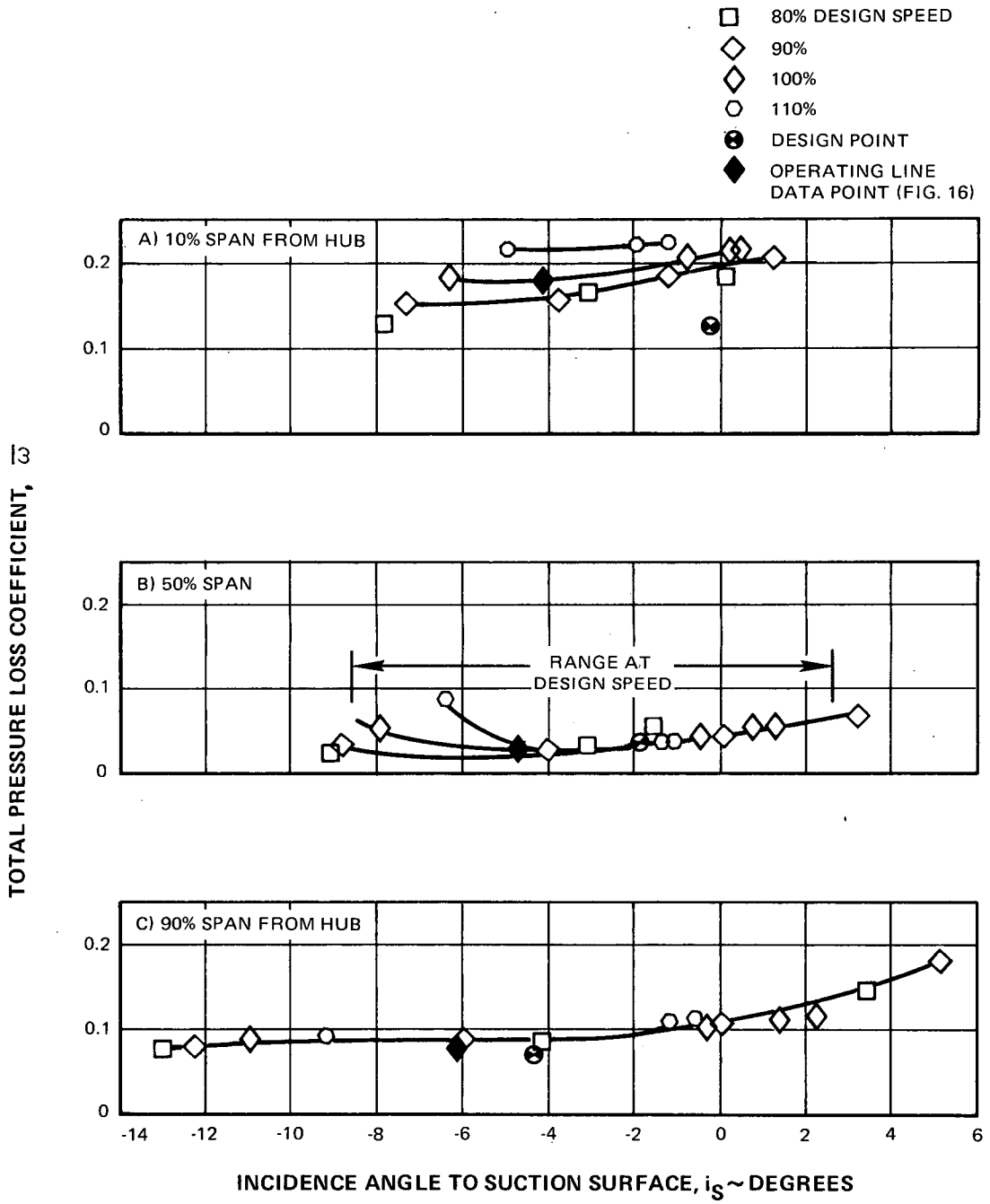

Figure 81 Redesigned-Stator Loss Coefficient vs Incidence to the Suction Surface at 10, 50, and 90% of Span

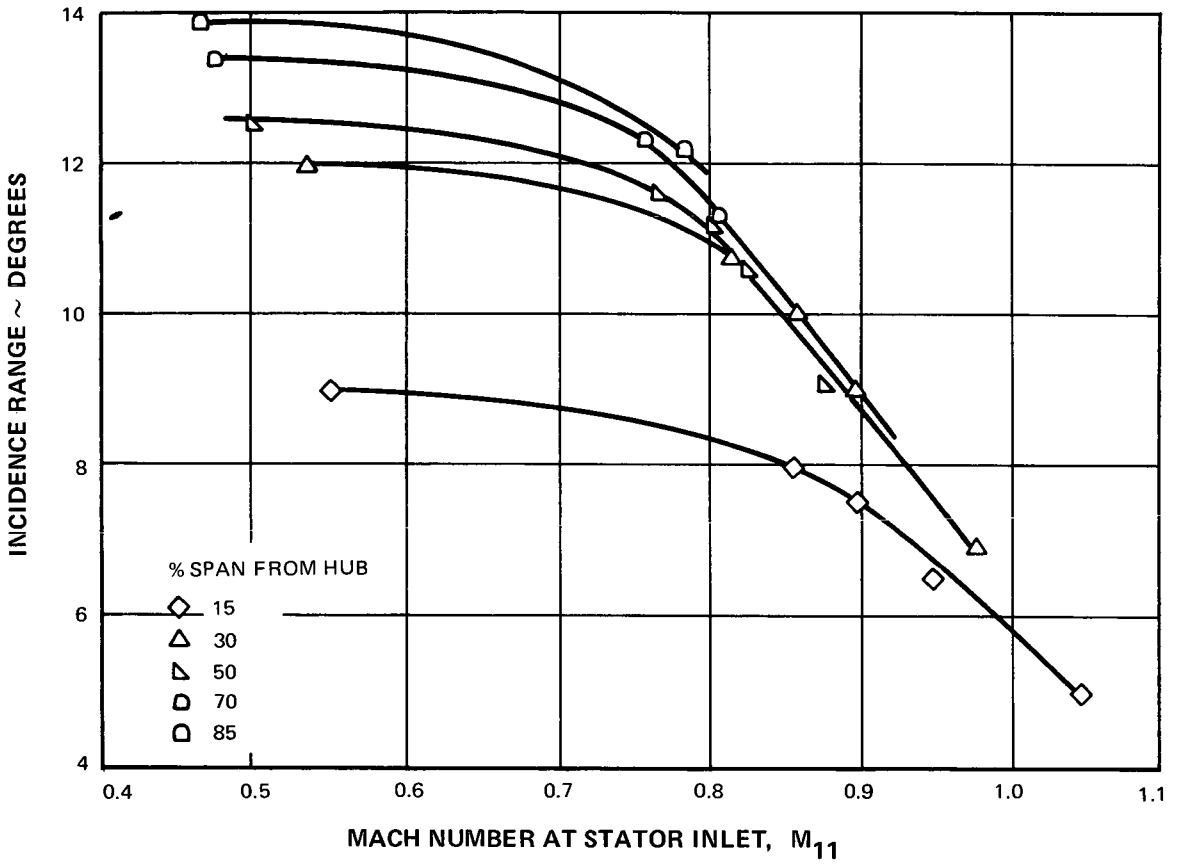

Figure 82 Incidence Range of Redesigned Stator-Blade Elements vs Inlet Mach Number

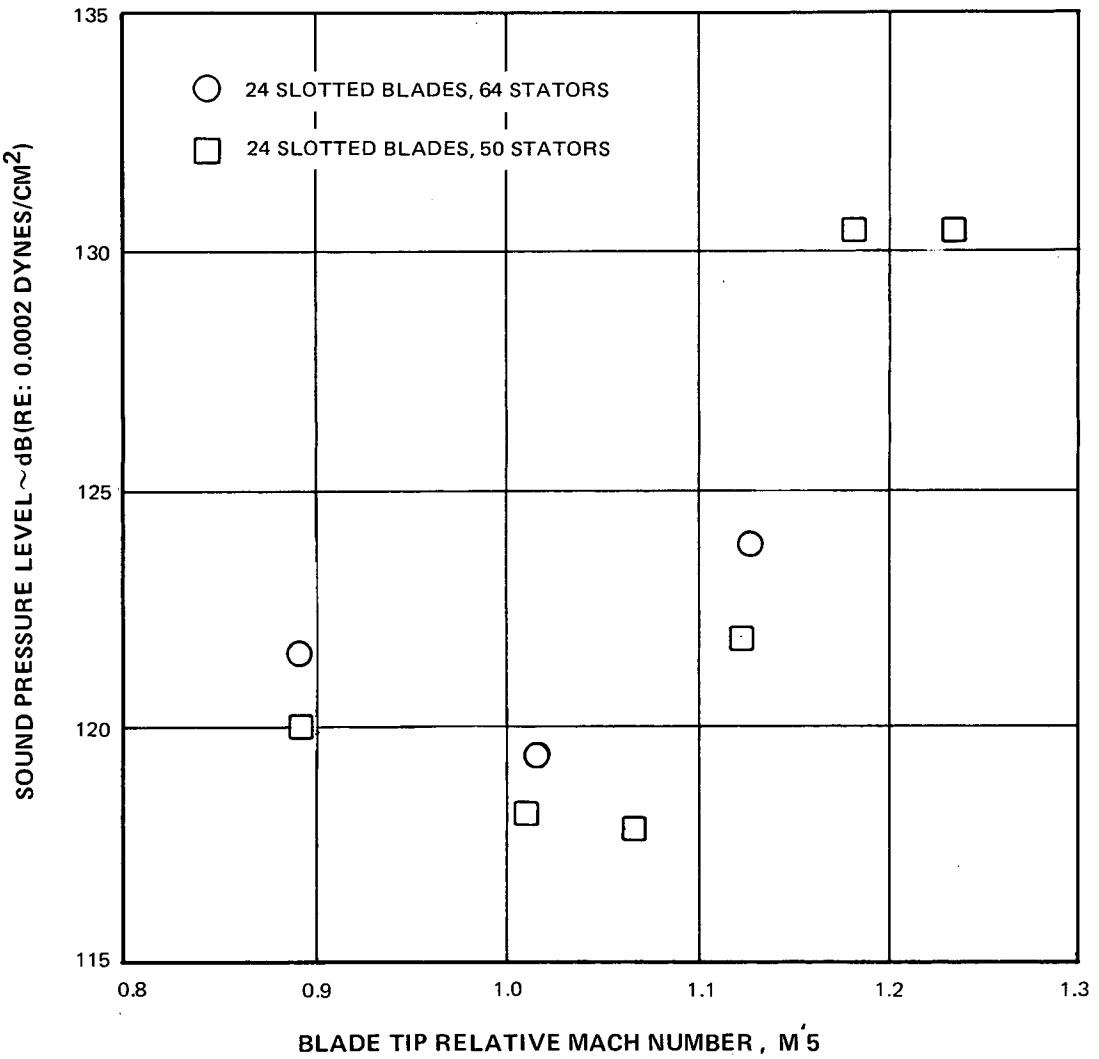

Figure 83 Comparison of Blade-Passing-Frequency Inlet Noise Level for the Sixty-Four and Fifty Vane Stator at Wide Open Throttle

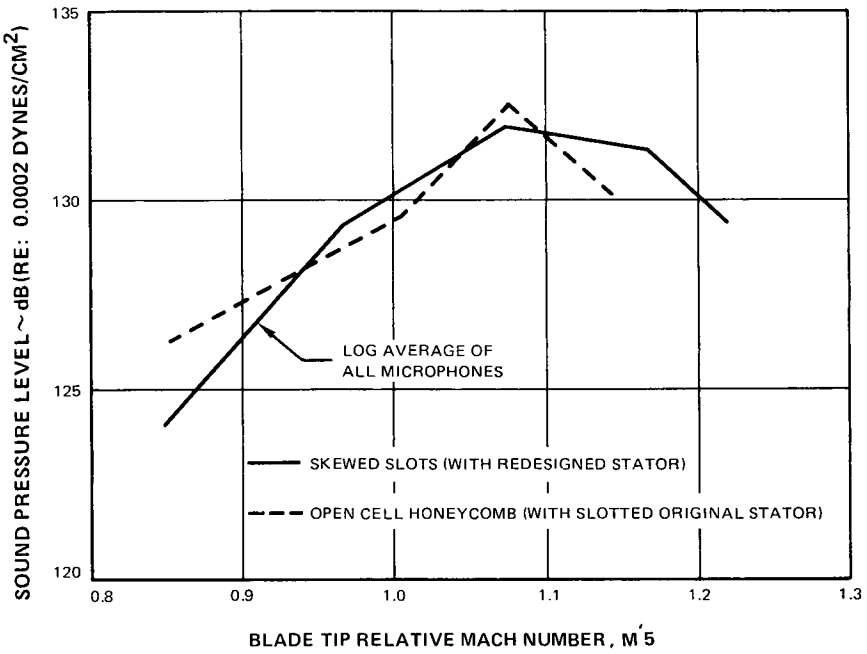

Figure 84 Time-Averaged Blade-Passing-Frequency Inlet Noise for Fan With Rotor Tip Casing Treatment, Nominal Stator at Part Throttle

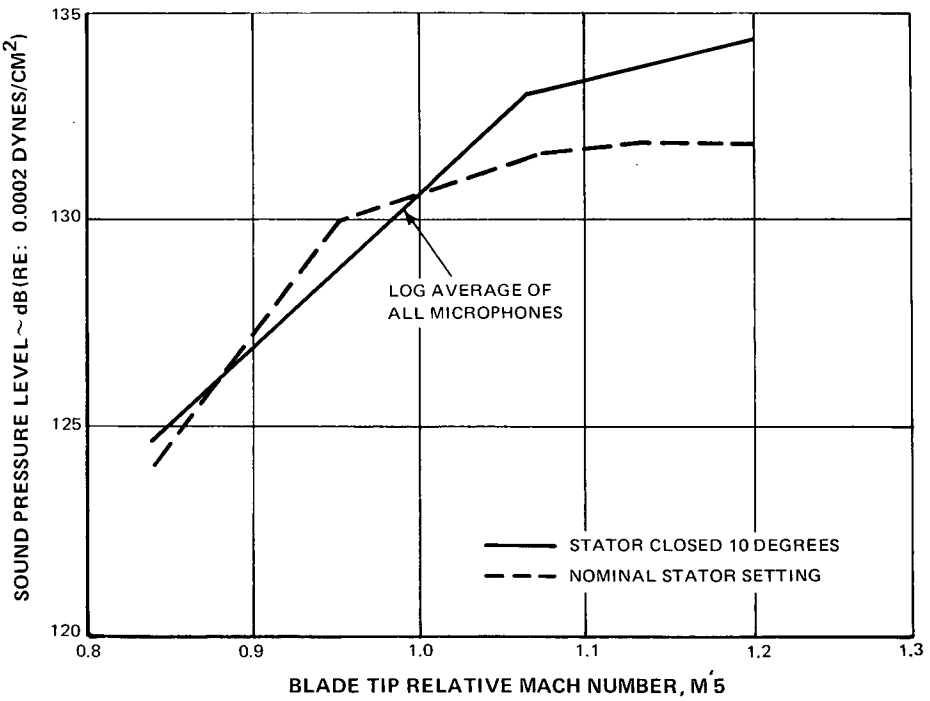

Figure 85 Effect of Stator Angle on Time-Averaged Blade-Passing-Frequency Inlet Noise, Redesigned Stator at Part Throttle

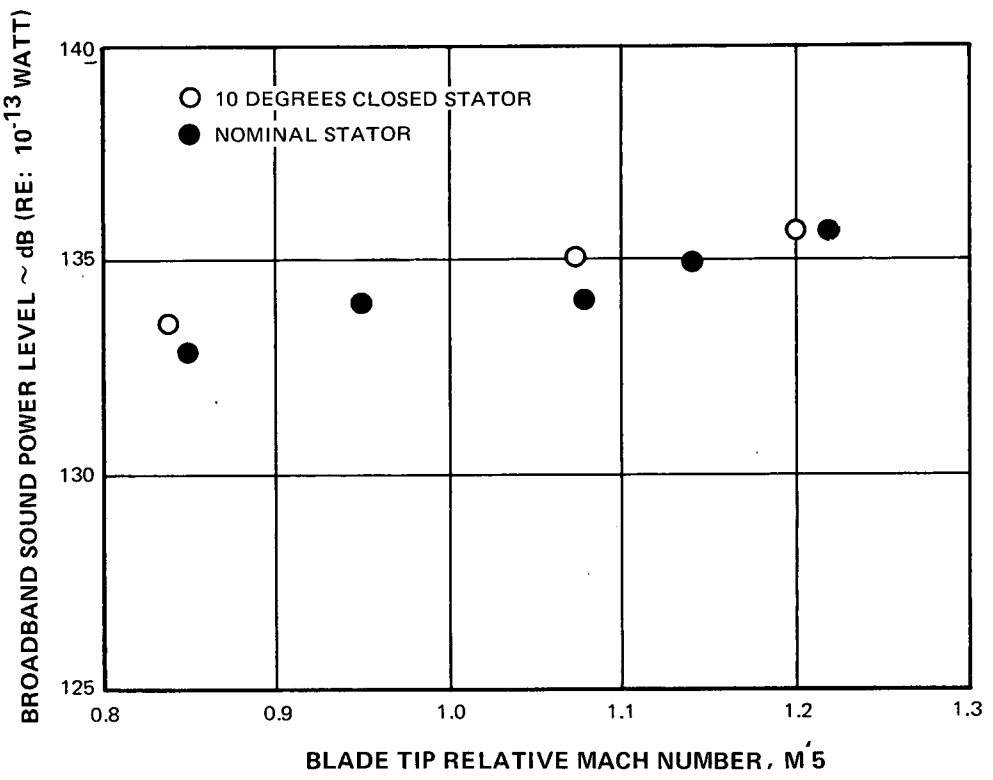

Figure 86 Total Inlet Broadband Sound Power Level, Redesigned Stator at Part Throttle

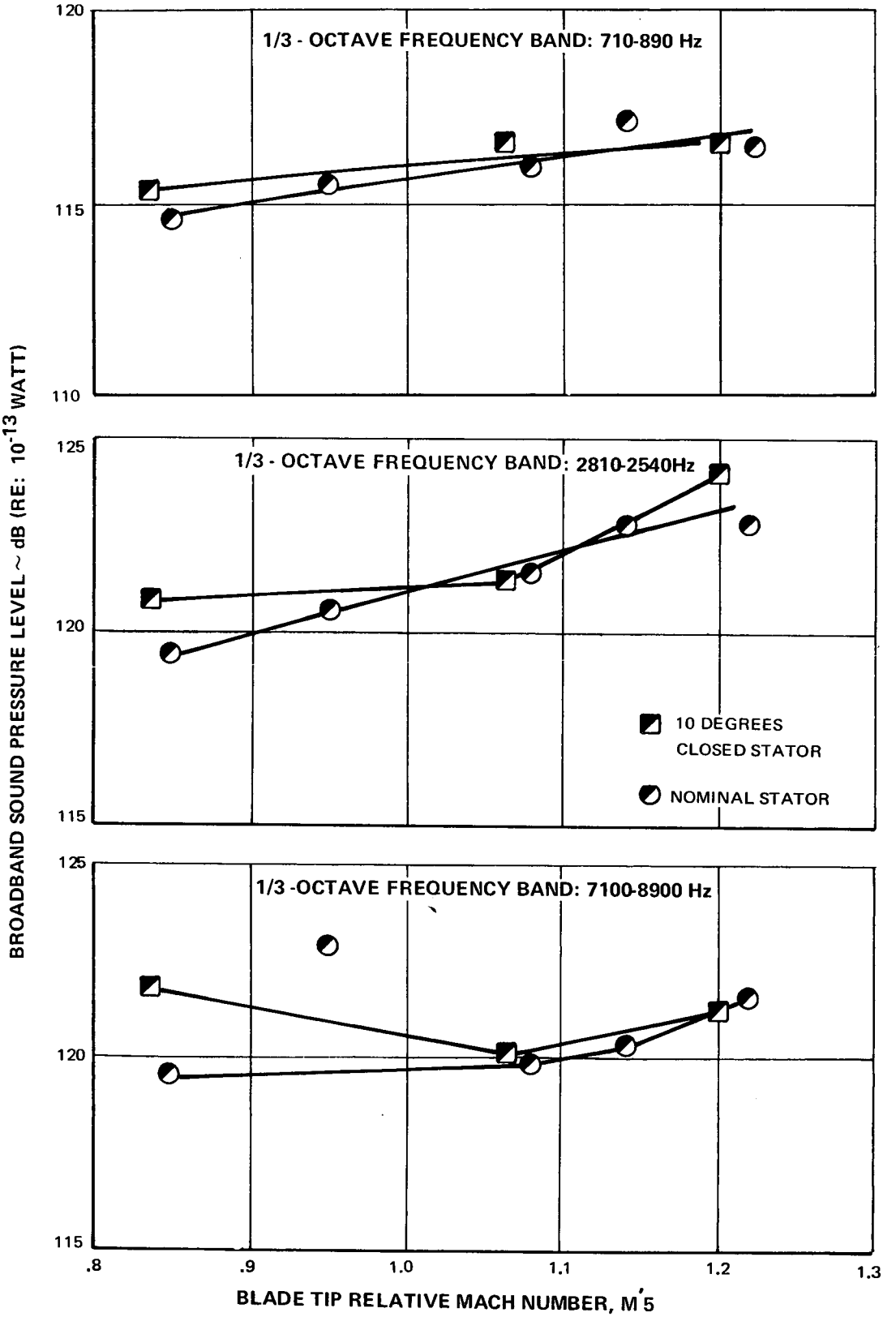

Figure 87 Broadband Sound Pressure Levels in One-Third Octave Bands at Fan Inlet With Nominal and Ten-Degree Closed Settings, Redesigned Stator at Part Throttle

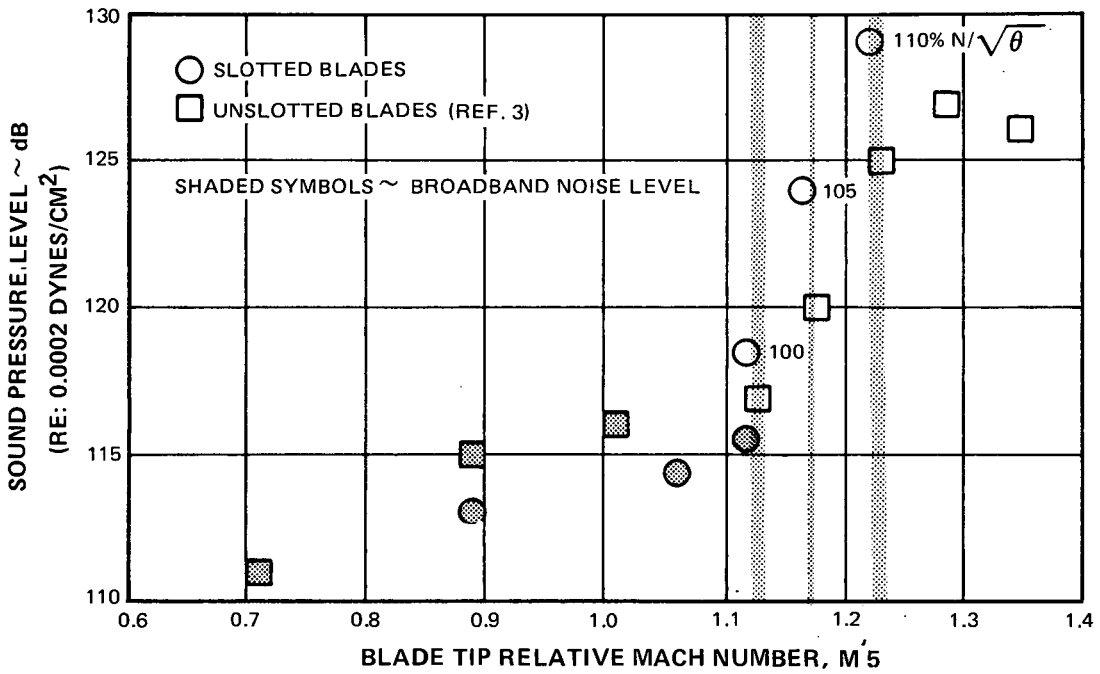

Figure 88 Effects of Slots on Inlet Supersonic Fan-Noise

105% DESIGN SPEED

103.6% DESIGN FLOW

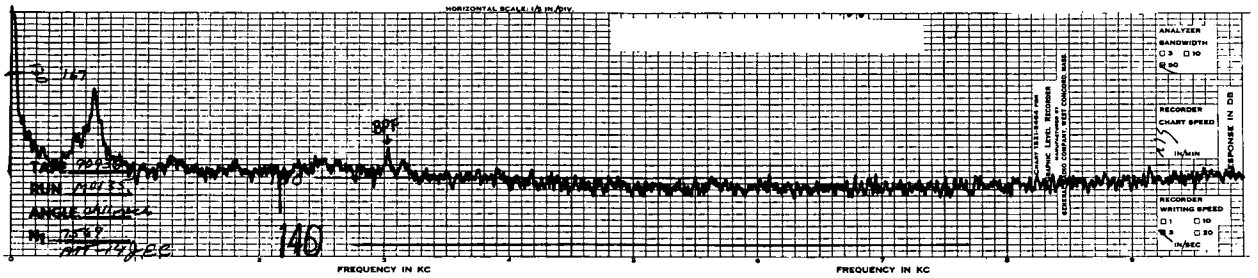

100% DESIGN SPEED

100:2% DESIGN FLOW

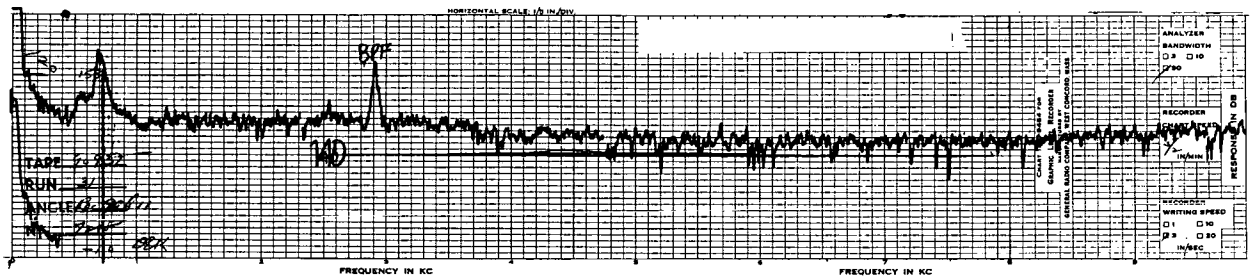

90% DESIGN SPEED

94.7% DESIGN FLOW

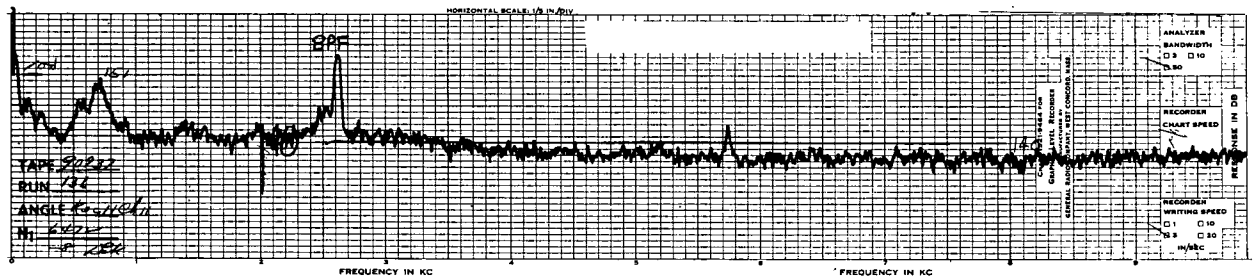

NOTE: REFERENCE SOUND PRESSURE LEVEL AT
140 dB RE: 0.0002 DYNES/CM^2

Figure 89 Fan Discharge Noise Spectra, Wide Open Throttle, Typical of All Configurations Tested With Nominal Stator Setting Angle

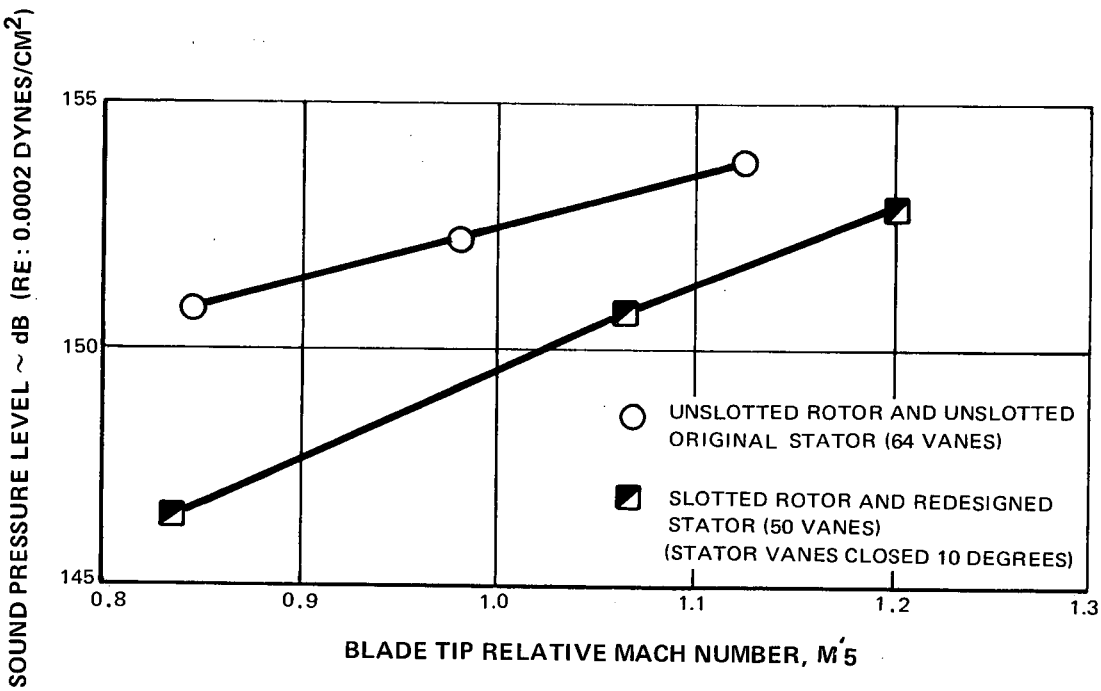

Figure 90 Time-Averaged Blade-Passing-Frequency Noise Downstream of Fan for Two Fan-Configurations at Part Throttle

APPENDIX 1

NOMENCLATURE

A. Symbols:

a	–	distance to maximum camber point from leading edge
A	–	area
A*	–	critical area where M = 1
C	–	chord length on flow surface
D	–	diffusion factor
dB	–	decibel
g_c	–	conversion factor, 32.17 lb_m ft/lb sec^2
i_s	–	incidence angle, angle between inlet air direction and line tangent to blade suction surface at leading edge, degrees
J	–	conversion factor, 778.26 ft lb = 1 BTU
M	–	Mach number
N	–	rotor speed, rpm
P	–	total pressure
p	–	static pressure
R	–	gas constant for air, ft lb/lb_m °R
r	–	radius
ΔS	–	entropy increase
T	–	total temperature
U	–	rotor speed
V	–	air velocity
V_r	–	radial air velocity
V_z	–	axial air velocity
V_m	–	meridional air velocity, $(V_r^2 + V_z^2)^{1/2}$
V_θ	–	tangential component of air velocity $(V^2 - V_m^2)^{1/2}$
W	–	weight flow
α	–	Conical surface angle approximating a streamline of revolution as measured from the axial direction, degrees
β_z	–	absolute air angle [$\cot^{-1} (V_z/V_\theta)$], degrees

APPENDIX 1

NOMENCLATURE (Cont'd)

β – absolute air angle $[\cot^{-1}(V_m/V_\theta)]$, degrees

β'_z – relative air angle $[\cot^{-1}(V_z/V'_\theta)]$, degrees

β' – relative air angle $[\cot^{-1}(V_m/V'_\theta)]$, degrees

β^* – metal angle on conical surface between tangent to mean camber line and axial direction at leading and trailing edge, degrees

γ – ratio of specific heats for air, 1.4

δ – ratio of inlet total pressure to standard pressure of 2116 lb/ft^2

δ° – deviation angle, angle between exit direction and tangent to blade mean camber line at trailing edge, degrees

ϵ – angle between tangent to streamline projected on meriodional plane and axial direction, degrees

η – efficiency

ϕ – blade camber angle, difference between blade metal angle at leading and trailing edge on conical surface, degrees

θ – ratio of inlet total temperature to standard temperature of 518.7°R (288.8°K)

σ – solidity, ratio of chord to spacing

$\bar{\omega}$ – total pressure loss coefficient

ω – angular velocity of rotor, radians/sec

B. Superscripts:

' – relative to moving blades

* – designates blade metal angle

C. Subscripts:

ad – adiabatic

m – meridional direction (vector sum of axial and radial components)

s – suction surface

tip – at rotor tip diameter

APPENDIX 1

NOMENCLATURE (Cont'd)

z	–	axial direction
0	–	plenum chamber
4	–	instrument plane upstream of rotor
5	–	station at rotor inlet
6	–	station at rotor exit
11	–	station at stator leading edge
12	–	station at stator trailing edge

APPENDIX 1

PERFORMANCE PARAMETER DEFINITIONS

a) Relative total temperature

$$T'_5 = t_5 \left[1 + \frac{\gamma - 1}{2} (M'_5)^2 \right] \qquad \text{(rotor in)}$$

$$T'_6 = T'_5 + \left[\frac{(\omega r_5)^2 - (\omega r_6)^2}{\frac{2\gamma}{\gamma - 1} Rg_c} \right] \qquad \text{(rotor out)}$$

b) Diffusion factor

$$D = 1 - \frac{V'_6}{V'_5} + \frac{r_6 V_{\theta 6} - r_5 V_{\theta 5}}{(r_5 + r_6)\sigma V'_5} \qquad \text{(rotor)}$$

$$D = 1 - \frac{V_{12}}{V_{11}} + \frac{r_{11} V_{\theta\, 11} - r_{12} V_{\theta\, 12}}{(r_{11} + r_{12})\sigma V_{11}} \qquad \text{(stator)}$$

c) Loss coefficient

$$\bar{\omega} = \frac{P'_5 \left[\frac{T'_6}{T'_5} \right]^{\frac{\gamma}{\gamma - 1}} - P'_6}{P'_5 - p_5} \qquad \text{(rotor)}$$

$$\bar{\omega} = \frac{P_{11} - P_{12}}{P_{11} - p_{11}} \qquad \text{(stator)}$$

APPENDIX 1

PERFORMANCE PARAMETER DEFINITIONS (Cont'd)

d) Total-pressure recovery [ref. 15]

$$\text{Recovery} = e^{-(J/R)\,\Delta S} = \frac{P_6/P_5}{(T_6/T_5)^{\gamma/\gamma-1}} \qquad \text{(rotor)}$$

$$e^{-(J/R)\,\Delta S} = P_{12}/P_{11} \qquad \text{(stator)}$$

e) Adiabatic efficiency

$$\eta_{ad} = \frac{\left[\frac{P_6}{P_5}\right]^{\frac{\gamma-1}{\gamma}} - 1}{\left[\frac{T_6}{T_5}\right] - 1} \qquad \text{(rotor)}$$

$$\eta_{ad} = \frac{\left[\frac{P_{12}}{P_5}\right]^{\frac{\gamma-1}{\gamma}} - 1}{\left[\frac{T_{12}}{T_5}\right] - 1} \qquad \text{(stage)}$$

APPENDIX 1

PERFORMANCE PARAMETER DEFINITIONS (Cont'd)

f) Stall margin

$$SM = \left[\left(\frac{\frac{P_{12}}{P_5}}{\frac{W\sqrt{\theta}}{\delta}} \right)_{\text{at stall}} \times \left(\frac{\frac{W\sqrt{\theta}}{\delta}}{\frac{P_{12}}{P_5}} \right)_{\text{at reference point}} - 1 \right] \times 100\%$$

For absolute values of stall margin, the reference is generally an operating point near peak efficiency.

g) Velocity diagram

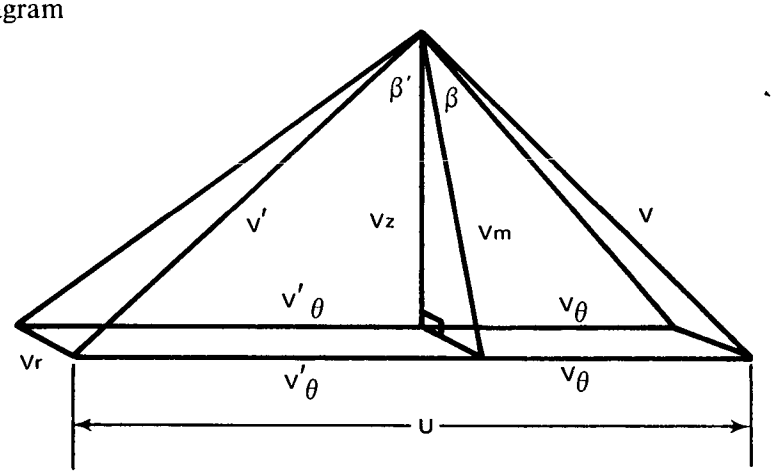

APPENDIX 2

AERODYNAMIC DESIGN SUMMARY – ROTOR INLET

		I.D.										O.D.
Percent Flow		0	10	20	30	40	50	60	70	80	90	100
pressure ratio	-	1.0	1.0	1.0	1.0	1.0	1.0	1.0	1.0	1.0	1.0	1.0
temperature ratio	-	1.0	1.0	1.0	1.0	1.0	1.0	1.0	1.0	1.0	1.0	1.0
M	-	0.561	0.581	0.602	0.615	0.624	0.629	0.632	0.634	0.635	0.636	0.635
M'	-	0.669	0.741	0.806	0.860	0.908	0.950	0.990	1.027	1.061	1.095	1.127
M_m	-	0.561	0.581	0.602	0.615	0.624	0.629	0.632	0.634	0.635	0.636	0.635
M_z	-	0.531	0.564	0.592	0.609	0.620	0.627	0.631	0.634	0.635	0.636	0.635
β	degrees	0	0	0	0	0	0	0	0	0	0	0
β'	degrees	32.98	38.32	41.69	44.36	46.61	48.56	50.29	51.84	53.23	54.51	55.67
β_z	degrees	0	0	0	0	0	0	0	0	0	0	0
β'_z	degrees	34.43	39.17	42.16	44.63	46.76	48.65	50.33	51.85	53.24	54.51	55.67
ϵ	degrees	18.76	14.05	10.46	7.88	5.95	4.43	3.19	2.15	1.25	0.49	-0.10
					ENGLISH UNITS							
diameter	inches	12.217	15.382	17.903	20.058	21.975	23.723	25.341	26.857	28.289	29.651	30.953
V	ft/sec	575.5	628.3	649.0	662.2	670.7	676.1	679.5	581.5	682.4	682.6	682.4
V'	ft/sec	607.7	800.9	869.1	926.2	976.3	1021.6	1063.5	1102.8	1140.1	1175.8	1210.1
V_Z	ft/sec	724.5	609.5	638.2	655.9	677.1	674.1	678.5	681.0	682.3	682.6	682.4
V_m	ft/sec	607.7	628.3	649.0	662.2	670.7	676.1	679.5	681.5	682.4	682.6	682.4
V_θ	ft/sec	0	0	0	0	0	0	0	0	0	0	0
V'_θ	ft/sec	-394.4	-496.6	-597.9	-647.6	-709.5	-765.9	-818.1	-867.1	-913.3	-957.3	-999.3
U	ft/sec	394.4	496.6	578.0	647.7	709.5	765.9	818.2	867.1	913.3	951.3	999.3
					SI UNITS							
diameter	meters	0.3103	0.3907	0.4547	0.5095	0.5582	0.6026	0.6437	0.6822	0.7185	0.7531	0.7862
V	m/sec	185.2	191.5	197.8	201.8	204.4	206.1	207.1	207.7	208.0	208.1	207.9
V'	m/sec	220.8	244.1	264.9	282.3	297.6	311.4	324.2	336.1	347.5	358.4	368.8
V_Z	m/sec	175.4	185.8	194.5	199.9	203.3	205.5	206.8	207.6	207.9	208.1	207.9
V_m	m/sec	185.2	191.5	197.8	201.8	204.4	206.1	207.1	207.7	208.0	208.1	207.9
V_θ	m/sec	0	0	0	0	0	0	0	0	0	0	0
V'_θ	m/sec	-120.2	-151.4	-176.2	-197.4	-216.2	-233.4	-249.4	-264.3	-278.4	-291.8	-304.6
U	m/sec	120.2	151.4	176.2	197.4	216.2	233.4	249.4	264.3	278.4	291.8	304.6

Calculations based on an inlet pressure of 2116 psf and an inlet temperature of 518.7 R

APPENDIX 2 (Cont'd)

AERODYNAMIC DESIGN SUMMARY – ROTOR EXIT

		I.D.										O.D.
Percent Flow		0	10	20	30	40	50	60	70	80	90	100
pressure ratio	-	1.540	1.540	1.540	1.540	1.540	1.540	1.540	1.540	1.540	1.540	1.540
temperature ratio	-	1.141	1.134	1.135	1.136	1.138	1.140	1.141	1.143	1.146	1.150	1.157
M	-	0.912	0.875	0.826	0.778	0.742	0.714	0.692	0.674	0.659	0.646	0.634
M'	-	0.559	0.595	0.577	0.558	0.557	0.565	0.581	0.601	0.622	0.639	0.644
M_m	-	0.431	0.579	0.576	0.554	0.537	0.524	0.514	0.506	0.499	0.488	0.471
M_z	-	0.420	0.573	0.573	0.552	0.536	0.524	0.514	0.506	0.498	0.488	0.471
β	degrees	61.82	48.62	45.81	44.65	43.89	42.74	41.98	41.30	40.81	40.89	42.03
β'	degrees	-39.60	-13.41	-2.23	7.01	15.15	21.98	27.76	32.63	36.72	40.13	43.04
β_z	degrees	62.39	48.89	45.97	44.75	43.65	42.78	41.99	41.31	40.82	40.89	42.03
β'_z	degrees	-40.28	-13.53	-2.24	7.04	15.18	22.11	27.78	32.64	36.72	40.12	43.04
ϵ	degrees	12.52	7.89	6.02	4.78	3.76	2.90	2.15	1.48	0.89	0.38	-0.05
					ENGLISH UNITS							
diameter	inches	15.308	17.787	19.699	21.411	22.994	24.477	25.878	27.211	28.486	29.716	30.922
V	ft/sec	1006.9	968.8	921.9	874.7	838.3	810.4	788.1	769.9	755.0	742.7	732.3
V'	ft/sec	617.0	658.4	643.1	626.9	629.1	641.8	662.1	686.9	712.9	734.3	744.3
V_z	ft/sec	464.1	634.4	639.1	620.1	605.9	594.4	585.5	578.3	571.3	561.5	543.9
V_m	ft/sec	475.4	640.5	642.6	622.3	607.2	595.2	585.9	578.5	571.4	561.5	543.9
V_θ	ft/sec	887.6	726.9	661.0	614.7	578.0	549.9	527.1	508.1	493.5	486.1	490.3
V'_θ	ft/sec	393.3	152.7	25.0	-76.6	-164.4	-240.3	-308.4	-370.4	-426.2	-473.3	-508.0
U	ft/sec	494.2	574.3	635.9	691.3	742.4	790.2	835.5	878.5	919.7	959.4	998.3
					SI UNITS							
diameter	meters	0.3888	0.4518	0.5084	0.5438	0.5840	0.6217	0.6573	0.6912	0.7235	0.7548	0.7854
V	m/sec	306.9	295.3	280.9	266.6	255.5	247.9	240.2	234.7	230.1	226.4	223.2
V'	m/sec	188.1	200.6	196.0	191.1	191.7	195.6	201.8	209.4	217.3	223.8	226.9
V_z	m/sec	141.5	193.4	194.8	189.0	184.7	181.2	178.4	176.3	174.1	171.1	165.8
V_m	m/sec	144.9	195.2	195.9	189.7	185.1	181.4	178.6	176.3	174.2	171.1	165.8
V_θ	m/sec	270.5	221.6	201.5	187.4	176.2	167.6	160.7	154.9	150.4	184.2	149.4
V'_θ	m/sec	119.9	46.5	7.6	-23.3	-50.1	-73.2	-93.9	-112.9	-129.9	-144.3	-154.9
U	m/sec	150.6	175.0	193.9	210.7	226.3	240.9	254.7	267.8	280.3	292.4	304.3

Calculations based on an inlet pressure of 2116 psf and an inlet temperature of 518.7°F

APPENDIX 2 (Cont'd)

AERODYNAMIC DESIGN SUMMARY – ORIGINAL-STATOR INLET

		I.D.										O.D.
Percent Flow		0	10	20	30	40	50	60	70	80	90	100
pressure ratio	-	1.540	1.540	1.540	1.540	1.540	1.540	1.540	1.540	1.540	1.540	1.540
temperature ratio	-	1.141	1.134	1.135	1.136	1.138	1.140	1.141	1.143	1.146	1.150	1.157
M	-	0.899	0.849	0.821	0.798	0.778	0.761	0.745	0.732	0.719	0.708	0.697
M_m	-	0.545	0.596	0.602	0.602	0.600	0.595	0.589	0.583	0.577	0.567	0.551
M_z	-	0.528	0.585	0.597	0.599	0.598	0.594	0.589	0.583	0.577	0.567	0.551
β	degrees	52.69	45.49	42.79	40.97	39.54	38.54	37.75	37.11	36.70	36.80	37.82
β_z	degrees	53.55	45.99	43.07	41.12	39.62	38.58	37.77	37.12	36.71	36.80	37.82
ϵ	degrees	14.21	10.75	8.00	5.88	4.31	3.11	2.17	1.40	0.77	0.23	-0.27
					ENGLISH UNITS							
diameter	inches	17.169	19.206	20.915	22.477	23.856	25.174	26.420	27.609	28.749	29.851	30.931
V	ft/sec	994.9	944.0	916.5	894.3	875.1	858.3	843.3	829.9	818.1	807.9	799.4
V_z	ft/sec	584.5	650.2	665.9	671.7	672.9	670.3	666.4	661.7	655.9	646.9	631.5
V_m	ft/sec	602.9	661.8	672.5	675.3	674.8	671.3	666.8	661.9	655.9	646.9	631.5
V_θ	ft/sec	791.4	673.2	622.6	586.3	557.1	534.8	516.3	500.8	488.9	483.9	490.1
					SI UNITS							
diameter	meters	0.4361	0.4878	0.5312	0.5702	0.6059	0.6394	0.6711	0.7013	0.7302	0.7582	0.7856
V	m/sec	303.2	287.7	279.3	272.6	266.7	261.6	257.1	252.9	249.4	246.2	234.7
V_z	m/sec	178.1	198.2	202.9	204.7	205.1	204.3	203.1	201.7	199.9	197.2	192.5
V_m	m/sec	183.8	201.7	204.9	205.8	205.7	204.6	203.3	201.7	199.9	197.2	192.5
V_θ	m/sec	241.2	205.2	189.8	178.7	169.8	162.9	157.4	152.6	149.0	147.5	149.4

Calculations based on an inlet pressure of 2116 psf and an inlet temperature of 518.7°R.

APPENDIX 2 (Cont'd)

AERODYNAMIC DESIGN SUMMARY - ORIGINAL-STATOR EXIT

		I.D.										O.D.
Percent Flow		0	10	20	30	40	50	60	70	80	90	100
pressure static	–	1.375	1.473	1.504	1.513	1.516	1.516	1.515	1.513	1.509	1.503	1.493
temperature ratio	–	1.141	1.134	1.135	1.136	1.138	1.139	1.141	1.143	1.146	1.149	1.157
M	–	0.456	0.537	0.551	0.549	0.546	0.542	0.539	0.536	0.533	0.527	0.518
M_m	–	0.456	0.537	0.551	0.549	0.546	0.542	0.539	0.536	0.533	0.527	0.518
M_z	–	0.446	0.530	0.547	0.547	0.545	0.542	0.539	0.536	0.533	0.527	0.518
β	degrees	0	0	0	0	0	0	0	0	0	0	0
β_z	degrees	0	0	0	0	0	0	0	0	0	0	0
ϵ	degrees	12.34	9.09	6.63	4.82	3.51	2.52	1.74	1.11	0.60	0.17	-0.23
					ENGLISH UNITS							
diameter	inches	18.096	19.910	21.422	22.807	24.109	25.349	26.536	27.677	28.779	29.852	30.904
V	ft/sec	532.8	620.6	635.9	634.8	631.2	628.1	625.4	622.6	619.2	614.4	606.5
V_z	ft/sec	520.5	612.8	631.7	632.5	630.0	627.5	625.1	622.5	619.2	614.4	606.5
V_m	ft/sec	532.8	620.6	635.9	634.8	631.2	628.1	625.4	622.6	619.2	614.4	606.5
V_θ	ft/sec	0	0	0	0	0	0	0	0	0	0	0
					SI UNITS							
diameter	meters	0.4596	0.5057	0.5441	0.5793	0.6124	0.6439	0.6740	0.7029	0.7309	0.7582	0.7850
V	m/sec	162.4	189.2	193.8	193.5	192.4	191.4	190.6	189.8	188.7	187.3	184.8
V_z	m/sec	158.6	186.8	192.5	192.8	192.0	191.3	190.5	189.7	188.7	187.3	184.8
V_m	m/sec	162.4	189.2	193.8	193.4	192.4	191.4	190.6	189.8	188.7	187.3	184.8
V_θ	m/sec	0	0	0	0	0	0	0	0	0	0	0

Calculations based on an inlet pressure of 2116 psi and an inlet temperature of 518.7°R

APPENDIX 2 (Cont'd)

AERODYNAMIC DESIGN SUMMARY – REDESIGNED-STATOR INLET

		I.D.										O.D.
Percent Flow		0	10	20	30	40	50	60	70	80	90	100
pressure ratio	–	1.508	1.553	1.545	1.536	1.530	1.524	1.519	1.515	1.513	1.488	1.475
temperature ratio	–	1.1466	1.1423	1.1367	1.1354	1.1346	1.1330	1.1307	1.1318	1.1353	1.1435	1.1462
M	–	0.865	0.840	0.810	0.786	0.768	0.752	0.735	0.723	0.713	0.683	0.665
M_m	–	0.462	0.510	0.545	0.568	0.580	0.586	0.590	0.594	0.590	0.553	0.531
M_z	–	0.440	0.497	0.536	0.563	0.577	0.586	0.589	0.593	0.589	0.552	0.531
β_1	degrees	60.0	50.0	45.3	42.8	39.8	38.0	35.9	35.5	35.6	36.8	37.0
β_2	degrees	59.84	49.65	44.20	40.96	38.95	36.80	35.22	34.49	34.35	36.36	36.78
ϵ	degrees	17.7	13.0	10.6	8.1	5.8	3.9	2.8	2.3	1.6	1.1	0.0
					ENGLISH UNITS							
diameter	inches	17.22	19.40	21.12	22.60	24.00	25.30	26.50	27.62	28.78	29.80	31.00
V	ft/sec	965.	939.	906.	885.	864.	845.	830.	816.	805.	782.	762.
V_z	ft/sec	476.	603.	644.	662.	671.	676.	677.	672.	666.	629.	610.
V_m	ft/sec	500.	619.	655.	669.	674.	678.	678.	673.	666.	629.	610.
V_θ	ft/sec	820.	710.	626.	575.	542.	506.	478.	462.	455.	463.	456.
					SI UNITS							
diameter	meters	0.4374	0.4928	0.5364	0.5740	0.6096	0.6426	0.6731	0.7015	0.7310	0.7569	0.7874
V	m/sec	294.	286.	276.	270.	263.	258.	253.	249.	245.	238.	232.
V_z	m/sec	145.	184.	196.	202.	205.	206.	206.	205.	203.	192.	186.
V_m	m/sec	152.	189.	200.	204.	205.	207.	207.	205.	203.	192.	186.
V_θ	m/sec	250.	216.	191.	175.	165.	154.	146.	141.	139.	141.	139.

Calculations based on an inlet pressure of 2116 psf and an inlet temperature of 518.7°R

APPENDIX 2 (Cont'd)

AERODYNAMIC DESIGN SUMMARY – REDESIGNED STATOR EXIT

		I.D.										O.D.
Percent Flow		0	10	20	30	40	50	60	70	80	90	100
pressure ratio	–	1.449	1.474	1.494	1.513	1.511	1.507	1.503	1.498	1.492	1.461	1.445
temperature ratio	–	1.1466	1.1423	1.1367	1.1354	1.1346	1.1330	1.1307	1.1318	1.1353	1.1435	1.1462
M	–	0.578	0.578	0.578	0.583	0.578	0.573	0.568	0.565	0.559	0.529	0.506
M_m	–	0.578	0.578	0.578	0.583	0.578	0.573	0.568	0.565	0.559	0.529	0.506
M_z	–	0.548	0.565	0.571	0.579	0.575	0.571	0.567	0.564	0.559	0.529	0.506
β	degrees	0	0	0	0	0	0	0	0	0	0	0
β_z	degrees	0	0	0	0	0	0	0	0	0	0	0
ϵ	degrees	18.5	12.3	9.2	7.1	5.5	4.4	3.4	2.7	2.0	1.1	0.2
					ENGLISH UNITS							
diameter	inches	18.80	20.50	22.00	23.30	24.50	25.79	26.90	28.00	28.90	29.99	31.00
V	ft/sec	668.	668.	668.	669.	665.	655.	653.	648.	643.	615.	590.
V_z	ft/sec	632.	654.	660.	664.	660.	657.	654.	649.	643.	616.	593.
V_m	ft/sec	666.	669.	669.	669.	663.	658.	655.	650.	643.	616.	593.
V_θ	ft/sec	0	0	0	0	0	0	0	0	0	0	0
diameter	meters	0.4775	0.5207	0.5585	0.5918	0.6223	0.6550	0.6832	0.7112	0.7340	0.7617	0.7874
V	m/sec	204.	204.	204.	204.	203.	200.	199.	198.	196.	187.	180.
V_z	m/sec	193.	199.	201.	202.	201.	200.	199.	198.	196.	188.	181.
V_m	m/sec	203.	204.	204.	204.	202.	201.	200.	198.	196.	188.	181.
V_θ	m/sec	0	0	0	0	0	0	0	0	0	0	0

Calculations based on an inlet pressure of 2116 psf and an inlet temperature of 518.7°R

APPENDIX 3

AIRFOIL DEFINITIONS ON FLOW SURFACES (Assumed Conical) - ROTOR

ENGLISH AND SI UNITS

Percent Flow	0 Root	10	20	30	40	50	60	70	80	90	100 Tip
diameter at leading edge, inches	12.217	15.382	17.903	20.058	21.975	23.723	25.341	26.857	28.289	29.651	30.95
m	0.31031	0.39070	0.45473	0.50947	0.55817	0.60256	0.64366	0.68217	0.71854	0.75314	0.78621
cone angle α degs	18.20	14.40	10.80	8.20	6.20	4.60	3.30	2.20	1.20	0.40	-0.20
aerodynamic chord c, inches	4.5	4.671	4.800	4.910	5.008	5.101	5.189	5.275	5.352	5.421	5.525
m	0.1143	0.1186	0.1219	0.1247	0.1272	0.1296	0.1318	0.1340	0.1359	0.1377	0.1403
front chord c_f, inches	3.1	2.62	2.203	1.959	1.858	1.898	2.076	2.318	2.580	2.842	3.097
m	0.0787	0.0665	0.0560	0.0498	0.0472	0.0482	0.0527	0.0589	0.0655	0.0722	0.0787
blade angle β^*_5, deg	33.26	36.22	39.07	41.50	43.36	45.18	46.53	47.95	49.46	50.97	52.88
blade angle β^*_{5s}, deg	40.60	42.40	44.80	46.90	48.40	49.90	50.90	52.00	53.20	54.40	56.00
blade camber angle ϕ, deg	80.45	62.07	53.84	46.57	39.02	33.10	27.82	23.25	19.73	17.76	17.21
front camber angle ϕ_f, deg	60.82	30.69	18.80	12.22	7.89	5.51	4.02	3.31	2.56	2.16	2.79
max. thickness-to-chord ratio, t_{max}/c	0.07	0.0633	0.0581	0.0537	0.0494	0.0458	0.0422	0.0390	0.0359	0.0329	0.03
percent chord location of t_{max}	40.0	49.0	50.0	50.0	50.0	50.0	50.0	50.0	50.0	50.0	50.0
edge radii, L.E.R. - T.E.R., inch	0.0146	0.0137	0.0129	0.0122	0.0115	0.0108	0.0101	0.0095	0.0089	0.0083	0.0076
m	0.000373	0.000348	0.000328	0.000310	0.000292	0.000274	0.000257	0.000241	0.000226	0.000210	0.000193
maximum camber location, a/c	0.4794	0.5337	0.5392	0.5378	0.5403	0.5470	0.5610	0.5773	0.5984	0.6203	0.6343
solidity, σ	2.513	2.155	1.953	1.812	1.704	1.616	1.500	1.493	1.443	1.397	1.359

Rotor blades are multiple-circilar-arc airfoils on conical surfaces approximating streamlines of revolution.

Number of rotor blades is 24.

APPENDIX 3 (Cont'd)

AIRFOIL DEFINITIONS ON FLOW SURFACES (Assumed Conical) - ORIGINAL STATOR

ENGLISH AND SI UNITS

Percent Flow	0 Root	10	20	30	40	50	60	70	80	90	100 Tip
diameter at leading edge, inches	17.198	19.214	20.918	22.456	23.854	25.172	26.421	27.611	28.750	29.851	30.931
m	43.683	48.804	53.132	57.038	60.589	63.937	67,109	70.132	73.025	75,822	78.565
cone angle α, degs	14.42	11.16	8.06	5.55	4.13	2.86	1.91	1.11	0.48	0.09	-0.43
aerodynamic chord c, inches	1.877	1.858	1.842	1.834	1.830	1.828	1.827	1.826	1.826	1.826	1.826
m	4.7676	4.7193	4.6787	4.6584	4.6482	4.6431	4.6406	4.6380	4.6380	4.6380	4.6380
front chord c_f, inches	0.601	0.580	0.587	0.598	0.608	0.619	0.626	0.635	0.650	0.672	0.706
m	1.527	1.473	1.491	1.519	1.544	1.572	1.590	1.613	1.651	1.707	1.793
blade angle β^*_{11}, deg	48.82	41.11	38.02	35.78	34.02	32.82	31.74	30.83	30.20	30.12	30.71
blade angle $\beta^*_{11\epsilon}$, deg	52.91	45.38	42.72	40.90	39.50	38.54	37.73	37.11	36.70	36.83	37.32
blade camber angle ϕ, deg	65.73	56.45	52.58	47.45	44.38	43.62	44.09	44.90	45.10	46.11	47.55
front camber angle ϕ_f, deg	9.72	7.89	7.23	6.41	5.85	5.68	5.64	5.64	5.60	5.74	5.97
max. thickness-to-chord ratio, t_{max}/c	0.039	0.0431	0.0472	0.0507	0.0541	0.0564	0.0591	0.0619	0.0641	0.0663	0.07
percent chord location of t_{max}	50.0	50.0	50.0	50.0	50.0	50.0	50.0	50.0	50.0	50.0	50.0
edge radii, L.E.R. - T.E.R., inch	0.0034	0.0038	0.0041	0.0043	0.0046	0.0048	0.0051	0.0053	0.0053	0.0057	0.0059
m	.008636	.009652	.010414	.010922	.011684	.012192	.012954	.013462	.013462	.014478	.014086
maximum camber location, a/c	0.5309	0.5304	0.5328	0.5356	0.5381	0.5405	0.5425	0.5445	0.5470	0.5510	0.5577
solidity, σ	2.169	1.935	1.773	1.651	1.555	1.474	1.405	1.346	1.293	1.246	1.203

Original-stator vanes are multiple-circular-arc airfoils on concial surfaces approximating streamlines of revolution.

Number of original-stator vanes is 64

APPENDIX 3 (Cont'd)

AIRFOIL DEFINITIONS ON FLOW SURFACES (Assumed Conical) - REDESIGNED STATOR

ENGLISH AND SI UNITS

Percent Flow	0 Root	10	20	30	40	50	60	70	80	90	100 Tip
diameter at leading edge, inches	17.2	19.4	21.1	22.6	24.0	25.3	26.5	27.7	28.8	29.9	31.0
m	43.69	49.28	53.59	57.40	60.96	64.26	67.31	70.36	73.15	75.95	78.74
cone angle α. degs	18.50	12.20	9.80	7.50	5.80	4.20	3.20	2.30	1.60	1.40	0.0
aerodynamic chord c, inches	2.628	2.623	2.615	2.608	2.600	2.593	2.585	2.578	2.570	2.563	2.550
m	6.675	6.662	6.642	6.624	6.604	6.586	6.566	6.548	6.528	6.510	6.477
front chord c_f, inches	0.960	0.960	0.905	0.970	0.978	1.000	1.035	1.090	1.150	1.225	1.300
m	2.438	2.438	2.451	2.464	2.484	2.540	2.629	2.769	2.921	3.112	3.302
blade angle β_{11}*, deg	56.5	46.5	41.0	38.3	36.0	34.4	33.3	32.6	32.8	33.8	36.0
blade angle β_{115}*, deg	58.6	49.5	44.5	42.2	40.6	39.4	38.6	38.5	39.0	40.4	42.7
blade camber angle ϕ, deg	73.0	61.5	53.4	47.3	44.0	42.5	41.8	42.4	43.8	45.4	47.7
front camber angle ϕ_f, deg	11.2	10.4	10.2	10.5	11.2	12.8	14.5	16.6	18.9	21.3	23.5
max. thicknes-to-chord ratio, t_{max}/c	0.0410	0.0450	0.0484	0.0519	0.0550	0.0580	0.0615	0.0642	0.0670	0.0692	0.0720
percent chord location of t_{max}	56.00	55.00	54.40	53.80	53.00	52.50	52.00	51.50	51.00	50.50	50.00
edge radii, L.E.R. - T.E.R., inch	0.0048	0.0055	0.0059	0.0064	0.0067	0.0070	0.0073	0.0077	0.0080	0.0083	0.0086
m	.01219	.01397	.01499	.01626	.01702	.01778	.01854	.01956	.02032	.02108	.02184
maximum camber location, a/c	0.5463	0.5435	0.5400	0.5355	0.5300	0.5220	0.5132	0.5065	0.5020	0.5005	0.5025
solidity, σ	2.330	2.085	1.930	1.805	1.705	1.618	1.540	1.478	1.420	1.360	1.307

Redesign-stator vanes are multiple-circular-arc airfoils on conical surfaces approximating streamlines of revolution.

Number of redesigned-stator vanes is 50

REFERENCES

1. Tyler, J. M. and Sofrin, T. G.: "Axial-Flow Compressor Noise Studies"; *SAE Trans.* Vol. 70, 1962

2. Monsarrat, M. T.; Keenan, M. J.; and Tramm, P. C.: *High-Loading Low-Speed Fan Study, I. Design* NASA CR-72536, PWA-3535, 1969

3. Harley, K. G. and Burdsall, E. A.: *High-Loading Low-Speed Fan Study, II. Data and Performance, Unslotted Blades and Vanes;* NASA CR-72667, PWA-3653, 1970

4. Harley, J. G.; Harris, J.; and Burdsall, E. A.: *High-Loading Low-Speed Fan Study, III. Data and Performance Slotted Blades and Vanes and Rotor Tip Treatment;* NASA CR-72895, PWA-3899, 1971

5. Harley, K. G.; Odegard, P. A.; and Burdsall, E. A.: *High-Loading Low-Speed Fan Study IV. Data and Performance, Redesigned Stator and Rotor Tip Casing Treatment;* NASA CR-120866, PWA-4326, 1971

6. Keenan, M. J. and Bartok, J. A.: *Evaluation of Transonic Stators, Final Report:* NASA CR-72298, PWA-3470

7. Goldstein, A. M.; Lucas, J. G.; and Balombin, J. R.: *Acoustic and Aerodynamic Performance of a Six-Foot Diameter Fan for Turbofan Engines. II. Performance of QF-1 Fan in Nacelle Without Acoustic Suppression;* NASA TND-6080

8. Sofrin, T. G.; and McCann, J. C.: *Pratt & Whitney Aircraft Experience in Compressor Noise Reduction;* Acoustic Soc. Amer., Paper No. 202, 2 Nov. 66

9. Peacock, R. E.: *Flow Control in the Corners of Cascades;* Aeronautical Research Council, 27291, 1965

10. Horlock, J. H.: *Axial Flow Compressor,* Butterworths' Scientific Publications, London, 1958

11. Lucas, J. T.; Finger, H. B.; and Filippi, R. E.: *Effect of Inlet-Annulus Area Blockage on Overall Performance and Stall Characteristics of an Experimental 15-Stage, Axial Flow Compressor;* NACA RM E53L28, 1954

12. Sulam, D. H.; Keenan, M. J.; and Flynn, J. T.: *Single-Stage Evaluation of Highly-Loaded High-Mach-Number Compressor Stages, Data and Performance Report, Multiple-Circular-Arc Rotor;* NASA CR-72694, PWA-3772, 1970

13. Hanley, W. T.: "A Correction of End Wall Losses in Plane Compressor Cascades"; *ASME Transaction,* Sect. A. Vol. 99, pg 251-257

14. Robbins, W. H.; Jackson, R. J.; and Lieblein, S: "Blade-Element Flow in Annular Cascades", *Aerodynamic Design of Axial Flow Compressors (Johnson, J. A. and Bullock, R. O. eds);* NASA SP-361, 1965, Chapter VII, pg 227-254

15. Bullock, R. O.; and Johnsen, I. A.: "Compressor Design System". *Aerodynamic Design of Axial Flow Compressors (Johnsen, I. A. and Bullock, R. O. eds.);* NASA SP-36, 1965, Chapter III pg 53-100